2014

DEVELOPMENT OF INDIRECT RING TENSION TEST FOR FRACTURE CHARACTERIZATION OF ASPHALT MIXTURES

Alireza Zeinali Siavashani
University of Kentucky, alireza.zeinali@gmail.com

DEVELOPMENT OF INDIRECT RING TENSION TEST FOR FRACTURE
CHARACTERIZATION OF ASPHALT MIXTURES

_____

DISSERTATION

_____

A dissertation submitted in partial fulfillment of the
requirements for the degree of Doctor of Philosophy in the
College of Engineering
at the University of Kentucky

By
Alireza Zeinali Siavashani

Lexington, Kentucky

Director: Dr. Kamyar C. Mahboub, Professor of Civil Engineering

Lexington, Kentucky

2014

ABSTRACT OF DISSERTATION

DEVELOPMENT OF INDIRECT RING TENSION TEST FOR FRACTURE
CHARACTERIZATION OF ASPHALT MIXTURES

Low temperature cracking is a major distress in asphalt pavements. Several test configurations have been introduced to characterize the fracture properties of hot mix (HMA); however, most are considered to be research tools due to the complexity of the test methods or equipment. This dissertation describes the development of the indirect ring tension (IRT) fracture test for HMA, which was designed to be an effective and user-friendly test that could be deployed at the Department of Transportation level. The primary advantages of this innovative and yet practical test include: relatively large fracture surface test zone, simplicity of the specimen geometry, widespread availability of the required test equipment, and ability to test laboratory compacted specimens as well as field cores.

Numerical modeling was utilized to calibrate the stress intensity factor formula of the IRT fracture test for various specimen dimensions. The results of this extensive analysis were encapsulated in a single equation. To develop the test procedure, a laboratory study was conducted to determine the optimal test parameters for HMA material. An experimental plan was then developed to evaluate the capability of the test in capturing the variations in the mix properties, asphalt pavement density, asphalt material aging, and test temperature.

Five plant-produced HMA mixtures were used in this extensive study, and the results revealed that the IRT fracture test is highly repeatable, and capable of capturing the variations in the fracture properties of HMA. Furthermore, an analytical model was developed based on the viscoelastic properties of HMA to estimate the maximum allowable crack size for the pavements in the experimental study. This analysis indicated that the low-temperature cracking potential of the asphalt mixtures is highly sensitive to the fracture toughness and brittleness of the HMA material. Additionally, the IRT fracture test data seemed to correlate well with the data from the distress survey which was conducted on the pavements after five years of service. The maximum allowable crack size analysis revealed that a significant improvement could be realized in terms of the pavements performance if the HMA were to be compacted to a higher density. Finally, the IRT fracture test data were compared to the results of the disk-shaped

compact [DC(t)] test. The results of the two tests showed a strong correlation; however, the IRT test seemed to be more repeatable.

KEYWORDS: Asphalt Pavement, Low-Temperature Cracking,
            Fracture Mechanics, Material Characterization,
            Laboratory Testing

Alireza Zeinali Siavashani
Signature

7/30/14
Date

DEVELOPMENT OF INDIRECT RING TENSION TEST FOR FRACTURE
CHARACTERIZATION OF ASPHALT MIXTURES

By

Alireza Zeinali Siavashani

Dr. Kamyar C. Mahboub
_____
Director of Dissertation

Dr. Y. T. (Ed) Wang
_____
Director of Graduate Studies

Date: 7/30/2014
_____

DEDICATION

I dedicate this dissertation to my brilliant and outrageously loving wife, Shirin Abyazi,

whose unconditional support has always urged me to achieve my goals.

ACKNOWLEDGEMENTS

TABLE OF CONTENTS

LIST OF TABLES

LIST OF FIGURES

CHAPTER 1
INTRODUCTION

Hot mix asphalt (HMA) is the most expensive part of the asphalt pavements. HMA pavements provide relatively high strength and durability, smooth and quiet ride, and are yet constructed fairly easily at a relatively low cost. The life span, rideability, and need for costly maintenance treatments of asphalt pavements are significantly affected by type, extent, and rate of fracture that occurs in the surface layers of these pavements. The Superpave mix design, which resulted from the Strategic Highway Research Program (SHRP), addresses three major types of distress in asphalt pavements: rutting permanent deformation, fatigue cracking, and low-temperature cracking (Asphalt Institute 2001). Nonetheless, more forms of fracture are commonly observed in HMA pavements such as longitudinal surface or top-down cracking, reflective cracking of asphalt overlays placed on existing jointed or cracked pavements, and block cracking (Huang 1993).

Accurate characterization of HMA material is a necessity for design and maintenance of asphalt pavements which represent a major investment in the transportation infrastructure. To protect this investment and reduce the life-cycle cost of asphalt pavements, the pavement managers require the proper tools to quantify the performance of the pavements under specific traffic and climatic conditions. In recent years a great deal of effort has been directed toward the development of testing and evaluation methods that can be used for crack initiation and propagation mechanism analyses.

In cold climates, the failure mode of asphalt pavements is primarily induced by climatic conditions. As the pavement temperature decreases, the asphalt binder becomes more brittle due to its viscoelastic properties. As the result of temperature drop and thermal contraction of the asphalt pavement, thermal stresses accumulate in the HMA layer which is restrained by the lower pavement layers. In current designs practices, a mechanistic-empirical approach is used to predict the fracture resistance of asphalt concrete as governed by engineering material parameters, such as modulus and tensile strength (Huang 1993).

The thermal stresses caused by the temperature drop combined with the embrittlement of asphalt binder make the HMA pavements more susceptible to cracking (Asphalt Institute 2007). The capability of an asphalt binder to relax the thermal stresses and its resistance against low-temperature cracking can be evaluated through binder testing. However, once a binder is mixed with aggregates to produce the HMA, the adhesion and interactions between the components of the resulted mix can also influence the thermal cracking potential of the pavement. The effect of these interactions, such as absorption of asphalt, air void content, and the aggregate-binder bonding, cannot be predicted by binder testing alone, and instead the tests should be conducted on specimens of the asphalt mixture.

Mixture testing, which is also referred to as performance testing, is performed on HMA material at the structural scale to simulate the actual service conditions of an asphalt pavement. Additionally, the study of fracture mechanics reveals that formation of cracks and flaws during construction or service life of a pavement can significantly reduce the resistance of the pavement to cracking. Since the asphalt mixtures respond as a brittle material at low temperatures, understanding the fracture properties of HMA at such temperatures is arguably an indispensable step towards efficient design and maintenance of asphalt pavements in cold climates.

1.1 HMA Fracture Test Configurations

1.1.1 Single-Edge Notched Beam Test

Utilization of fracture mechanics theory for asphalt binders and mixtures started in late 1960s (Bahgat and Herrin 1968; Majidzade et al. 1971). These tests were primarily conducted on single-edge notched beam [SE(B)] specimens in which a simply-supported pre-notched beam is subjected to bending. Single-edge notched beam specimen geometry has been used extensively in measuring fracture toughness of metallic materials, and is standardized in ASTM E399 specification (2012). Majidzade et al. (1971) successfully employed single-edge notched beam [SE(B)] geometry in fracture testing of HMA specimens. SE(B) is a beam sample of HMA that is notched by a sharp cutting tool and is subjected to a compressive load under three-point bend test configuration. Fracture

toughness testing and mode-I loading configurations require that the compressive load in the three-point bend test to be applied on the beam surface and exactly along the notch direction. Figure 1.1 illustrates the geometry of the SE(B) test. The SE(B) loading apparatus is designed to minimize the frictional effects by using roller supports. The load point displacement is measured by linear variable differential transformers (LVDTs) during the test.
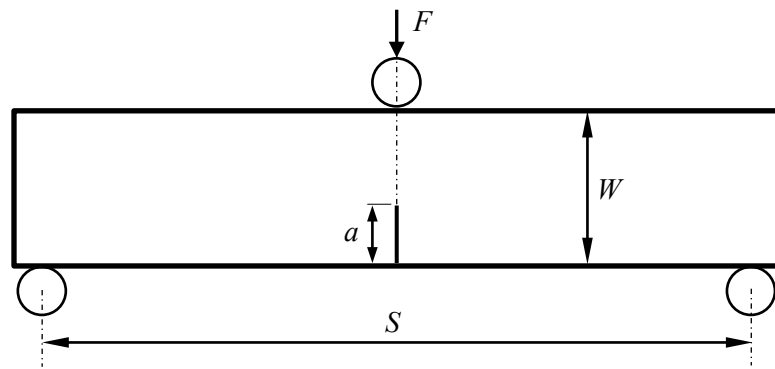
Figure 1.1. Single-Edge Notched Beam Test Geometry

Little and Mahboub (1985) evaluated the effect of initial crack shape and chevron notch on the SE(B) test results. Mahboub (1990) utilized the SE(B) geometry to measure the J-integral fracture energy of HMA materials. In this study, some modifications to the standard ASTM fracture testing procedures were proposed to accommodate the special characteristics of HMA mixtures. Additionally, electronic crack separation sensors were used to measure the crack length during the test.

SE(B) specimen configuration was later utilized to determining various fracture characteristics of HMA over a range of temperatures, specimen dimensions, crack length and mix designs (Bhurke et al. 1997; Marasteanu et al. 2002). In another study, the SE(B) test geometry was used along with numerical methods (Wagoner et al. 2005a). This study showed that the SE(B) test can adequately represent the reflective cracking conditions in asphalt pavements.

The SE(B) geometry has also been used in conjunction with cohesive zone model (CZM) to investigate the fracture behavior in hot mix asphalt (Song et al. 2006; Braham et al. 2012). Cohesive zone model presumes the fracture to be a gradual phenomenon.

According to the cohesive zone model theory, the crack surfaces are traction-free, and the crack grows into a cohesive zone where its growth is resisted by cohesive traction. The CZM concept was first proposed by Dugdale (1960) and Barenblatt (1962) for metallic materials and later extended by Hillerborg et al. (1976) and Hillerborg (1985) for quasi-brittle materials.

The SE(B) configuration is an advantageous tool for investigating fracture for several reasons. Foremost, the SE(B) specimen produces a stable crack growth after crack initiation. Also the size of the beam can be easily adjusted in a laboratory setting to ensure that the fracture mechanisms are not affected by end effects. The SE(B) test is a versatile test which can accommodate mixed-mode (combination of tensile and shear opening) fracture tests. Mixed-mode testing can easily be conducted by cutting the initial notch away from the central symmetry line of the beam.

The SE(B) geometry has the disadvantage of requiring a non-standard specimen geometry, which limits its applicability to cylindrical laboratory or field specimens. It is often impractical to extract beam shaped specimens from constructed pavement facilities. In a laboratory, making beam shaped specimens require special compaction equipment which significantly increase the test cost. The single-edge notched beam geometry has been extensively used for testing various materials; however, its application in asphalt materials has been restricted by the limited availability of the beam compactor devices, particularly at the state highway agency level.

1.1.2 Semi-Circular Bend Test

After development of the Superpave mix design, the Superpave gyratory compactor (SGC) was standardized as the primary compaction device in HMA mixture laboratories. Superpave gyratory compactors produce cylindrical HMA specimens. Furthermore, forensic investigations and in-situ sampling of asphalt pavements are typically conducted by coring the pavement structure, and obtaining the properties from those cylindrical cores. Thus, a fracture test specimen was needed which could be fabricated from the SGC compacted samples. By combining the bending beam geometry and cylindrical shape of HMA cores, the semi-circular bending (SCB) test geometry was developed and utilized in pavement fracture tests.

SCB specimen, as depicted in Figure 1.2, is comprised of a half disk of compacted asphalt mixture with an initial notch that initiates at the center of the circle. The specimen is supported symmetrically by two rollers and the load is applied on the top of the specimen. Load point displacement can be measured using an LVDT and a metal button on the specimen during the test procedure in order to calculate the fracture energy of the specimen. The crack mouth opening displacement (CMOD) can also be measured as a feedback signal by two metal buttons and an extensometer or by a single clip-on gage. This geometry was first proposed by Chong and Kurrupu (1984) for fracture testing of rocks. The SCB specimen geometry has also been used for fracture testing of rock materials with fatigue pre-cracking to introduce a sharp crack tip (Lim et al. 1994).

a = crack length

r = radius of specimen

2s = support span
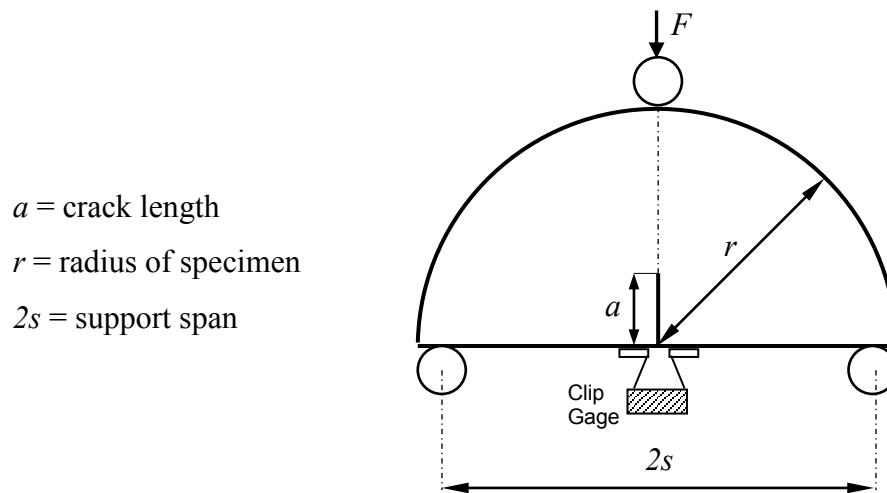
Figure 1.2. Semi-Circular Bend Specimen Geometry

Molenaar et al. (2000) utilized the SCB geometry to evaluate the fracture properties of HMA mixtures. In this study, seven standard types of asphalt mixtures were tested using three different specimen sizes, four test temperatures (25°C, 15°C, 0°C, and −10°C) and three loading rates (0.005, 0.05, and 0.5 mm/s). The results indicated that possible excessive plastic deformation may occur at the vicinity of crack tip at higher temperatures. Furthermore, it was observed that for a deformation rate of 0.05 mm/s, most specimens did not show significant non-linear deformation before peak load.

Additionally, the data showed that the fracture parameters obtained from the SCB specimens were not independent of the specimen dimensions, which indicates that the fundamental properties were not being measured without any interactions from the other factors. Nonetheless, the comparison of the test to the indirect tensile strength test showed that the SCB test is more sensitive to the mix properties.

The SCB test with a crack mouth opening (CMOD) rate of 0.0005 mm/s was employed in a study on three mixtures used at MnROAD facility (Mull et al. 2002; Li et al. 2005). The results showed that the fracture energy and fracture toughness as measured by the SCB test could differentiate asphalt mixtures with respect to low-temperature performance. The fracture energy seemed to be a better indicator due to its less dependence on the conditions of linear elasticity and homogeneity of the tested materials. However, both parameters were dependent upon the specimen size and temperature, which indicate that they were not measured as fundamental properties.

The semi-circular bend geometry was later utilized to determine the critical J-integral of HMA mixtures (Wu et al. 2005) using the elasto-plastic fracture mechanics concepts. However, the test procedure proposed in this work deviates significantly from the standard methods of determining the J-integral fracture energy. The SCB specimen has been utilized in different research studies for fracture characterization of HMA materials (Kim et al. 2012; Mogawer et al. 2013). In an experimental study, Mohammad et al. (2013) used the SCB test to measure the critical J-integral of the asphalt mixtures containing bio-binders. According to the test results, the mixtures that contained bio-binder exhibited less intermediate temperature fracture resistance than the conventional mixtures.

The semi-circular bend test specimens may also be taken form pavement field cores. One of the advantages of the SCB test is its potential in obtaining two test specimens from each field core, which can reduce the number of required cores. However, this division of the core into two parts causes a constraint on crack length and reduces the potential fracture surface area of the specimen. It should be noted that for testing non-homogenous materials such as HMA, a minimum specimen size is always required to account for the effect of non-homogeneity, and represent the actual properties of the material. Moreover, a high compressive zone is created in the top rounded part of

the specimen in bending tests, which prevents the crack from propagating in this zone. Consequently, the variation in the SCB test result is relatively high which undermines the applicability of the test for distinguishing the difference between HMA mixtures.

1.1.3 Disk-Shaped Compact Tension Test

Another specimen geometry which has been used for fracture testing of asphalt mixtures is the disk-shaped compact tension [DC(t)] specimen. DC(t) test configuration has been utilized for fracture testing of metals for decades. As depicted in Figure 1.3, a DC(t) specimen is made by cutting an initial notch along a diametric line of a disk-shaped specimen. Two holes are also drilled in the specimen on two different sides of the initial notch to facilitate tensile loading on the crack surfaces. One side of the specimen, where the notch starts, is flattened by a cutting saw to make a platform for mounting a clip-type crack mouth opening gauge.
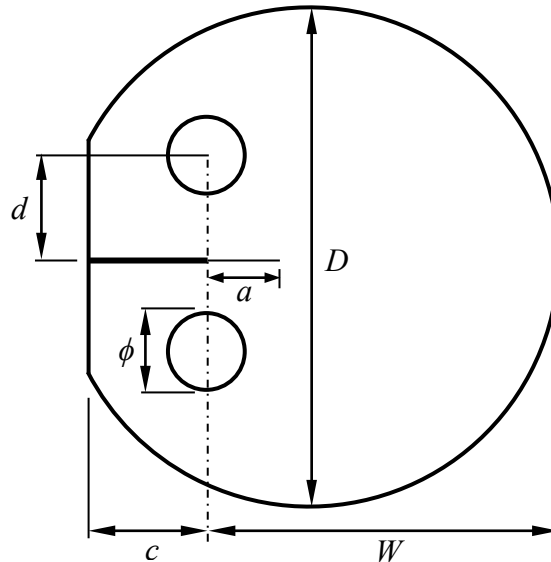
Figure 1.3. Disk-shaped Compact Tension Specimen Geometry

Wagoner et al. (2005b) used disk-shaped compact tension [DC(T)] geometry in HMA fracture tests which had been previously standardized in the ASTM E399 for metallic materials. However, in HMA fracture tests, due to failures that happened around the loading holes in the specimen, Wagoner et al. (2005c) changed the position of the

7

loading holes and proposed a new geometry for using DC(T) in HMA fracture tests. Additionally, the initial notch length of the DC(t) specimens was increased to the center of the specimen to make it more suitable for HMA materials and prevent failures around the loading holes.

DC(T) specimens can be obtained from standard cylindrical field cores as well as the laboratory-produced samples. However, the complexity of the DC(t) test equipment has somewhat limited its widespread use, and it is often viewed as a research tool by practitioners. Moreover, undesirable cracking behavior during the test, such as random failures around the loading holes and deviation of the cracking pattern from the straight diametrical direction, limited its use. As a matter of fact, the DC(t) test configuration does not produce a consistent crack growth pattern for HMA specimens and the crack path in many cases deviates from the straight line. Once such a crack deviation occur, the fracture mode of test changes from the mode-I to mixed-mode (mode I-II) fracture, and as a consequence, the variability in the test results would increase. Figure 1.4 displays DC(t) specimens with failed loading hole, and two different non-straight crack patterns.
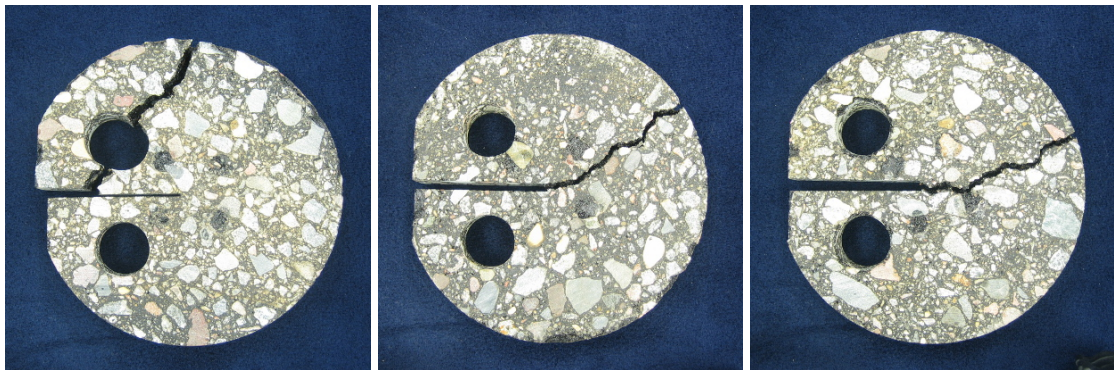
Figure 1.4. Imperfections in the Failure of DC(t) Specimens

Changing the ASTM standardized DC(T) specimen geometry to make it applicable for HMA fracture testing invalidates the ASTM stress intensity factor calibration equation for DC(T) specimen, and a new formulation is required for the new geometry. Wagoner et al. (2005a) employed the cohesive zone model theory and defined the fracture energy as the area under the load-CMOD (crack mouth opening

displacement) curve normalized by the area of fracture surface (initial ligament length times the specimen thickness). This parameter indicates the amount of work that is done to pull the crack faces apart. Although, this normalized fracture energy does not represent a true material property, it is useful as fracture potential ranking tool.

1.1.4 Indirect Tension Test

Indirect tensile strength test (IDT) has been extensively used by different highway agencies to measure the tensile strength of asphalt mixtures. By applying the elasticity theory concepts, it can be shown that when a disk-shaped sample of a homogenous, isotropic and linear elastic material is subjected to a pair of equal and diagonal loads (F), the internal stress magnitude along the loaded diameter would be a constant in the direction perpendicular to the loading line. Based upon this theory, indirect tension test configuration has been designed that is advantageous in several aspects such as:

- IDT test uses compressive loading apparatus for determining the tensile strength of materials which is more convenient than direct tensile loading configuration for lab tests.
- The deformation of the indirect test specimen can be easily measured in one, two, or three directions using either one or two LVDTs in each direction.
- The apparatus can be used under any existing loading frame (e.g. Marshall, hydraulic system, unconfined, triaxial).
- According to the symmetric geometry of the specimen in two directions, implementation of the test is more convenient than other similar methods.
- The apparatus is available in most HMA testing laboratories.

When a disk shaped body of an isotropic material is subjected to concentrated diametral load F, it can be shown that stress components in rectangular coordinate system at each point in the body for the notations in Figure 1.5, are (Frocht 1964):

$$\sigma_x = -\frac{2F}{\pi t}\left[\frac{(R-y)x^2}{r_1^4} + \frac{(R+y)x^2}{r_2^4} - \frac{1}{d}\right] \tag{1.1}$$

$$\sigma_y = -\frac{2F}{\pi t}\left[\frac{(R-y)^3}{r_1^4} + \frac{(R+y)^3}{r_2^4} - \frac{1}{d}\right] \qquad (1.2)$$

$$\tau_{xy} = \frac{2F}{\pi t}\left[\frac{(R-y)^2 x}{r_1^4} + \frac{(R+y)x}{r_2^4}\right] \qquad (1.3)$$

where,

F= diametric load

R= disk radius

T= disk thickness

r_1 and r_2= distance from the loading points

x and y= Cartesian coordinates with origin at the disk center
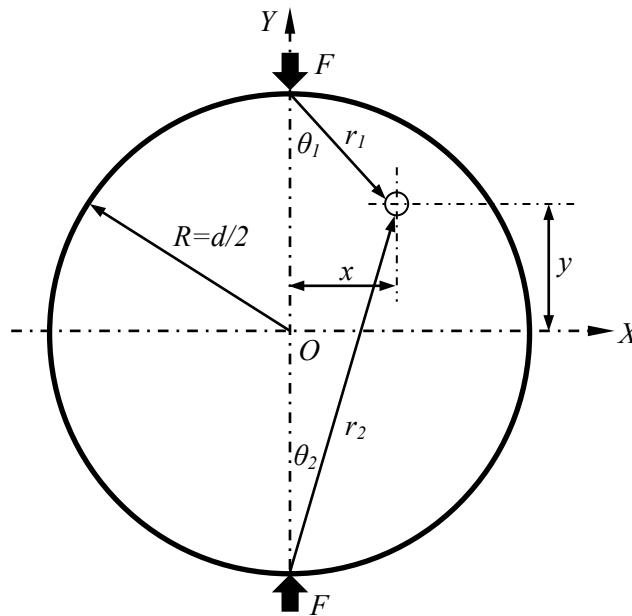
Figure 1.5. Disk under the Action of Two Diametrically Opposite Concentrated Loads

Along the loading line, the stresses can be determined by:

$$\sigma_x = \frac{2F}{\pi t d} \tag{1.4}$$

$$\sigma_y = -\frac{2F}{\pi t}\left[\frac{2}{d - 2y} + \frac{2}{d + 2y} - \frac{1}{d}\right] \tag{1.5}$$

$$\tau_{xy} = 0 \tag{1.6}$$

Thus, it is seen that across the vertical central section, i.e. along the loading line, the horizontal tension is constant and the vertical compression is theoretically infinite when r_1=0 or when r_2=0. The minimum numerical value of the vertical compression is *6F/(πdt)* at the center of the disk. The distribution of the stresses across the X and Y axes are shown in Figures 1.6 and 1.7.

The simplicity and widespread availability of the IDT test equipment persuaded the researchers to develop other HMA tests with similar configurations such as resilient modulus, IDT creep compliance, and IDT repeated load fatigue tests. It has also been shown that the triaxial shear strength of HMA can be correlated to its strength by applying the time-temperature superposition principles and the results can be used to estimate the mixture cohesion (Pellinen et al. 2005). In another research, the results from IDT strength test, IDT resilient modulus test, and IDT creep compliance tests were used together to estimate the dissipated creep strain energy of HMA, and use it as an indicator for top-down cracking potential of asphalt pavements (Zhang et al. 2001; Birgisson et al. 2002)

In theory, an IDT specimen with a central notch along the loading line could be used for Mode-I fracture testing of HMA. The stress distribution of the IDT specimen would induce a tensile stress on the crack faces without any shear stress. Furthermore, by changing the inclination angle of the central notch with respect to the loading direction, the mode of the fracture test can vary from mode-I to mixed-mode (Jia et al. 1996). Nevertheless, cutting such a narrow notch at the center of an HMA specimen is not practicable with the regular tools in typical asphalt laboratories.
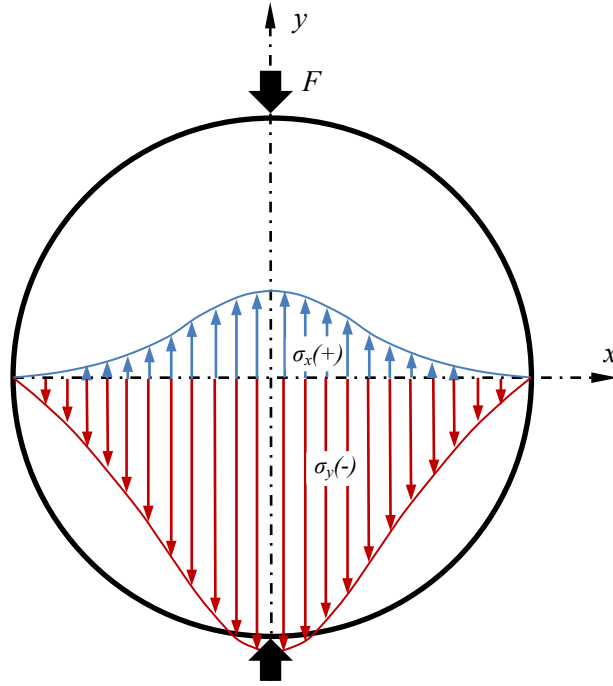
Figure 1.6. Stress Distribution along the Horizontal Diameter of IDT Specimen
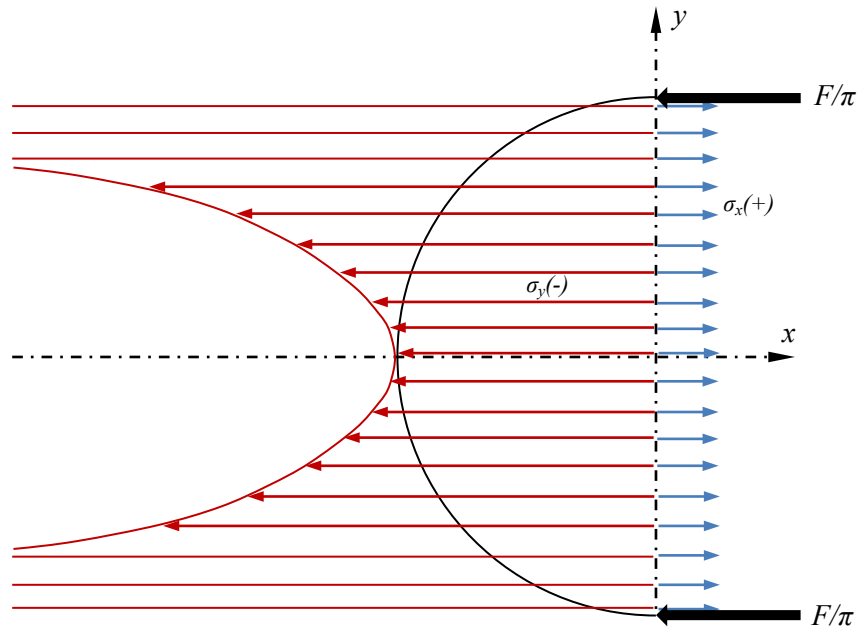
Figure 1.7. Stress Distribution along the Loading Diameter of IDT Specimen

Hiltunen and Roque (1994) used a centrally notched disk-shaped sample with a small hole at the center to measure the parameters related to the fatigue crack growth in HMA. The central hole was drilled at the center of the specimen so that the cutting device would have room to create the initial notch. However, in the absence of the stress intensity factor formula for this geometry, the test results were interpreted using the equations for an infinitely large cracked body subjected to a uniform tensile stress. In a research on compacted soils, Harison et al. (1994) calculated the stress intensity factor of a somewhat similar ring specimen, but with a larger central hole, for a specific set of dimensions through numerical modeling. In another study, Yang et al. (1997) used a similar geometry to measure fracture parameters of portland cement concrete. In a theoretical study, Fischer et al. (1996) conducted finite element analysis to calculate the stress intensity factor of a somewhat similar specimen with a specific set of dimensions and flatten loading areas.

1.2 Introduction of IRT Fracture Test

The indirect ring tension (IRT) fracture test was developed in this study such that it could produce repeatable data, and would be implementable with the existing equipment in the asphalt testing laboratories. The purpose of this research was to develop a user-friendly HMA fracture test that was effective, based upon fundamental concepts, and yet simple enough that it could be used at the Department of Transportation (DOT) level. The approach was to do the hard work for the user, and deliver a set of protocols which could be easily implemented by the practitioners.

The configuration of the indirect ring tension (IRT) fracture test is depicted in Figure 1.8. To fabricate an IRT specimen of HMA, a hole is cored out from the central part of a disk-shaped laboratory specimen or a field core specimen. Then, two notches with equal lengths are cut along the diametrical line of the disk. This fracture test is performed in a compression test frame, which is the most basic mechanical testing device available in most asphalt laboratories. Furthermore, a mixed-mode fracture test could be conducted by simply changing the inclination angle of the specimen prior to applying the load. When compared to other HMA fracture test geometries, the IRT specimen can

better produce the stress distribution condition of a pavement under thermally-induced loads. As the pavement temperature drops, the entire depth of the asphalt layer is subjected to tensile stress, which is similar to the stress distribution along the crack propagation line in the IRT fracture test. This stress distribution enables the crack to grow rapidly into the fracture ligament when the material enters its quasi-brittle phase. Furthermore, the stress distribution of IRT specimen prevents the potential for ductility interfering with fracture, which sometimes occurs in bending-mode HMA fracture test due to the relatively low stiffness of the asphalt mixtures.
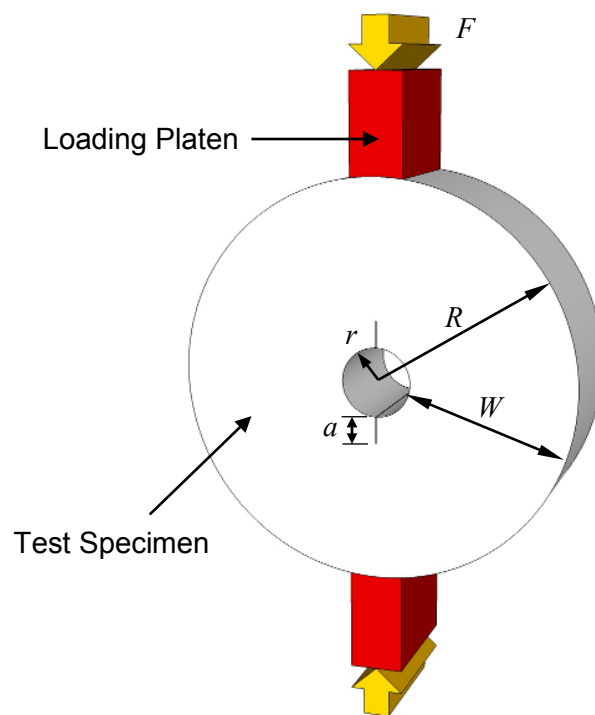
Figure 1.8. Indirect Ring Tension Fracture Test Geometry
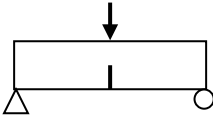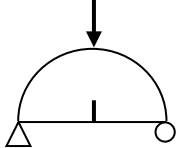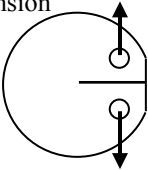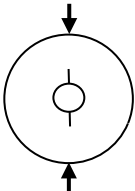
The primary advantages of the IRT fracture test configuration include:
- Simulating the stress distribution of an HMA layer under low-temperature tensile loads,
- Ease of potential implementation,
- Generating a mode-I fracture on a relatively consistent basis,
- High repeatability,

14

- Ability to accommodate field cores as well as laboratory-compacted samples,
- Relatively high fracture surface area, and
- Relatively low cost.

Table 1.1 briefly compares the IRT test configuration to the other existing test for fracture testing of HMA.

Table 1.1. Comparison of Different Geometries for HMA Fracture Testing

Specimen Geometry	Advantages	Disadvantages	Potential Fracture Surface Area
Single-edge Notched Beam	- Simple specimen geometry - Ability to investigate mixed mode fracture - High fracture surface area	- Cannot be obtained from field core specimens - Constraint for crack propagation to the top	7500 mm^2
Semi-circular Bending	- Easy to fabricate from field cores - Ability to investigate mixed mode fracture	- Complicated stress distribution - Low crack length limit - Constraint for crack propagation to the round top - Low fracture surface area	3750 mm^2
Disk-shaped Compact Tension	- Easy to obtain from field cores - Standard ASTM test method for HMA - High fracture surface area	- Complicated stress distribution - Crack path deviation - Failure around the loading holes - Low fracture surface area (3750 mm^2)	5500 mm^2
Indirect Ring Tension	- Obtained directly from field cores - Simple test procedure - Low variability of the results - Compatible with other HMA tests - High fracture surface area - Implementable with existing equipment in HMA labs	- New test, limited data on mixture types	5500 mm^2

Note: the fracture surface areas were calculated based on a 50-mm specimen thickness.

It is noteworthy to mention that various modeling methods, such as continuum damage model (Hou et al. 2010), cohesive zone model (Hyunwook et al. 2008), and dissipated strain energy (Sangpetngam et al. 2003) have been utilized to evaluate the cracking phenomena and cumulative damage in asphalt mixtures. Such theories and models can also be employed along with the IRT specimen geometry to study the internal state of the HMA cracking at lower temperatures. However, the objective of this research was to utilize the IRT specimen geometry to characterize the fundamental fracture properties of HMA and use such properties to rank the mixtures performance and estimate the low-temperature performance of asphalt pavements.

To develop a fracture-mechanics-based test, the stress intensity factor of the IRT fracture specimen was calibrated through finite element modeling. Next, the developed stress intensity factor equation was used to develop the IRT fracture test procedure and optimize it for the HMA material. Then, an experimental study was conducted on plant-produced HMA samples to examine the capability of the IRT test in discerning the difference between the potential cracking susceptibility of the HMA mixtures. Additionally, a viscoelastic model was used in conjunction with the IRT fracture test data to evaluate the cracking performance of the pavements in the field based on a hypothetical cooling scenario. Moreover, two experimental studies were executed by the IRT fracture test to evaluate the effect of pavements density and aging on their thermal cracking potential.

CHAPTER 2
STRESS INTENSITY FACTOR CALIBRATION

2.1 Fracture Mechanics

The field of fracture mechanics focuses on failure mechanism of flawed or cracked materials. Analytical solutions and experimental methods are used in fracture mechanics to explain the behavior of materials in the presence of a crack. At the microscopic scale, a crack is considered as a cut in a body inducing a stress singularity. Crack surfaces are the opposite boundaries of the crack which are traction-free, and the crack ends at the crack tip. In linear fracture mechanics, the cracked body is presumably made of linear isotropic elastic material in the whole domain. In such materials, any possible inelastic process in the vicinity of the crack tip is restricted to a small region that is negligible at macro scale.

In the analysis of low-temperature cracking of asphalt pavements, the thermally-induced loads are traditionally compared with the tensile strength of the material as the failure criteria. However, the study of fracture mechanics reveals that tensile strength can be very misleading as a fracture resistance indicator, and high strength materials can be very susceptible to fracture in the presence of cracks and flaws. In fact, the fracture strength of a cracked material can be far more representative of the actual field performance than its laboratory-measured tensile strength. Since it cannot be guaranteed that a pavement material will remain flaw-free during its construction and service life, the fracture mechanics approach seems to provide more reliable information about the actual resistance of the pavements to thermal cracking.

Generally, three types of crack opening can be defined with regard to deformation of crack and the body. Figure 2.1 schematically illustrates the crack opening modes which are denoted as mode-I, mode-II, and mode-III fracture. In mode-I, the crack opening is symmetric with respect to x-z plane and occurs in most of actual engineering situations related to cracked components, including low temperature cracking of asphalt pavements. Mode-II or in-plane shear mode occurs when the crack surfaces slide over each other in a direction normal to the crack front. Mode-III, also called tearing mode, is characterized by movement of crack surfaces in a tangential direction to the crack front.
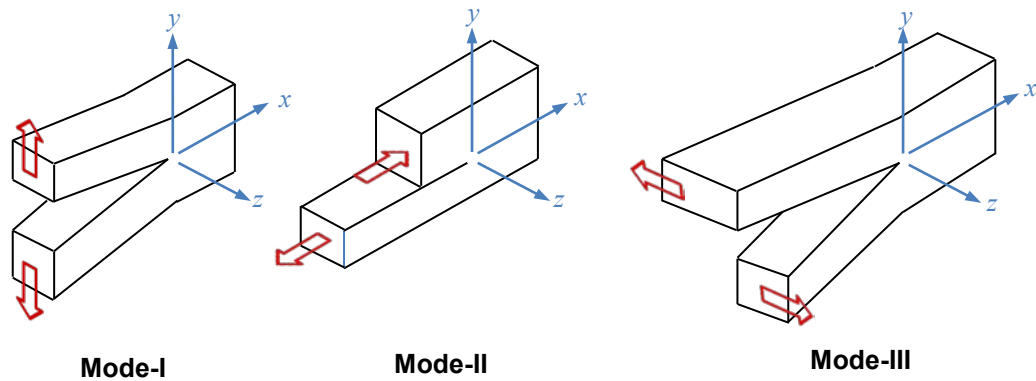
Figure 2.1. Basic Modes of Loading Involving Different Crack Surface Displacements

Given the numerous applications of mode-I fracture in engineering problems, considerable attention has been given to analytical and experimental methods for quantification of mode-I crack propagation. Multiple test methods and standard procedures have been developed to characterize the mode-I fracture of various engineering materials. Some Mode-I test configurations are also capable of producing a mixed-mode fracture test. The mixed mode-I & mode-II loading condition is often generated by changing the inclination angle of the initial crack with respect to the load direction. Such test configuration would induce in-plane shear stress as well as the tensile stress in the vicinity of the crack tip. For instance, as depicted in Figure 2.2, the mode-I single-edge notched bending beam [SE(B)] test can be turned into a mixed mode-I & II test by cutting the initial specimen crack with the angle δ with respect to the vertical loading line. In order to characterize the mode-I fracture properties of a materiel, it is crucial for the test to be able to maintain the crack growth pattern at the straight line during the test. As the crack grows, inclination of the crack growth pattern changes the mode-I loading to a mixed mode. This change in the fracture mode can result in higher variation in the test results and make the measured properties less reliable.
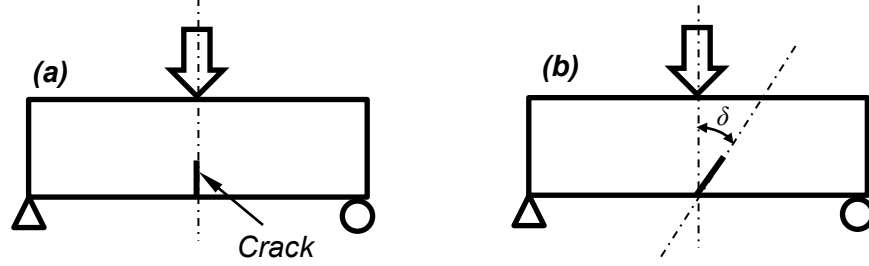
**Figure 2.2. SE(B) Test Configuration: a) Mode-I Fracture, b) Mixed Mode-I &
Mode-II Fracture**

2.2 Stress Intensity Factor

In a fracture mechanics problem of a body with a straight crack, under either plane-strain
or plane-stress conditions, the body behavior within a small region around the crack tip is
of highest importance. For the notation shown in Fig. 2.2 and mode-I loading conditions,
the associated stresses in the vicinity of the crack tip in isotropic plane bodies can be
found by (Gross and Seelig 2006):

$$\sigma_{yy} = \frac{K_I}{\sqrt{2\pi r}} \cos\frac{\theta}{2}\left(1 + \sin\frac{\theta}{2}\sin\frac{3\theta}{2}\right) \qquad [2.1a]$$

$$\sigma_{xx} = \frac{K_I}{\sqrt{2\pi r}} \cos\frac{\theta}{2}\left(-\sin\frac{\theta}{2}\sin\frac{3\theta}{2}\right) \qquad [2.1b]$$

$$\sigma_{xy} = \frac{K_I}{\sqrt{2\pi r}}\left(\sin\frac{\theta}{2}\cos\frac{\theta}{2}\cos\frac{3\theta}{2}\right) \qquad [2.1c]$$

and the deformation of the crack tip vicinity in y and x directions can be found by:

$$u = \frac{K_I}{2G}\sqrt{\frac{r}{2\pi}}(\kappa - \cos\theta)\cos\frac{\theta}{2} \qquad [2.2a]$$

$$v = \frac{K_I}{2G}\sqrt{\frac{r}{2\pi}}(\kappa - \cos\theta)\sin\frac{\theta}{2} \qquad [2.2b]$$

where

r and θ = coordinates of the point in local polar coordinate system

G= shear modulus

$$\kappa = \begin{cases} 3 - 4\nu & \text{if plane-strain or axisymmetric} \\ \dfrac{3-\nu}{1+\nu} & \text{if plane-stress} \end{cases}$$

ν = Poisson's ratio

K_I = mode-I stress intensity factor
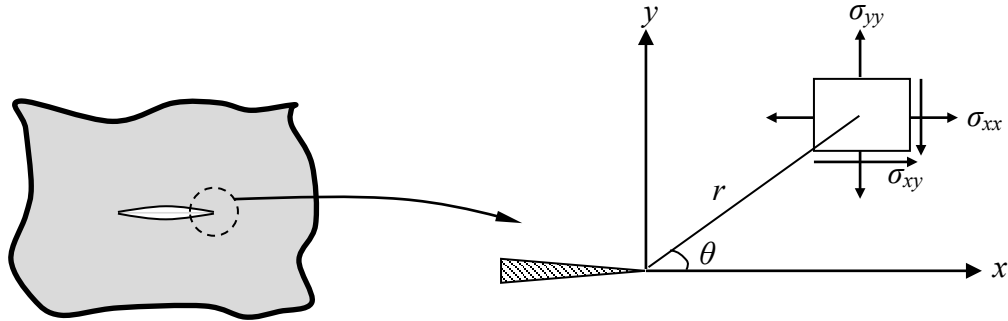
Figure 2.3. Vicinity of the Crack Tip in a Cracked Body

Equation 2.1 concludes that the stresses σ_{ij} have singularities of the type $r^{-1/2}$, where r is the radius measured from the crack tip as shown in Figure 2.3. The strains ε_{ij} have the same singularities of type $r^{-1/2}$ and increase infinitely as the distance from the crack tip becomes very small. Furthermore, Equation 2.1 shows that the stress distribution around any crack tip in a structure is similar and depends only on parameters r and θ. The difference between the cracked components is in the magnitude of parameter K which is defined as stress intensity factor. K is essentially a factor that defines the magnitude of the stress in the vicinity of the crack tip.

For mode-II crack opening the stress and displacements in the crack tip field can be found by (Gross and Seelig 2006):

$$\sigma_{yy} = \frac{K_{II}}{\sqrt{2\pi r}} \sin\frac{\theta}{2} \cos\frac{\theta}{2} \cos\frac{3\theta}{2} \qquad \text{[2.3a]}$$

$$\sigma_{xx} = \frac{K_{II}}{\sqrt{2\pi r}} \left(- \sin\frac{\theta}{2}\right)\left(2 + \cos\frac{\theta}{2} \cos\frac{3\theta}{2}\right) \qquad \text{[2.3b]}$$

$$\sigma_{xy} = \frac{K_{II}}{\sqrt{2\pi r}} \cos\frac{\theta}{2} \left(1 - \sin\frac{\theta}{2} \sin\frac{3\theta}{2}\right) \qquad [2.3c]$$

and

$$u = \frac{K_{II}}{2G} \sqrt{\frac{r}{2\pi}} (\kappa + 2 + \cos\theta) \sin\frac{\theta}{2} \qquad [2.4a]$$

$$v = \frac{K_I}{2G} \sqrt{\frac{r}{2\pi}} (\kappa - 2 + \cos\theta) \cos\frac{\theta}{2} \qquad [2.4b]$$

Stresses in the vicinity of the crack tip in a body under mode-III crack loading as depicted in Figure 2.3 are determined by:

$$\sigma_{xz} = \frac{K_{III}}{\sqrt{2\pi r}} \left(-sin\frac{\theta}{2}\right) \qquad [2.5a]$$

$$\sigma_{yz} = \frac{K_{III}}{\sqrt{2\pi r}} \left(cos\frac{\theta}{2}\right) \qquad [2.5b]$$

and displacement in the z-direction is:

$$w = \frac{2K_{III}}{G} \sqrt{\frac{r}{2\pi}} sin\frac{\theta}{2} \qquad [2.6]$$

As can be seen in Equations 2.1 to 2.6, stress intensity factors play the major role in defining the magnitude of stress in the vicinity of the crack tip. There exist multiple methods to determine K factors. Since K is directly tied to the configuration of the cracked component and the application of loads, generally all linear elasticity techniques can be utilized, and when closed form solutions are needed, analytical methods can be used. These methods are applicable only in simple boundary value problems. The analysis of more complex problems usually is utilized with numerical methods. Finite element method is one of these numerical approaches which is commonly used, but other schemes like boundary element method and finite difference method can also be employed successfully. Furthermore, some experimental methods such as compliance

method (Bonesteel et al. 1978; Newman 1981), strain measurements in the crack tip vicinity by using high sensitivity measurement tools (Dally and Sanford 1987), and photoelasticity (Hyde and Warrior 1990; Voitovich et al. 2011) have been utilized to determine the K factors for complex configurations.

Generally, the stress intensity factor depends on the configuration of the crack component as well as the manner in which the load is applied. It has been shown that (Hertzberg 1996):

$$K = f(\sigma, a) \tag{2.7}$$

where a is the crack length, and the crack is assumed to be sharp with a very small crack tip radius. By increasing the mode-I traction in a crack field in a plane-strain condition, the K_I magnitude escalates to a maximum value at which point the crack starts growing. This maximum K_I value is known as the plane-strain fracture toughness (K_{IC}), which is a material specific property, and can be directly related to the fracture performance of the material.

As Equation 2.1 shows, the stress state in the vicinity of the crack tip has a singularity of type $r^{-1/2}$ and the stress magnitude tends to infinity at the crack tip. In metallic materials, such high stresses exceed the yield strength and develop a plastic zone in a region around the crack tip, where r is small. In brittle materials containing voids, such as Portland cement concrete and hot mix asphalt, microcracks form in the cohesive zone that is developed around the crack tip. By coalescence of these microcracks, the crack grows and propagates into the fracture ligament. The fracture toughness of the material depends on the volume of material that undergoes permanent deformation prior to fracture (Hertzberg 1996). Since this volume depends on specimen thickness, it follows that the fracture toughness K_c will vary with thickness as presented in Figure 2.4.

When the sample is thick in a direction parallel to the crack front (such as *t2* in Figure 2.4), a large σ_z stress can be generated which restricts deformation in that direction. Alternatively, when the sample is very thin, such as *t1* in Figure 2.4, the degree of strain constraint acting at the crack tip is not considerable and as a result, the plane-stress conditions prevail and the material exhibits maximum toughness. The most

important aspect of plane-strain fracture toughness (K_{IC}) of a material is that for any testing conditions and specimen geometry, it remains a constant and does not decrease with increasing sample thickness. Basically, the plane-stress fracture toughness depends on the specimen geometry in addition to the natural properties of the material, while the plane-strain fracture toughness depends only on the material properties. In other words, thickness effects can be avoided by comparing the plane-strain fracture toughness values of different materials. As the result, plane-strain fracture toughness has become the material's conservative lower limit of toughness in engineering application.
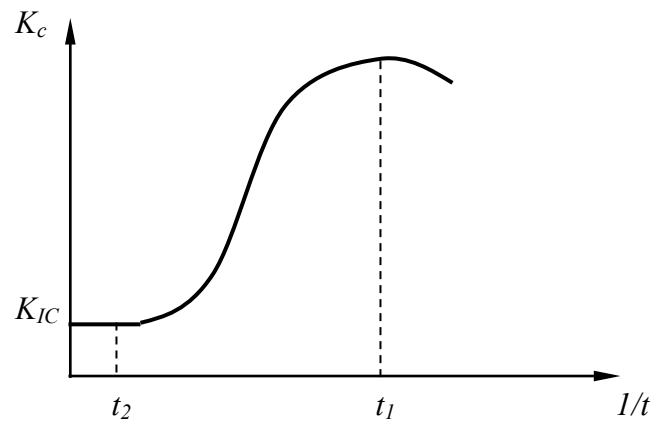
Figure 2.4. Variation in Fracture Toughness with Respect to Plate Thickness

Any specimen size and geometry that represents plane strain condition can be used in determination of fracture toughness of a material. The test specimen must have a starter crack which is sometimes produced by applying an oscillating load to an initially notched specimen. Fracture toughness of a material can also be determined by specimens taken from naturally cracked components with geometries whose stress intensity formula is already known. Basically fracture toughness is one of the most commonly used material properties in engineering design. For a certain material, knowing the fracture toughness enables determining the critical flaw size or the stress that can be tolerated before fracture.

Brown and Srawley (1966) after examining the fracture toughness of several alloys with different specimen geometries and testing conditions, proposed the following

empirical relation to calculate the minimum specimen thickness and crack size to perform valid plane-strain tests on metallic materials:

$$t \text{ and } a \ \geq 2.5 \left(\frac{K_{IC}}{\sigma_{ys}} \right)^2 \qquad\qquad [2.8]$$

where t is the specimen thickness, a is the crack size, and σ_{ys} is the yield strength of the material. For other materials the minimum thickness for plane-strain test can be obtained by trial and error or numerical methods. If a lower level of fracture toughness is obtained after repeating the test with a thicker sample, then the initially obtained value is no longer valid.

2.3 Finite Element Modeling

Asphalt binder is generally a viscoelastic material whose response is a function of temperature. By lowering the temperature, the asphalt phase angle is reduced and it exhibits more of an elastic behavior. As the temperature decreases to below the glass transition temperature, viscous properties of asphalt diminish and it behaves similar to a linear elastic material. Since the thermal cracking of asphalt mixtures typically occurs at such low temperatures, the linear elastic fracture mechanics theory may be used to model HMA's response to thermally-induced tensile loads. By employing the linear elastic fracture mechanics theory, it is assumed that the HMA is a homogenous, isotropic, linear elastic material at the designated test temperatures. Furthermore, the shape of the crack in the test specimen is assumed to be a straight line with a sharp tip.

Proper utilization of the indirect ring tension (IRT) specimen for fracture characterization of HMA necessitates the calibration of the stress intensity factor equation for the IRT specimen geometry. This calibration equation would produce the stress intensity factor for the IRT specimen for various specimen sizes, and load magnitudes. The K calibration equation is used to characterize the fracture properties of a material in fracture toughness and fatigue crack propagation tests.

In order to calibrate the stress intensity factor equation for the IRT specimen configuration, finite element (FE) modeling was utilized to calculate the K values for various geometries. An individual FE model was made for every combination of the IRT's geometric parameters using the ANSYS® Academic Research, Release 12.0 software (ANSYS, Inc., 2009a).

2.3.1 Crack Tip Element

In the study of fracture mechanics, most interest is often focused on the singularity point where stress becomes (mathematically but not physically) infinite. Near such singularities polynomial-based finite element approximations perform poorly and attempts have frequently been made to include special functions within an element that can model the analytically known singular function. An element of this kind, shown in Figure 2.4 was introduced by Henshell and Shaw (1975), and Barsoum (1976), almost simultaneously. This element is made from quadratic, isoparametric quadrilateral or triangular elements by shifting the mid-side node to the quarter point.

For the 8-node elements shown in Figure 2.5, the shape functions in the normalized space (ξ, η), $(-1 \leq \xi \leq +1$, $-1 \leq \eta \leq +1$) are (Barsoum 1976):

$$N_i = [(1 + \xi\xi_i)(1 + \eta\eta_i) - (1 - \xi^2)(1 + \eta\eta_i) - (1 - \eta^2)(1 + \xi\xi_i)]\xi_i^2\eta_i^2/4 +$$
$$(1 - \xi^2)(1 + \eta\eta_i)(1 - \xi_i^2)\eta_i^2/2 + (1 - \eta^2)(1 + \xi\xi_i)(1 - \eta_i^2)\xi_i^2/2 \qquad [2.9]$$

where N_i are shape functions corresponding to the node i, whose coordinates are (x_i, y_i) in the x–y system and (ξ_i, η_i) in the transformed ξ–η system. The stiffness matrix for the elements is:

$$\{\varepsilon\} = [J]^{-1}[B(\xi, \eta)]\begin{Bmatrix} u_i \\ v_i \end{Bmatrix} \qquad [2.10]$$

where $[B]$ is the stiffness matrix, $\{\varepsilon\}$ is strain vector, u_i, v_i are displacements, and $[J]$ is Jacobian matrix:

$$[J] = \begin{bmatrix} \dfrac{\partial x}{\partial \xi} & \dfrac{\partial y}{\partial \xi} \\ \dfrac{\partial x}{\partial \eta} & \dfrac{\partial y}{\partial \eta} \end{bmatrix} = \begin{bmatrix} \cdots & \dfrac{\partial N_i}{\partial \xi} & \cdots \\ \cdots & \dfrac{\partial N_i}{\partial \eta} & \cdots \end{bmatrix} \begin{bmatrix} \vdots & \vdots \\ x_i & y_i \\ \vdots & \vdots \end{bmatrix} \qquad\qquad [2.11]$$

The stresses are given by:

$$\{\sigma\} = [D]\{\varepsilon\} \qquad\qquad [2.12]$$

where $[D]$ is the stress-strain matrix. The element stiffness $[K]$ is then:

$$[K] = \int_{-1}^{1} \int_{-1}^{1} [B]^T [D][B].\det|J| \, d\xi \, d\eta \qquad\qquad [2.13]$$

In order to obtain a singular element to be used to at the crack tip, the strain in Equation 2.10 and stress in Equation 2.12 must be singular. This singularity can be achieved by placing the mid-side node at the quarter points of the sides, and requiring that the Jacobian $[J]$ be singular at the crack tip. In other words, the determinant of the Jacobian (*det* $|J|$) should vanish at the crack tip.
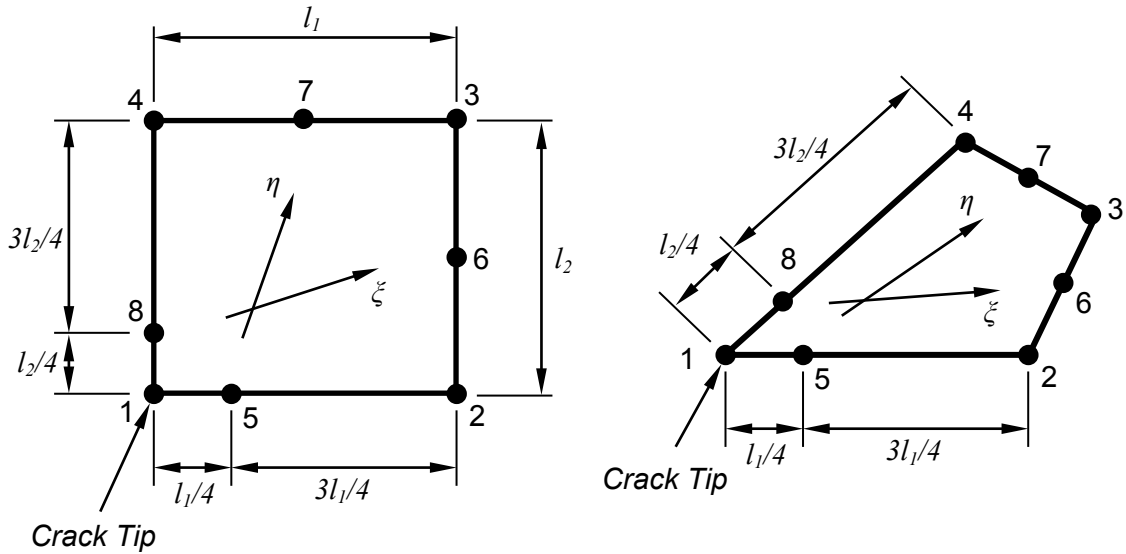
Figure 2.5. 2-D Rectangular Elements with Mid-side Node at the Quarter Points

For the 8-node quadrilateral element with mid-side nodes of two sides at the quarter points (Figure 2.5), the displacement along the line 1–2 is:

$$x = -\frac{1}{2}\xi(1-\xi)x_1 + \frac{1}{2}\xi(1+\xi)x_2 + (1-\xi^2)x_5 \qquad [2.14]$$

By choosing $x_1=0$, $x_2=L$, and $x_5=L/4$, the displacement function will be:

$$x = \frac{1}{2}\xi(1+\xi)L + (1-\xi^2)\frac{L}{4} \qquad [2.15]$$

therefore,

$$\xi = \left(-1 + 2\sqrt{\frac{x}{L}}\right) \qquad [2.16]$$

The term $\partial x/\partial \xi$ in the Jacobian is given by:

$$\frac{\partial x}{\partial \xi} = \frac{L}{2}(1+\xi) = \sqrt{xL} \qquad [2.17]$$

which makes the Jacobian singular at (x=0, ξ=-1). Consequently, the resulting stress at the crack tip will be singular as well. Similarly, displacement u along the line 1-2 is:

$$u = -\frac{1}{2}\xi(1-\xi)u_1 + \frac{1}{2}\xi(1+\xi)u_2 + (1-\xi^2)u_5 \qquad [2.18]$$

And writing it in terms of x yields:

$$u = -\frac{1}{2}\left(-1 + 2\sqrt{\frac{x}{L}}\right)\left(2 - 2\sqrt{\frac{x}{L}}\right)u_1 + \frac{1}{2}\left(-1 + 2\sqrt{\frac{x}{L}}\right)\left(2\sqrt{\frac{x}{L}}\right)u_2$$

$$+ \left(4\sqrt{\frac{x}{L}} - 4\frac{x}{L}\right)u_5$$

[2.19]

The strain in the x-direction is then:

$$\varepsilon_x = \frac{\partial u}{\partial x} = J^{-1}\frac{\partial u}{\partial \xi} = -\frac{1}{2}\left(\frac{3}{\sqrt{xL}} - \frac{4}{L}\right)u_1 + \frac{1}{2}\left(\frac{-1}{\sqrt{xL}} + \frac{4}{L}\right)u_2 + \left(\frac{2}{\sqrt{xL}} - \frac{4}{L}\right)u_5 \qquad [2.20]$$

The strain singularity along the line 1–2 is therefore, 1/√r, which is the required singularity for elastic analysis.

In finite element modeling of cracked components, triangular elements are more commonly used than quadrilateral ones. The 6-node triangle with mid-side nodes at the quarter points in Figure 2.6 can be generated by collapsing by the side 1–4 of the quadrilateral in Figure 2.5. In this case the singularity is investigated along the x-axis, *η=0*.
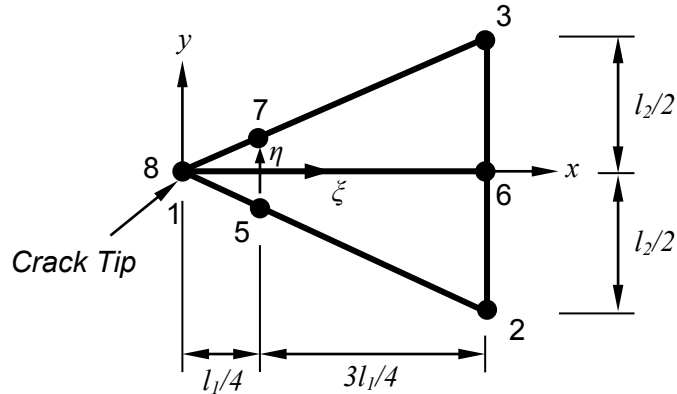
Figure 2.6. 2-D Triangular Element with Mid-side Nodes at the Quarter Points

$$x = -\frac{1}{4}(1+\xi)(1-\xi)l_1 + \frac{1}{2}(1-\xi^2)\frac{l_1}{4} + \frac{1}{2}(1+\xi)l_1 \qquad [2.21]$$

therefore,

$$\xi = \left(-1 + 2\sqrt{\frac{x}{l_1}}\right) \qquad [2.22]$$

Similar to Equation 2.16, the Equation 2.22 can satisfy the singularity condition of stress and strain at the crack tip.

Generally, the triangular quarter point elements give excellent results for elastic and perfectly-plastic analysis of small scale yielding problems. These elements are easy to use and exist in most advanced finite element programs. Basically quadrilateral elements can only provide singularity along sides containing the quarter-point nodes whereas the triangular elements provide the singularity through the interior when measuring the distance from the crack tip.

2.3.2 Symmetry and Plane-Strain State of the Model

The geometry of IRT fracture test has a biaxial symmetry with respect to the loading line as well as the line normal to the loading line in the disk surface plane. These symmetry lines are denoted as x and y axes in Figure 2.7. Due to the biaxial symmetric conditions of the model, the model size was reduced to only a quadrant of the domain. As depicted in Figure 2.7, the degrees of freedom (DOF) were adjusted along the x and y axes for the symmetry conditions. Roller supporters along the horizontal symmetry indicates that the vertical displacement of all the nodes along this line is zero ($u_y=0$). Additionally, the nodes on the vertical symmetry axis which are placed between the crack tip and the top of the loading strip were constrained to have zero displacements in x-direction ($u_x=0$). These zero displacements in the x-direction are shown by roller supporters in Figure 2.7b along the vertical boundary of the model.
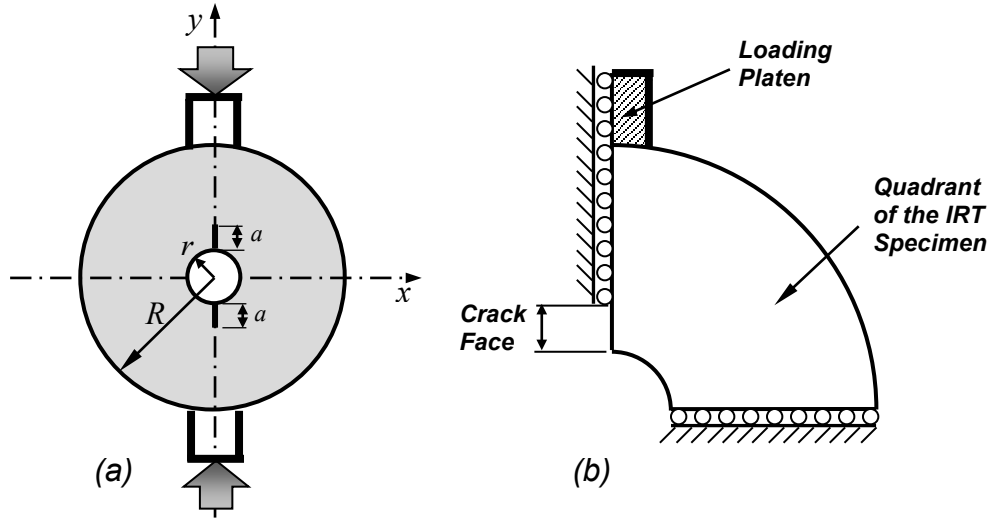
Figure 2.7. Biaxial Symmetry of the Finite Element Model

The IRT fracture test for HMA has been developed to be conducted on specimens at plane-strain state. To develop a finite element model that maintains the plane-strain conditions, the displacement field should satisfy the following relations (Reddy 2006):

$$u_x = u_x(x, y) \quad ; \quad u_y = u_y(x, y) \quad ; \quad u_z = 0 \qquad [2.23]$$

where (u_x, u_y, u_z) are the components of the displacement vector in the *(x, y, z)* coordinate system. This displacement field results in the following strain field:

$$\varepsilon_{xz} = \varepsilon_{yz} = \varepsilon_{zz} = 0 \qquad [2.24]$$

and

$$\varepsilon_{xx} = \frac{\partial u_x}{\partial x} \quad ; \quad 2\varepsilon_{xy} = \frac{\partial u_x}{\partial y} + \frac{\partial u_y}{\partial x} \quad ; \quad \varepsilon_{yy} = \frac{\partial u_y}{\partial y} \qquad [2.25]$$

The stress components for an isotropic material in a state of plane strain are given by:

$$\sigma_{xz} = \sigma_{yz} = 0 \quad ; \quad \sigma_{zz} = \upsilon(\sigma_{xx} + \sigma_{yy}) \qquad [2.26]$$

where ν is the Poisson's ratio. By combining the Equations 2.23 and 2.26, the stress-strain relationship for the finite element model reduces to:

$$\begin{Bmatrix} \sigma_{xx} \\ \sigma_{yy} \\ \sigma_{xy} \end{Bmatrix} = \frac{E}{(1+\nu)(1-2\nu)} \begin{bmatrix} 1-\nu & \nu & 0 \\ \nu & 1-\nu & 0 \\ 0 & 0 & 1-2\nu \end{bmatrix} \begin{Bmatrix} \varepsilon_{xx} \\ \varepsilon_{yy} \\ 2\varepsilon_{xy} \end{Bmatrix} \qquad [2.27]$$

As it shown in Equation 2.27, a finite element model in plane-strain condition can only be generated by satisfying the continuity and stress-strain relations in the x–y plane. By using this method, the finite element model for the IRT fracture test was reduced to a two-dimensional model. This decreased the solution time and size of the model significantly without any negative impact on the results.

2.3.3 Finite Element Model

The finite element model of the IRT fracture test involved curved boundaries and stress concentration around the loading area. In order to accurately model these irregularities, the element PLANE82 from the ANSYS Element Library (ANSYS 2009b) was utilized with a fine mesh to discretize the domain (Figure 2.8a). PLANE82 includes 8-node quadrilateral, and 6-node triangular, quadratic elements provides high accuracy in results for mixed (quadrilateral-triangular) meshes and can tolerate irregular shapes without a significant loss in accuracy (Zienkiewicz 1977). Moreover, the quadratic elements have a better ability to model the stresses in the vicinity of the loading platens, where the stress magnitude changes rapidly as the distance from the loading platen increases. The loading platens were also modeled using the quadrilateral PLANE82 quadratic elements, and the material properties were adjusted for steel.

Given the special attention to the stress singularity at the crack tip in fracture mechanics problems, singular elements described in Section 2.3.1, were used in the vicinity of the crack tip as illustrated in Figure 2.8b. Additionally, the loading platen was modeled as a separate object with contact to the surface of the test specimen. The contact between the two surfaces was modeled through a series of contact and target finite elements. TARGE169 is a two dimensional target segment in ANSYS element library (ANSYS 2009b) and it is used to represent and discretize various 2-D target surfaces for the associated contact elements. The contact elements themselves overlay the solid elements describing the boundary of a deformable body and are potentially in contact with target surface, defined by TARGE169. The contact and target surfaces are associated with a shared real constant. Any translational or rotational displacement, forces and moments, temperature, voltage, and magnetic potential can be imposed on the target segment elements.
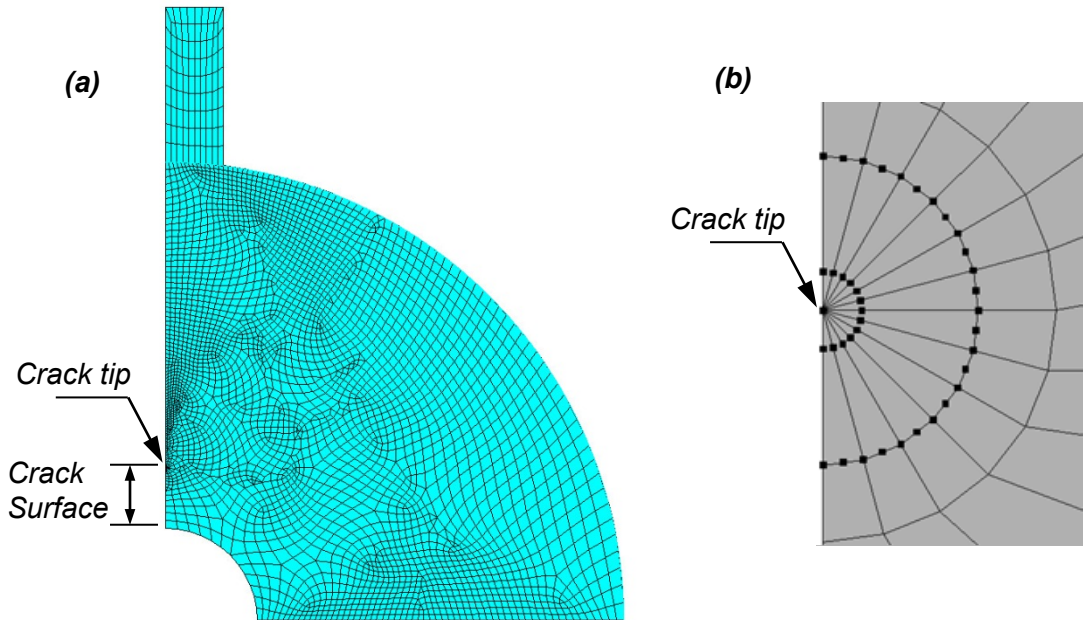
Figure 2.8. *a)* Finite Element Model, *b)* Singular Triangle Elements at the Crack Tip

CONTA172 is a two dimensional, 3-node, surface-to-surface contact element and is used to represent contact and sliding between the target surface and a deformable surface (ANSYS 2009b). This element was used on the curved surface of the test

specimen in the FE model. CONTA172 contact element has the same geometric characteristics as the solid element with which it has connected. Contact occurs when the element surface touches one of the associated target segment elements.

In general, for contacting two flexible bodies, if a convex surface is expected to come into contact with a flat or concave surface, the flat/concave surface should be target surface. On the other hand, when one surface is stiffer than the other, the softer one should be the contact surface and the stiffer one should be the target surface (ANSYS 2012). Considering these two important guidelines in designating the surfaces, the concave and stiffer surface of loading platen in the IRT test model was covered with target surface elements, and the convex surface of the specimen was modeled as the contact surface. Target and surface elements have the capability of defining friction between them. In this model, the friction coefficient between two contact and target surface was assumed to be zero, which represents a no friction surface between the specimen and loading platen. Moreover, to simulate the actual testing conditions, the compressive load on the specimen was modeled as a uniformly distributed load on the top surface of the loading platen.

Figure 2.9 illustrates the deformation of the IRT specimen from the solution of one of the FE models. The discretization of the domain and the un-deformed original boundaries of the model can also be seen in this figure. The test specimen was modeled with a fine mesh as depicted in Figure 2.9 to minimize the error in the model solution. Figure 2.10 displays the principal σ_x values which were resulted from one of the finite element models. As expected, a highly concentrated tensile stress was resulted at the vicinity of the crack tip. The magnitude of the tensile stress drops rapidly as the distance from the crack tip increases. In summary, the special crack tip elements seemed to be well capable of modeling the stress singularity at the crack tip.
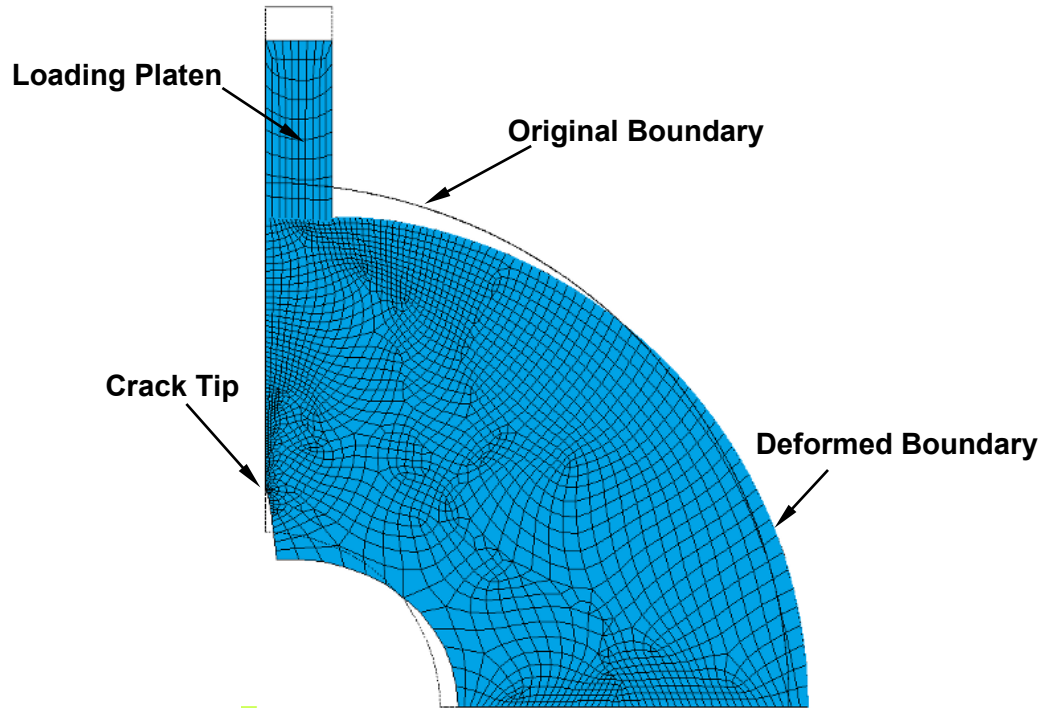
Figure 2.9. Original and Deformed Boundaries of the Finite Element Model

Note: The deformations are magnified in this figure to make it distinguishable from the original boundaries

2.3.4 Calculation of the Stress Intensity Factor

After solving each finite element model, the stress intensity factor of the specimen was calculated using the nodal displacement results. For plane-strain mode-I fracture, the displacement of the nodes along the crack surface ($\theta=0$) can be determined by Equation 2.4. For the notation shown in Figure 2.11, the displacement of the crack in the direction normal to its crack surface can be determined by:

$$u = \frac{2K_I}{G}\sqrt{\frac{r}{2\pi}}(1-v)$$

[2.28]

where

u = displacement in the direction normal to the crack face

K_I = mode-I stress intensity factor

G = shear modulus

r = distance from the origin of the local cylindrical system

v = Poisson's ratio
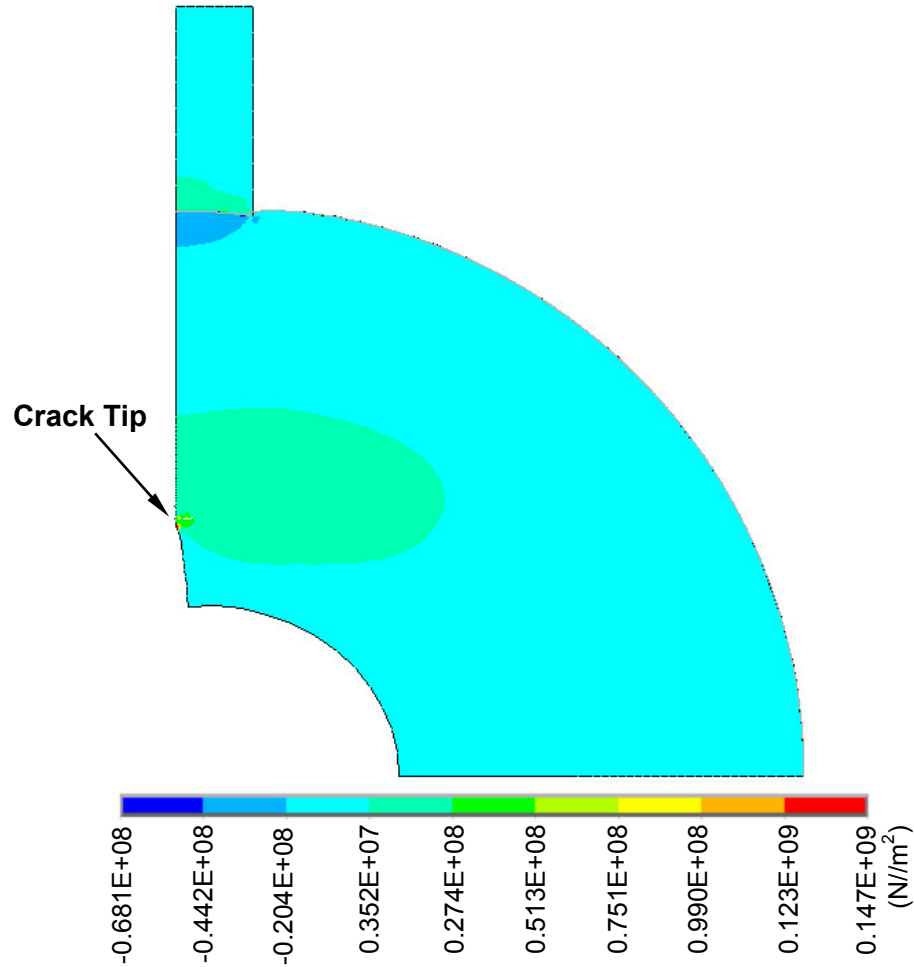
Figure 2.10. Contour Plot of the σ_x Values from One of the FE Models

Thus, for a finite element model that is symmetric with respect to the crack face, the stress intensity factor in the plane-strain mode would be:

$$K_I = \sqrt{2\pi} \frac{G}{2(1-v)} \frac{|u|}{\sqrt{r}}$$

[2.29]

As illustrated in Figure 2.11, the displacements of the three nodes located on the crack tip element (O, M, and N) can be obtained from the finite element modeling of the cracked body. While the displacement of the node O is zero, the displacement of the nodes M and N can be used to estimate the crack deformation. To determine the K_I values of the IRT specimens, the following model, in which u is normalized to be zero at O, was

fitted to the displacement data in the post-computation process of the ANSYS program (ANSYS, 2009b):

$$\frac{|u|}{\sqrt{r}} = A + B.r \qquad [2.30]$$

This fitted model accommodates the proportionality of u with respect to the squared root of r. By substituting the displacement of the M and N nodes (Figure 2.11), the A and B coefficients can be determined for each model. For the crack tip (node O), as the r value approaches zero, the $|u|/\sqrt{r}$ will approach A. Consequently, the K_I for the model can be determined by:

$$K_I = \sqrt{2\pi}\,\frac{GA}{2(1-v)} \qquad [2.31]$$

where A is already known from fitting the Equation 2.30 to the displacements of the nodes on the crack face.
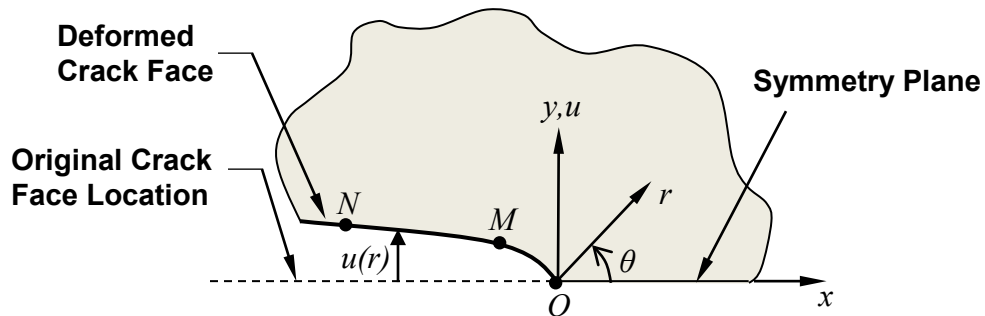
Figure 2.11. Calculation of Stress Intensity Factor from Crack Tip Displacement

2.3.5 Verification of the Finite Element Model

To assure the accuracy of the K_I values from finite element modeling of the IRT fracture test, an analytical solution was needed to be used as the check point. Such an analytical solution has not been developed for the IRT specimen due to the complexities in calculation of the stress distribution. Nonetheless, a centrally cracked indirect tension

(IDT) test specimen can be considered as a special case of the IRT geometry. That is, if the inner radius of an IRT specimen is zero (practically no central hole), it turns into an IDT specimen with a vertical crack at the center of the circle. For such a simplified geometry, some analytical solutions have been published in the literature. Fett (2001) and Dong et al. (2004) used weight functions in two separate studies to solve the differential equations for the stress distribution of a centrally cracked IDT specimen. As demonstrated in Figure 2.12, these two methods produced very similar K_I. These analytical solutions for the centrally cracked IDT geometry were used to cross check the validity of the results obtained from FE modeling of the IRT fracture test.

For the purpose of this verification, a finite element model was developed for the centrally cracked IDT by removing the central hole from the IRT specimen model ($r=0$). This model was developed with the same details of the IRT test model, and for a specimen with a diameter of 150 mm. The model was solved for various crack lengths and the stress intensity factors were calculated. The same specimen dimensions were then used to determine the stress intensity factors by the Fett's and Dong's analytical methods.
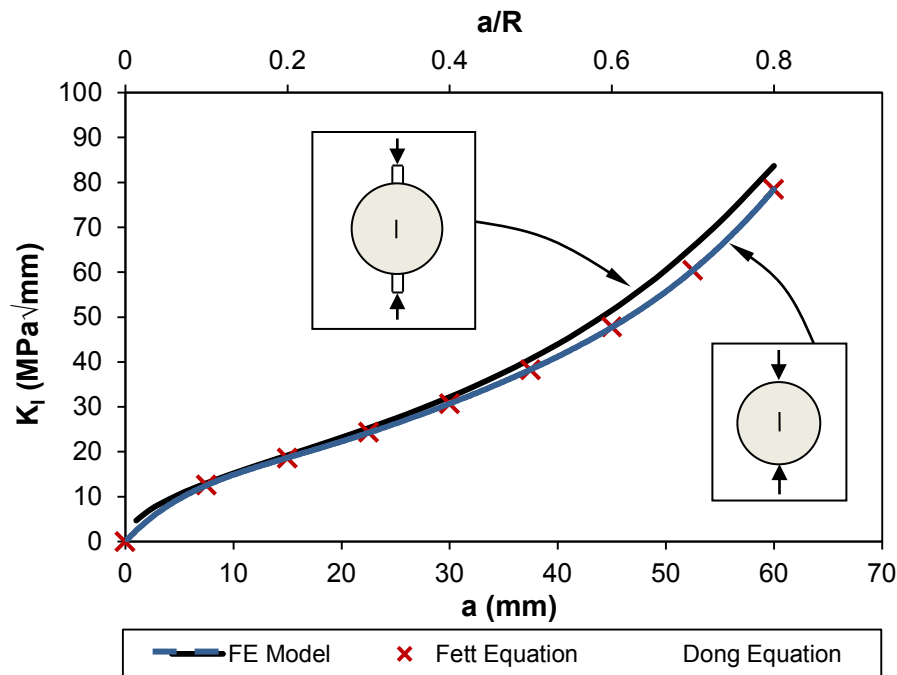
Figure 2.12. Verification of the FE model with analytical solutions for the centrally cracked IDT Specimen Geometry
Note: FE model properties: R=75 mm, B=100 mm, F=60 kN

Figure 2.12 compares the K_I values obtained from the FE model and the analytical solutions. This comparison showed a closed agreement between the stress intensity factor values from the three methods. It is noteworthy to mention that some approximations were used in the Fett's and Dong's solutions such as neglecting the higher order derivative terms. In addition, the effect of the loading platens on the specimen deformation was neglected in their solutions and the load was applied at a single point. By contrast, more realistic testing condition was modeled for the IRT fracture test in which the load was distributed on the loading platens with a set of dimensions which are standardized in the AASHTO T 322 (2007) test method for determining the tensile strength of HMA.

Applying the load through the loading platens distributes the load on an area on the specimen circumference. Consequently, by neglecting the loading platens, the small triangular-shape compressive zones at the contact points of the specimen and loading plates were not considered in the analytical solutions. The width of these loading areas induces small triangular-shape compressive zones in the specimen where it is in contact with the loading platens. This difference between the FE model and analytical methods could be the reason for the slight differences between the resulted stress intensity factors particularly for the larger crack sizes, when the crack tips are closer to the top and bottom triangular-shape compressive zones. For crack lengths ($2a$) of 50 mm or lower, when the crack tip is not influenced by the compressive zone, the agreement between the three methods is remarkably close.

2.4. IRT Stress Intensity Factor Formula

After successful verification of the finite element model with the analytical solutions, the model was regenerated for a range of various geometric parameters of the IRT test specimen. More than 3600 scenarios were modeled, and each model was solved for various load magnitudes. Table 2.1 presents the specimen dimension ranges for which the FE models were developed.

A small portion of the calculated K_I values from the finite element modeling is presented in Figure 2.13 to illustrate the relationship between K_I and specimen geometry.

The data in Figure 2.13 were obtained from the FE models for IRT specimens with 100, 150, and 200 mm outer diameter with various inner diameters and crack sizes. As expected, the obtained K_I results showed a linear relationship to the applied compressive load. Therefore, the K_I/p (stress intensity factor divided by the applied load) ratio was used in data analysis to eliminate one of the variables in the final model.

To facilitate the use of IRT stress intensity factor data, all the data obtained from the finite element modeling was encapsulated in the form of a single formula. Several evaluations were conducted on the data to establish the effect of various specimen geometries on the K_I values. Typically, the K_I for a specimen of linear elastic materials is linearly related to load magnitude and $\sqrt{a}$. Plane-strain K_I also has an inverse linear relationship to the specimen thickness (B). Moreover, the K_I formula involves a non-dimensionalized function that calibrates the K_I equation for the specific specimen geometry. The evaluations on the FE modeling data revealed that K_I of the IRT specimen is directly related to the specimen's r/R (inner diameter to outer diameter) ratio. That is, for two IRT specimens with different sizes but similar r/R values, the stress intensity factor formula would be similar. This trend had also been found in the K_I calibration formula of the arc-shaped specimen geometry (Anderson 1995).

Table 2.1. Range of the Geometric Parameters in the FE Model

Dimension	Range
Outer Radius (R)	50, 75, 100, 125, 150, 175, 200 mm
Inner Radius (r)	2 mm $< r <$ 0.8R
Crack Length (a)	1 mm $< a <$ 0.8R-r
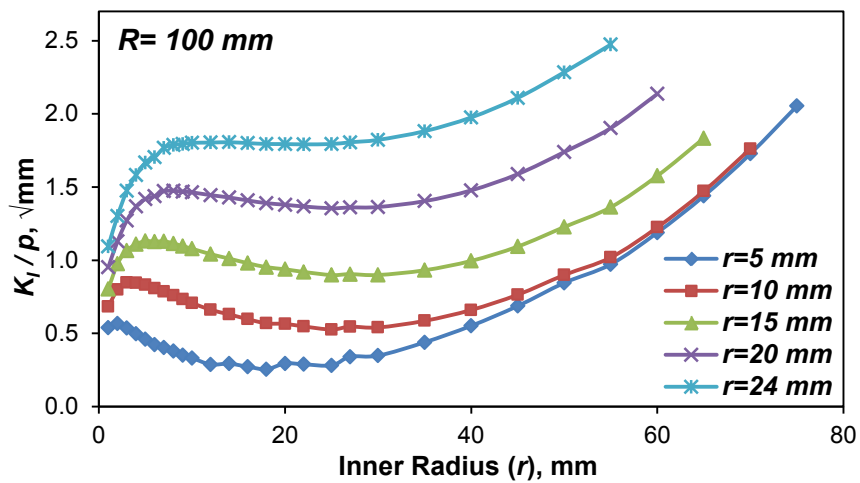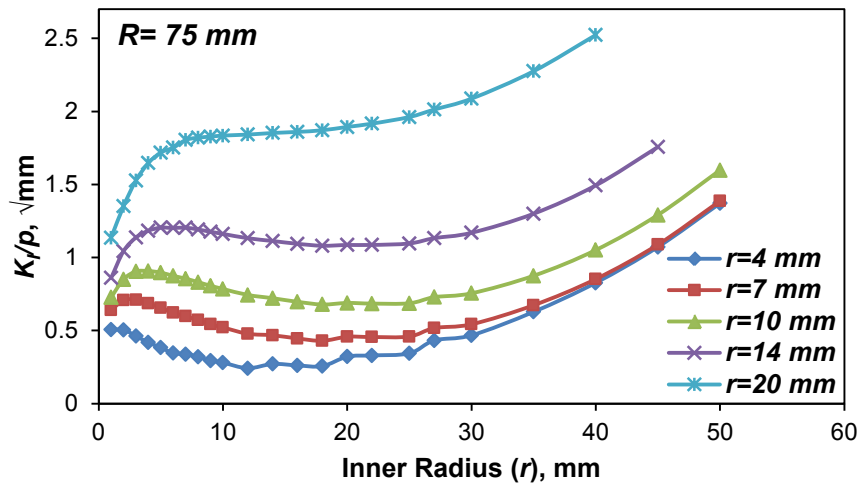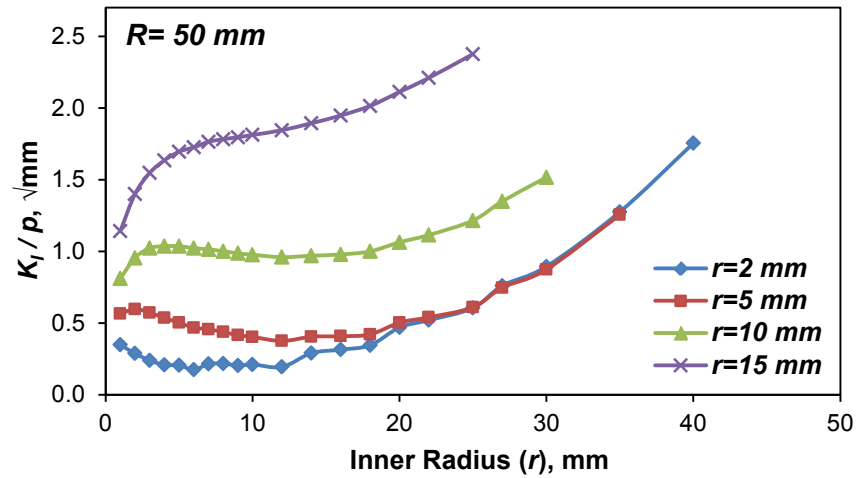
Figure 2.13. K_I Variation for IRT Specimens with Various Geometric Parameters
Note: p= pressure over the loading platens

After fitting numerous forms of equations to the FE data, Equation 2.32 was found to formulate the K_I data with a coefficient of determination (R^2) of 0.9956. It should be noted that Equation 2.32 can only be used to calculate the stress intensity factor of the IRT fracture specimen in the range of dimensions that were shown in Table 2.1.

$$K_I = \frac{F\sqrt{a}}{WB}\left[0.8772 - 11.2524\left(\frac{a.W^4}{R^5}\right) + 5.6104\frac{r}{W} - 10.4315\left(\frac{a}{W}.\frac{r}{R}\right)^{1.1549}\right]$$
$$\times \left[0.3 + \left[\left(0.65 - \frac{a}{W}\right)\left(1.5 - \frac{r}{R}\right)\right]^2\right] \times f\left(\frac{a}{W}\right)$$

[2.32]

and

$$f\left(\frac{a}{W}\right) = 1.3883 - 2.1476\left(\frac{a}{W}\right) + 20.1316\left(\frac{a}{W}\right)^2 - 29.5564\left(\frac{a}{W}\right)^3$$
$$+ 20.2896\left(\frac{a}{W}\right)^4$$

where

F = load on the IRT specimen

a = crack length

B = specimen thickness

R = outer radius

r = inner radius

$W = R\text{-}r$ = maximum fracture ligament

CHAPTER 3
DEVELOPMENT OF IRT TEST PROCEDURES

The ASTM E399 (2012) standard describes the test method for determination of the fracture toughness of metallic materials. This standard provides the K calibration formulae for several specimen geometries along with the test procedure and sample size requirements for each of those geometries. Similar to the specimen geometries specified in the ASTM E399, the K formula for the indirect ring tension (IRT) specimen, as shown in Equation 2-32, can be utilized to obtain the fracture properties in the linear elastic range. However, to use the IRT specimen geometry for fracture testing of HMA, a test procedure must be developed based upon the properties of HMA as well as the special characteristics of the test. Since asphalt materials also behave similar to linear elastic materials at low temperatures, the ASTM E399 standard was used as a baseline for developing the IRT fracture test for HMA mixtures.

In order to develop the proper test procedures and factors for the IRT HMA fracture test, a series of statistically-based laboratory experiments were conducted. The experiments demonstrated the capability of IRT HMA fracture test in discerning the properties of asphalt mixtures at low temperatures. The results obtained from the experimental plan were then used to recommend the optimum set of parameters and procedures for the IRT HMA fracture test.

3.1 Specimen Dimensions

One of the main advantages of the IRT fracture test is its practicality and ease of potential implementation with the existing equipment in most of the typical asphalt testing laboratories. In order to offer the test users a high level of flexibility, the K_I calibration formula for the IRT specimen was developed in such a way that it would cover a wide range of specimen dimensions. Nonetheless, to conduct a consistent set of tests and eliminate the specimen size effect, a set of dimensions was selected to be used for all of the test specimens in this study. The outer diameter of the IRT specimens was chosen to be 150 mm. This is the diameter of the standard Superpave gyratory compacted

specimens when fabricated in molds with a 150-mm diameter. Furthermore, asphalt field cores are often taken using core drills with 150-mm diameter; therefore this size of specimen is the best representative of the field and laboratory specimen geometry conditions. Additionally, most standard tests on disk-shaped HMA specimens use the 150-mm diameter samples, such as the indirect tensile strength (AASHTO T 322, 2007), and DC(t) fracture test (ASTM D7313 2013).

As for the inner radius of the IRT, a hole with a 26-mm diameter was found to be practical and satisfy the requirements of the fracture test. A 26-mm inner diameter can be conveniently cut using a 1-inch (25.4 mm) core drill (the final diameter of the hole would be 26 mm). Such an inner diameter in the ring would provide adequate space for a cutting device to generate the crack starter notches without damaging the circumference of the inner circular hole of the IRT specimen. Damage to the central hole during the cutting of the specimen notches should be avoided, as the presence of random damaged points in the central area of the specimen could cause stress concentrations beyond the notch zones, which would compromise the test results.

To simplify the fracture toughness calculations for the specimens in this experiment, the finite element modeling data were used to develop a simpler K equation for a specific set of specimen dimensions. For an IRT specimen with an outer diameter of 150 mm and an inner diameter of 26 mm, the stress intensity factor can be determined by:

$$K_I = \frac{F\sqrt{a}}{WB} \, f\left(\frac{a}{W}\right) \hspace{4cm} [3.1]$$

where

$$f\left(\frac{a}{W}\right) = 3.03 - 24.00\left(\frac{a}{W}\right) + 109.25\left(\frac{a}{W}\right)^2 - 261.88\left(\frac{a}{W}\right)^3$$
$$+ 311.28\left(\frac{a}{W}\right)^4 - 142.09\left(\frac{a}{W}\right)^5$$

where

F = load on the IRT specimen

a = crack length

B = specimen thickness

R = outer radius

r = inner radius

W = R-r = maximum fracture ligament

Equation 3.1 was developed by fitting a polynomial model to the calculated stress intensity factor values from the finite element models. This equation fits the FE data for specimens with 150-mm outer diameter and 26-mm inner diameter with a high coefficient of determination of 0.999 as illustrated in Figure 3.1. Similar to the Equation 2-32, the polynomial part of the Equation 3.1 is dimensionless.
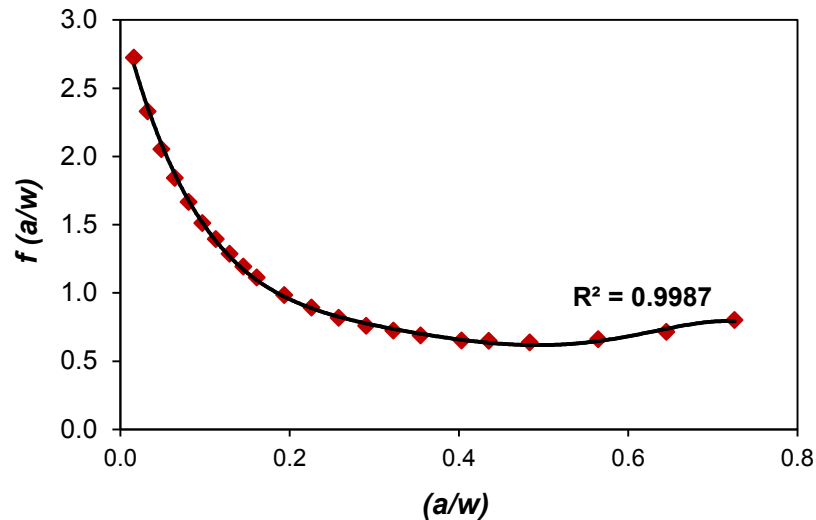
Figure 3.1. Fitting of the K_I Calibration Formula on the FE Data for IRT Specimens with R=75 mm and r=13 mm

3.2 HMA Materials

Two plant-produced hot-mix asphalt mixtures were used for the experiments. The experiments were designed to optimize the procedural factors of IRT fracture test for HMA materials. The mixtures, with a nominal maximum aggregate size (NMAS) of 9.5 mm, were collected from the construction site of two non-primary roads in Kentucky. The surface mixture for the KY85 road (Ohio County) was made with a polymer-modified PG 76-22 binder, whereas the surface mixture for the US60 road (Meade

County) was made with a neat PG 64-22. The HMA samples were collected from the hauling trucks before the paver and stored in 5-gallon metal buckets. The container buckets were sealed and stored in a temperature-controlled storage at about 24°C until the testing time. Each bucket contained 15 to 20 kg of asphalt mixture.

Two samples were taken from each mixture to test for the maximum theoretical specific gravity (G_{mm}) using the Rice test method and AASHTO T 209 (2011) standard procedure. The resulting G_{mm}'s were found to be within ±0.002 of the design G_{mm} value of the mixtures. Therefore, the design G_{mm} values were used for calculation of the air content of HMA specimens. Table 3.1 contains the design properties of KY85 and US60 mixtures.

Table 3.1. Mixture Properties

Property			KY85 Ohio County	US60 Meade County
Binder Grade			PG 76-22	PG 64-22
Asphalt Content (AC), %			5.9	5.8
Effective AC,%			5.5	4.8
Nominal Maximum Aggregate Size, mm			9.5	9.5
Maximum Specific Gravity (G_{mm})			2.445	2.465
Voids in the Mineral Aggregate (VMA), %			16.7	15.3
Voids Filled with Asphalt (VFA), %			75.7	73.0
	Sieve No.	Sieve Size, mm	Percent Passing	Percent Passing
	1/2"	12.5	100	100
	3/8"	9.5	95	92
	#4	4.75	72	56
Job Mix Formula (JMF)	#8	2.36	40	37
	#16	1.18	24	22
	#30	0.60	16	15
	#50	0.30	11	8
	#100	0.15	7	5
	#200	0.075	5.3	4.3

3.3 Specimen Preparation

As the asphalt materials age, they become more brittle due to oxidative reactions and loss of some lighter molecules. This embrittlement makes the asphalt mixtures stiffer, reduces their stress relaxation capability, and diminishes their healing properties (Asphalt Institute 2007). Consequently, asphalt mixtures become more susceptible to cracking as they age. Thus, aging the asphalt mixtures prior to running a cracking test leads to a more realistic evaluation of the cracking performance of the material at its most critical condition.

According to the current AASHTO R 30 (2002) standard procedure, to simulate the long-term aging of HMA samples, the compacted specimen should be placed in a forced-draft oven at 85°C for five days. However, recent studies have shown that more consistent results can be achieved by conditioning the loose mix samples at higher temperatures before compaction. A 24-hr conditioning at 135°C in a forced-draft oven has been recommended to simulate the aged conditions of HMA after seven to ten years of service in the field. This method has been successfully used in several research studies (Blankenship et al. 2010; Braham et al. 2009; Zeinali et al. 2014). Considering the advantages of this accelerated aging method, it was used in this research.

To fabricate the test specimens, the closed buckets containing loose mix collected from the field projects were reheated at 135°C until the samples became pliable enough for dividing. Next, the sample in each bucket was broken down into smaller portions by a sample splitting device (Figure 3.2a). Using this device would minimize the aggregate segregation during the splitting process and generate more uniform samples. The split samples were then spread in metal pans at a layer thickness of 2.5–5.0 cm. The pans were then placed in a forced-draft oven at 135°C for 24 hours ±2 minutes to simulate the long-term aging of the mixtures. After conditioning, the samples were compacted to a constant height of 150 mm using a Superpave gyratory compactor (SGC), and were let cool overnight. The weights of the compacted samples were adjusted to achieve final test specimens with 7.0±0.5% air voids content, which is typically used for performance testing of asphalt mixtures.

Finite element modeling and laboratory testing have shown that the plane-strain conditions can be assumed to be present in HMA specimens with a 50-mm thickness (Li and Marasteanu 2004). As Figure 3.3 illustrates, to fabricate IRT specimens, two 50-mm thick disk-shaped samples were cut from the mid-section of each gyratory sample. The top and bottom portion of the gyratory samples were discarded (Figure 3.2b) to avoid the density gradient caused by the loading plates in gyratory machines. These discarded portions typically have a higher density than the mid-section of the cylindrical sample. The disk-shaped specimens were cut using an automatic circular saw with digital measurement systems and high-speed diamond tip blade to produce a uniform set of specimens. Figure 3.3 schematically illustrates the fabrication of an IRT specimen from a gyratory compacted sample.

After cutting the disk-shaped specimens they were tested for bulk specific gravity using a CoreLok^{TM} machine and vacuum bags. As compared to the conventional bulk specific gravity test method in a water bath, sealing the specimen by a CoreLok™ method generates more accurate results, particularly for the specimens with higher air voids content. Based upon the measured bulked specific gravity and the design G_{mm} of the mixtures, the air voids content was determined for each disk-shaped specimen. In this study, an acceptable tolerance of ±0.5% from the target air voids content value was employed for all the specimens.
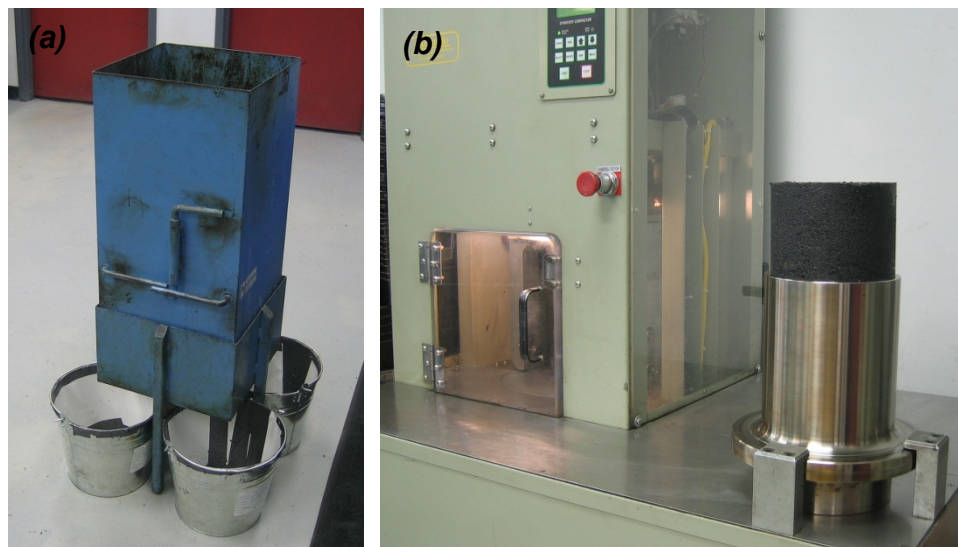
Figure 3.2. a) Sample Divider, b) Superpave Gyratory Compactor
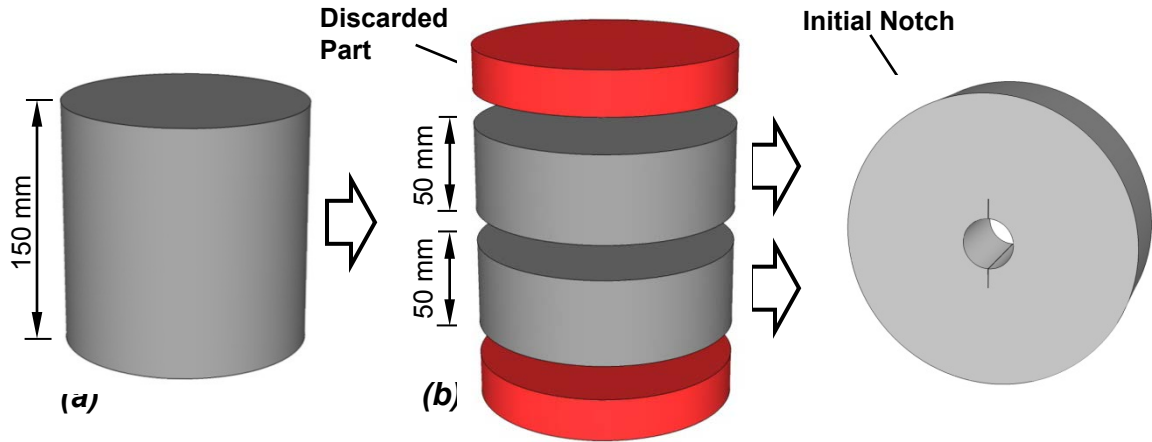
Figure 3.3. Fabrication of IRT Specimens: a) Gyratory Compacted Sample, b) Cutting the Disk-Shaped Specimens, c) Prepared IRT Specimen

HMA samples were cut under a stream of water to keep the temperature of the sample and cutting blade low. Consequently, the samples were soaked in water after each cutting. To ensure that the samples were completely dry before measuring their dry weight, their moisture was removed first by placing them in front of a fan, and then by a CoreDry™ device (Figure 3.4a). CoreDry™ dries the specimen by the means of a vacuum system and a cold trap. The drying process is done in consecutive cycles and after each drying cycle, the device weighs the specimen to find whether any moisture remains. This method ensures a completely dry sample in less than 30 minutes; whereas drying the specimens at the laboratory ambient conditions may take days, or sometimes weeks for samples with higher than 10 percent air voids content.

To cut the central circle of the IRT specimens, an automatic core drill machine with a diamond tip core bit was utilized, and its movement was controlled by a hydraulic system (Figure 3.5b). The central circle could also be drilled using a regular drill bit, however, A core drill device was preferred over the ordinary drill bit devices since the core bits would apply less pressure on the specimen body and do not impact the internal structure of the specimen.
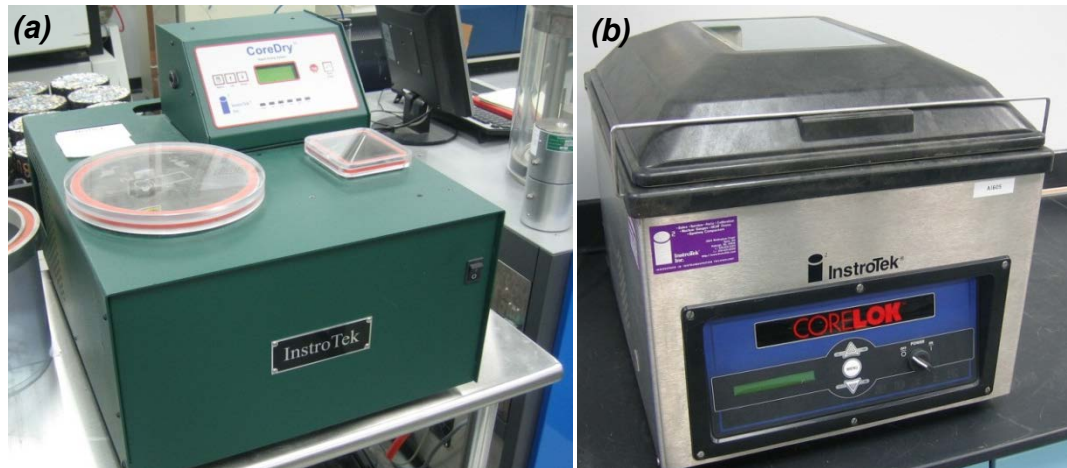
Figure 3.4. a) CoreDry™ Device, b) CoreLok™ Device
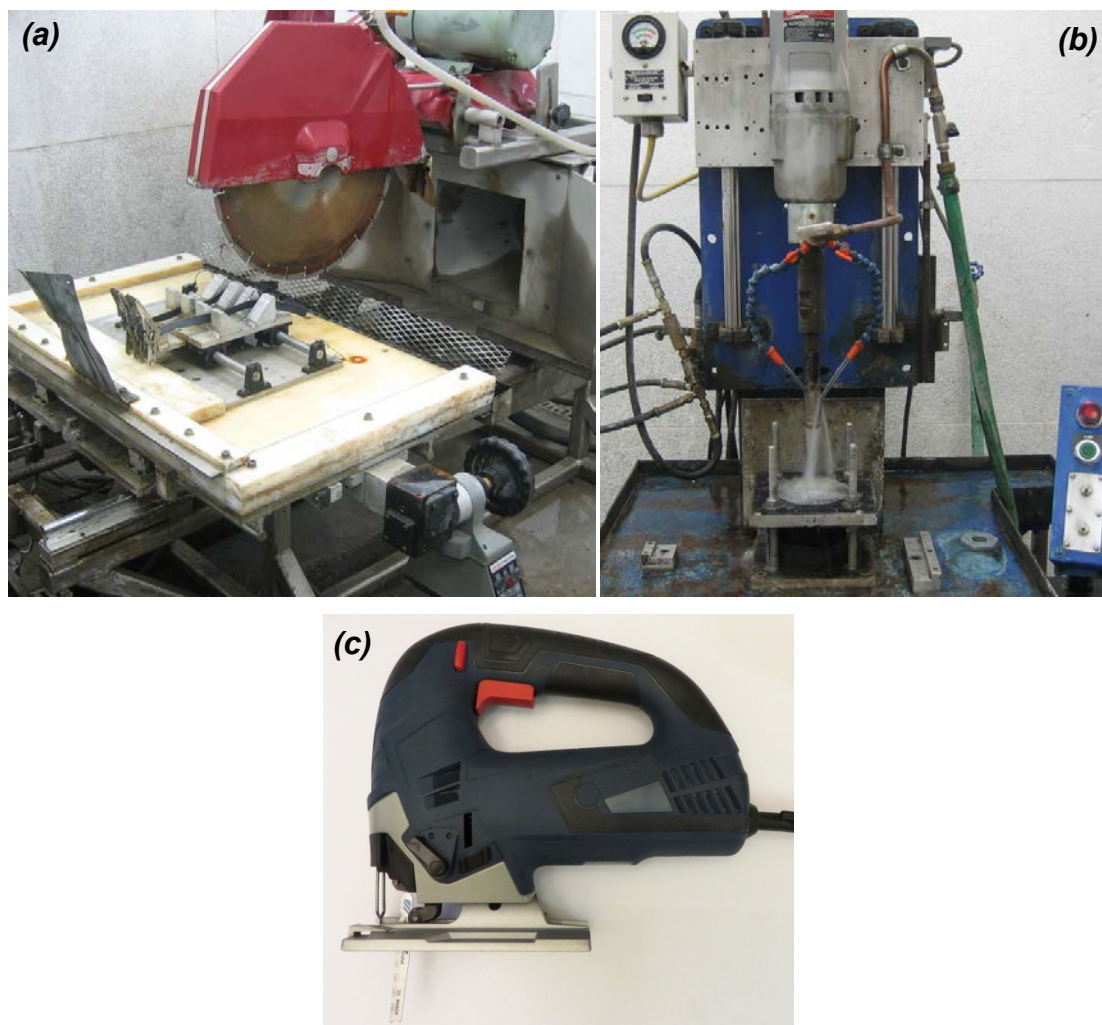
Figure 3.5. Equipment Used for Sample Preparation: a) Circular Saw, b) Core Drill, c) Jigsaw

After coring the central circle of the IRT specimen, the initial notches were cut inside the specimen along a randomly assigned diametric line. A hand-held jigsaw (Figure 3.5c) was used to generate the initial notches with the smallest possible width. A thin blade, which is typically used for cutting metals, was used to cut the notches. The final width of the notches after cutting was 1.0 to 1.2 mm. Figure 3.6 displays an IRT specimen after cutting the notches.

Figure 3.6. Fabricated IRT Specimen

3.4 Test Procedure

The fabricated specimens should be properly dried before testing. Existence of moisture in the HMA voids could potentially affect the fracture testing results at low temperature (Gubler et al. 2005; Xu et al. 2010; Mogawer et al. 2011). Thus, to achieve consistent results, it is recommended to ensure that all the test specimens are completely dry before testing. In this study, the prepared specimens were placed in a CoreDry^{TM} machine and dried on the day of testing. The attention paid to drying the specimen was critical in order to eliminate the influence of moisture on HMA fracture.

After drying, the specimens were conditioned in an environmental chamber for at least 3 hours so that the entire mass of the specimens reach the test temperature uniformly. The temperature of the specimens during the conditioning process was monitored using a dummy sample which was made with the similar geometry and materials as the test specimens. The dummy sample was instrumented with two thermocouples: one on the surface, and another one embedded at the center. The temperature readings from these thermocouples were monitored until both the surface and the core of the dummy specimen reached the designated test temperature. This method would ensure a uniform temperature distribution throughout the test specimens.

After temperature conditioning, the test specimen was placed in between the loading platens as displayed in Figure 3.7. A diametric line on the specimen, which was drawn for the proper placement of notches, was used to align the specimen direction with the loading line. The position of the specimen between the loading platens was stabilized by applying an initial load of about 100 N. Then, the test was started at the designated constant loading rate (e.g., in this study: 0.1, 1.0, and 10.0 mm/min). The loading continued until the complete splitting of the test specimen. During the test, the applied load and the load-point displacement data were recorded at 0.05-second intervals.
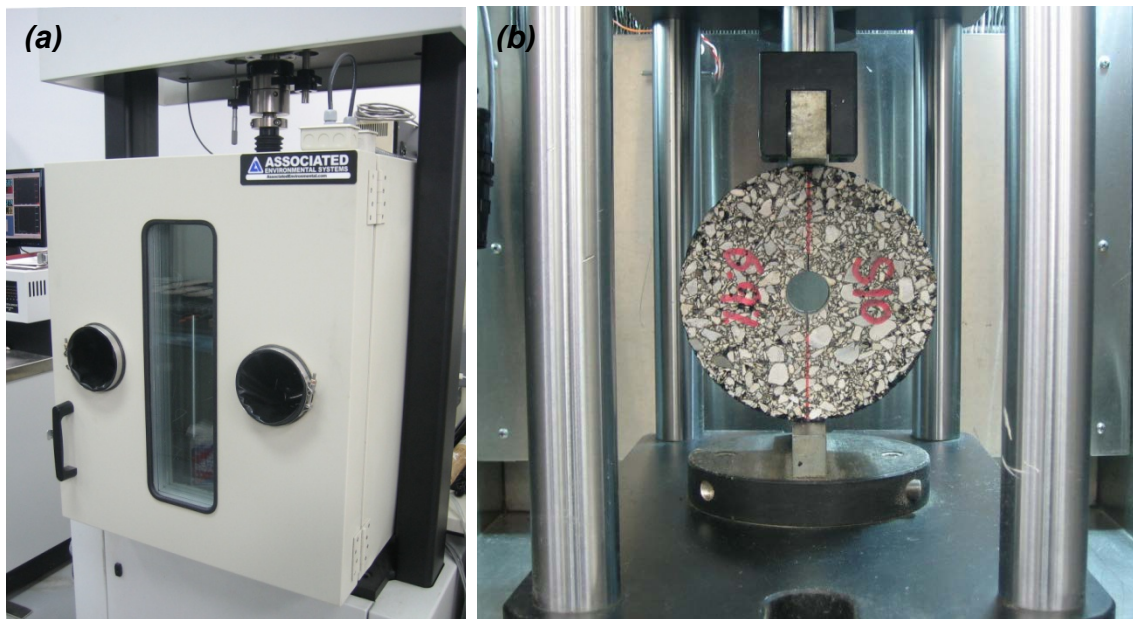
Figure 3.7. a) Universal Test Frame, b) IRT Specimen Placed in the Test Machine

Theoretically, the two notches on each specimen should be cut with exactly equal lengths through the pre-marked locations on two sides of the inner circle of the specimen. However, from a practical point of view, the final notch lengths may not be exactly the same. To account for this variation, the exact notch lengths were measured by a digital caliper after the fracture test was completed. As Figure 3.8b illustrates, the initial notch surface can be easily distinguished from the fracture surface after the test. To make an accurate measurement, one of the caliper tips was put against the notch tip without any movement and the other tip was aligned with the mouth of the notch in the internal circular hole. Three readings were made on each notch, and the average of 6 readings was used to represent the two notches in the calculations after the test. The measurements which were made by this method had a repeatability of about ±0.05 mm. In order to minimize the potential for adverse effects on fracture energy measurements due to specimen size effects, the notch length for all of the specimens was limited to a range between 8 and 12 millimeters in this study. Figure 3.8a shows an IRT specimen and the cracking pattern after the test.

Figure 3.8. a) Fractured IRT Specimen, b) Measurement of the Initial Notch Length

3.5 Fatigue Pre-Cracking

In calculation of the stress field in the vicinity of a crack, it was assumed that the crack was extremely sharp. Achieving such a sharp crack is not possible with typical laboratory cutting tools. To form a sharp crack in fracture testing specimens, the ASTM E399 (2012) standard requires fatigue pre-cracking of the notched specimens prior to the actual fracture test. In metals, the fatigue preloading causes the initial sharp crack tip to grow naturally and form a very sharp crack. For HMA specimens, however, the fatigue pre-cracking method is challenging due to the non-homogenous nature of the material. The fatigue loading would often result in formation of microcracks in the HMA and consequently undermine the structural integrity of the specimen.

To closely examine the effect of fatigue pre-cracking on IRT fracture testing, three trial specimens were fabricated (dimensions: *r=13 mm, R=75 mm, a=8 mm*) at 7.0±0.5% air voids content and subjected to fatigue loading at -12°C. On one of the specimens, the notches did not grow symmetrically and it could not be used for fracture testing. Two out of three specimens showed acceptable crack growth patterns on both of their notches. However, hysteresis loops were formed in the load-displacement curves, and the measurements after the fatigue loading revealed that the specimens had experienced a significant permanent deformation. The vertical diameter of the specimens (along the loading direction) reduced from 150 mm to 147 mm, and the horizontal diameter increased to about 151.5 mm. Moreover, the cracking patterns of the fatigue pre-cracks were somewhat deviated from the vertical loading line, which could affect the accuracy of the test. The IRT fracture test results on the specimens with fatigue pre-cracking were found to be more scattered and inconsistent as compared to the specimens without fatigue pre-cracking. Based on this trial experiment, it was decided to conduct the experimental plan on specimens with only saw-cut notches and without fatigue pre-cracking. By excluding the fatigue pre-cracking from the test procedure, it was assumed that the randomly distributed voids and flaws in the HMA would form starter microcracks, which would coalesce later into a larger crack in the specimen.

3.6 Fracture Calculations

3.6.1 Calculation of Fracture Toughness

The data from the test was utilized to plot the load versus load-point displacement during the test. ASTM E399 standard explains three types of load-displacement curve for linear elastic materials as presented in Figure 3.9. Based upon the type of fracture and load-displacement curve, the onset of crack propagation is determined, and the associated load is used for calculation of the material's fracture toughness. The numerous tests that were conducted for the present research revealed that the resulted curve from IRT fracture testing of HMA specimens at low temperatures matches the type-II fracture curve in the ASTM E399 standard.

FIG. 7 Principal Types of Force-Displacement (CMOD) Records
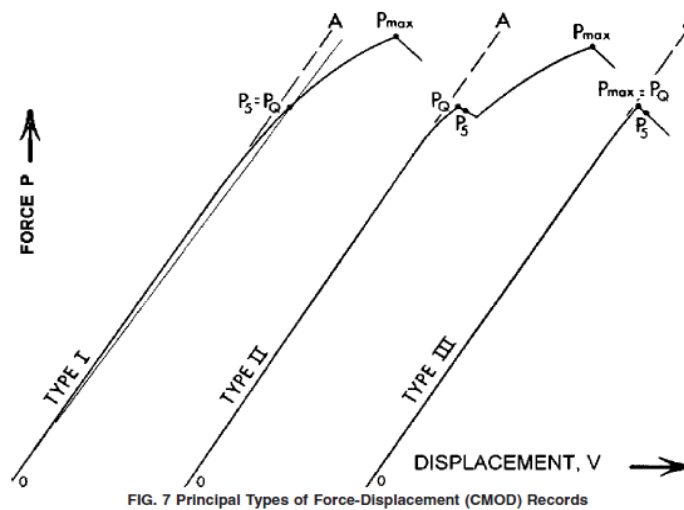
Figure 3.9. Three Fracture Types for Linear Elastic Materials (ASTM E399 2012)

A typical load-displacement curve from an IRT fracture test data trace at the asphalt binder's lower PG temperature is shown in Figure 3.10. As illustrated in this figure, an initial hardening phase was observed at the beginning of all the test data. Such hardening phase typically occurs at the beginning of the IDT strength test as well. During this phase, the compliance of the specimen decreases by increasing the load. According to the ASTM E399 standard, it is normal to observe some levels on nonlinearity at the beginning of the test. This nonlinearity also depends on the test geometry and loading configuration. The initial nonlinearity can be removed from the data by preloading the

specimen, and running the test in the linear portion. The other method is to run the test without pre-loading and account for the nonlinearity after the test. The latter was used in this study since it provides more accuracy for calculating the fracture energy.
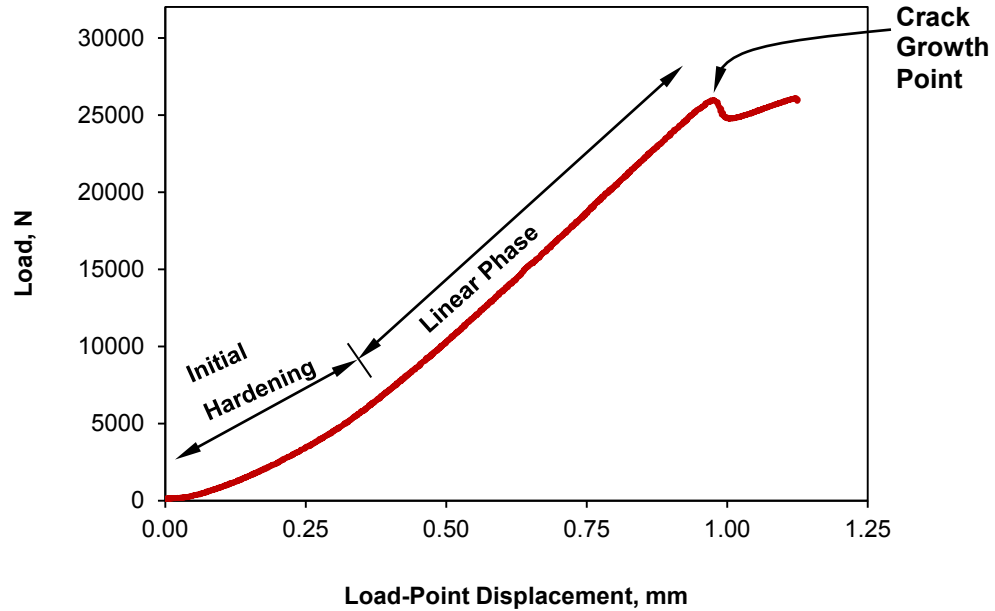
Figure 3.10. Typical IRT Fracture Test Data for HMA

After the initial hardening phase, the linear phase begins and the compliance of the specimen remains constant. During this phase the load magnitude increases with a linear relationship with respect to the load-point displacement. By increasing the load, the stress intensity factor (K_I) of the specimen increases, and as it reaches the critical K_{IC} value, the notch starts growing into the unbroken ligament portion of the fracture zone. At this point, the load-displacement curve exhibits a sudden drop which makes the crack growth moment easily distinguishable in the IRT fracture test data (Figure 3.10). As the loading platens continue to move at the designated displacement rate, the applied load on the specimen increases until the specimen completely fractures along the vertical loading line.

The peak load (P_Q) before the abrupt drop in the compressive load should be used for calculating the fracture toughness of the HMA. By entering this peak load and the geometry parameters into the Equation 2-32 (or Equation 3-1 for the special geometry

used in this experimental study), the plane-strain fracture toughness is determined. To have a valid linear elastic fracture, ASTM E399 requires that for the P_{max}/P_Q ratio should not exceed 1.10. The data collected from the IRT fracture test on HMA samples revealed that this ASTM E399 requirement was met. As illustrated in Figure 3.8a, the IRT fracture test produces a relatively straight crack pattern on a consistent basis. This straight crack pattern generates a mode-I fracture throughout the test, and prevents mixed-mode crack propagation.

3.6.2 Calculation of Fracture Energy

In addition to the fracture toughness, the normalized fracture energy from the load-point displacement can also be determined from the IRT fracture test. In order to do so, the consumed energy during the test is determined by calculating the area under the load versus load-point displacement curve as depicted in Figure 3.11. Then, the fracture energy is normalized by dividing the calculated fracture energy by the fracture ligament area of the specimen, which is equal to *2B(W-a)*. Normalization of the fracture energy helps decrease the effect of specimen size and initial notch length.
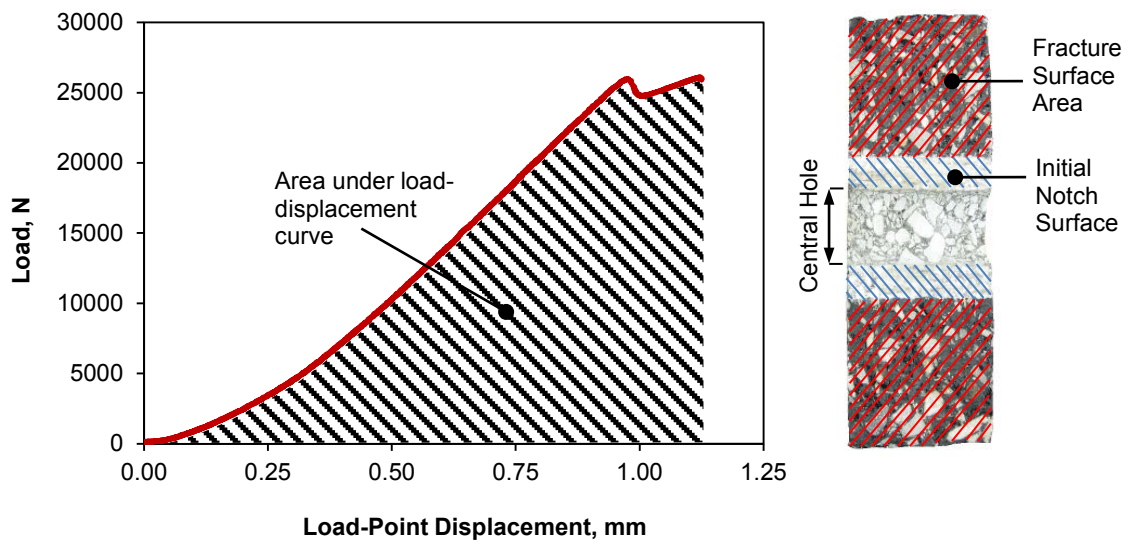
Figure 3.11. Calculation of the Normalized Fracture Energy

The fracture energy calculated by this method is not considered as a broad property of the material, and it is sensitive to the changes in mixture stiffness. However, research studies on field performance of asphalt pavements have shown that the energy obtained from the fracture tests on HMA can correlate well with the field cracking performance (Wagoner et al. 2006; Zou et al. 2013). Correlation of the fracture energy test data to the cracking performance of the pavement is typically conducted by running the test on core samples obtained from the pavement, and correlating the test results to the field cracking survey data.

3.7 Effects of Loading Rate

The response of HMA material to loading is highly dependent on the speed of applying the load (Asphalt Institute 2001; Witczak et al. 2002). To correctly characterize the material properties with a performance test, the loading rate of the test should represent realistic field conditions. Furthermore, the test duration and consistency of the results are among the factors which are taken into consideration when the optimal loading rate of a test is evaluated.

In this study, an experimental approach was used to optimize the optimal loading rate for the IRT fracture test. This experimental procedure involved conducting the IRT fracture test on nine HMA specimens from the KY85 mixture (Table 3.1) at three loading rates: 12.5 mm/min, 1.0 mm/min, and 0.1 mm/min. The 12.5 mm/min is considered as a relatively fast loading rate for high strain testing, which is used for the indirect tensile strength test (IDT) of HMA, and has been standardized under AASHTO T 322 (2007) and ASTM D6931 (2012). The IDT strength test has been extensively used to determine the tensile strength of Superpave mixtures at low and intermediate temperatures. The 1.0 mm/min is a moderate loading rate recommended by the ASTM D7313 (2013) for DC(t) fracture testing of HMA. The DC(t) test is conducted in the tension-bending mode and its configuration is essentially different from the IRT test; however, the 1.0 mm/min could be considered as an intermediate loading rate for the IRT test. Finally, the 0.1 mm/min rate was tested to evaluate the material's behavior at a very slow loading rate. The tests for loading rate evaluation were conducted at -12°C (10°C higher than the low PG

temperature of the binder). The data from tests for loading rate evaluations are depicted in Figure 3.12. The calculated values for the IRT fracture toughness and fracture energy of the specimens are presented in Table 3.2 and Table 3.3, respectively.

All of the specimens that were tested for various loading rates (Figure 3.12) exhibited a sudden failure at the end of the test. The Tukey Honestly Significant Difference (HSD) method was used to perform statistical pairwise comparisons on the fracture toughness data with various loading rates. Tukey's method compares all possible pairs of means in the data while it corrects the results for the experiment-wise error rate, which occurs as the consequence of running multiple comparisons on the data. The pairwise comparisons revealed that the resulted K_{IC} values at the 12.5 mm/min and 1.0 mm/min were not significantly different. However, as the loading rate decreased to 0.1 mm/min, the measured fracture toughness value decreased significantly.

At the 12.5 mm/min loading rate, one out of the three tested specimens failed immediately after the crack growth initiation. This specimen is identified as S2 in Figure 3.12a. On the other hand, the other two specimens exhibited failure loads higher than the load at the crack growth initiation point (Figure 3.12a). This non-uniformity in the failure of the specimens resulted in a higher variation in the calculated normalized fracture energy as can be seen in Table 3.3. By applying the loading rate of 1.0 mm/min, the failure mode seemed to be more repeatable, and more uniform data was obtained. Furthermore, the obtained fracture toughness and fracture energy at 1.0 mm/min, as presented in Tables 3.2 and 3.3, had the lowest coefficient of variation. The IRT tests at the 1.0 mm/min loading rate typically took 1 to 1.5 minutes to run.

Further decreasing the loading to 0.1 mm/min extended the test duration to more than 12 minutes. At this slow loading rate, the response of the specimens seemed to be affected by the HMA creep, and more variation was observed in the resulting fracture toughness values. Generally, when a test is developed to characterize a certain property of the material, the test procedure is developed in such a way to restrain the variations in the test data to the level of interest, and isolate all the other interfering variables. During this experimental study none of the IRT fracture tests at 0.1 mm/min would confound the variations in the fracture factors with the variability caused by the HMA creep and time-dependent loading.

Table 3.2. Calculated Fracture Toughness of the Specimens with Various Loading

Load Rate (mm/min)	Sample ID	Notch Length (mm)	Air Voids (%)	Max Load (N)	$f(a/W)$	K_{IC} (MPa$\sqrt{mm}$) Test Value	Average	CV
	S1	12.04	6.7	26458	0.970815	28.75		
12.5	S2	10.76	6.7	27746	1.042351	30.60	29.42	3.5%
	S3	10.34	7.1	26054	1.069644	28.91		
	S4	10.00	7.0	26591	1.096197	29.68		
1.0	S5	9.22	6.9	26690	1.153500	30.16	29.55	2.3%
	S6	10.36	7.1	25975	1.068296	28.81		
	S7	10.29	6.7	23469	1.073033	26.06		
0.1	S8	10.02	7.1	21857	1.091881	24.37	25.73	4.8%
	S9	10.05	6.6	24002	1.089741	26.75		

Note: Mix ID: KY85, test temperature= -12°C, R=75 mm, r=13 mm, B=50 mm

Table 3.3. Calculated Fracture Energy for Specimens with Various Loading Rates

Load Rate (mm/min)	Sample ID	Notch Length, (mm)	Air Voids (%)	Fracture Surface Area (mm^2)	Area under the Curve (N.mm)	Normalized Fracture Energy (J/m^2) Test Value	Average	CV
	S1	12.04	6.7	4996	14199	2842		
12.5	S2	10.76	6.7	5124	11646	2273	2759	16%
	S3	10.34	7.1	5166	16340	3163		
	S4	10.0	7.0	5204	16284	3129		
1.0	S5	9.22	6.9	5278	14522	2751	2894	7%
	S6	10.36	7.1	5164	14469	2802		
	S7	10.29	6.7	5171	14298	2765		
0.1	S8	10.02	7.1	5198	13339	2566	2778	8%
	S9	10.05	6.6	5195	15600	3003		

Note: Mix ID: KY85, test temperature= -12°C, R=75 mm, r=13 mm, B=50 mm
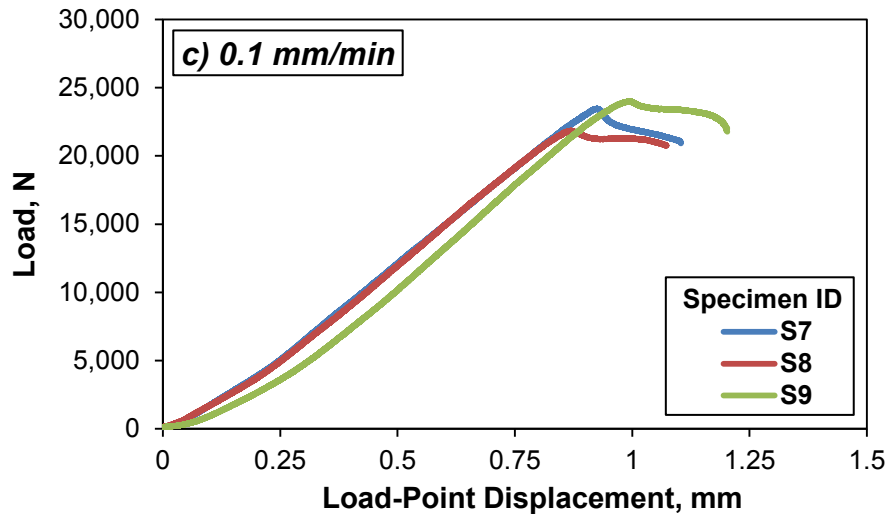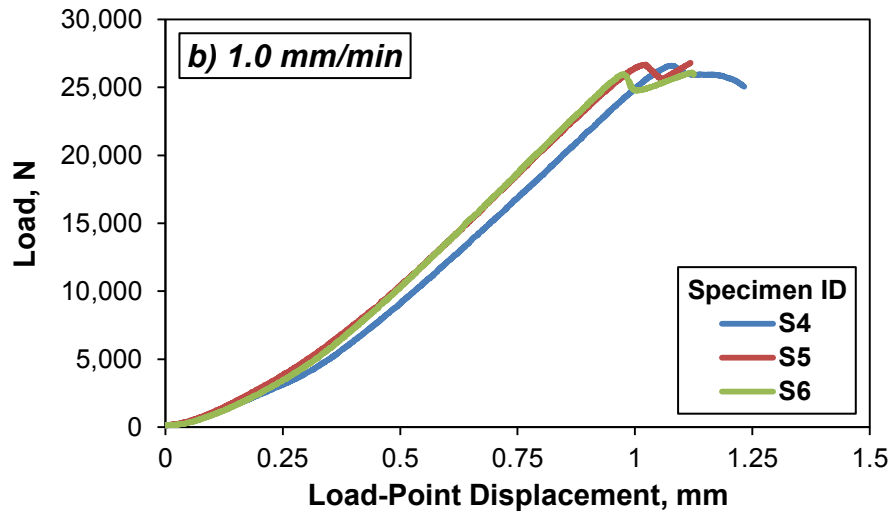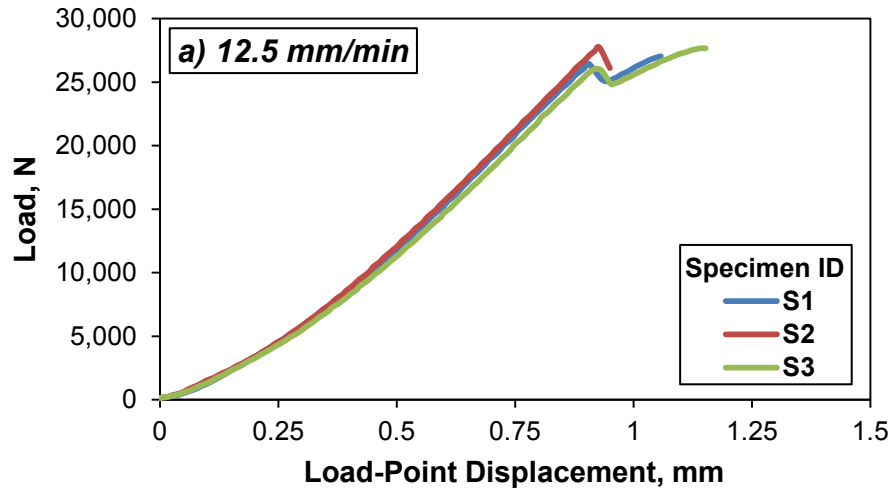
Figure 3.12. IRT Fracture Test Data at various Loading Rates: a) 12.5 mm/min, b) 1.0 mm/min, c) 0.1 mm/min

In summary, the 12.5 mm/min loading rate seemed to be too fast for IRT fracture test, and HMA material exhibited artificially high brittleness in some cases. On the other hand, the 0.1 mm/min loading rate seemed to be too slow to the degree that the effect of specimen creep was confounded with the elastic fracture of the HMA. Based on these studies, it was concluded that the 1.0 mm/min loading rate is more suitable for the IRT fracture testing of HMA. The variability in the test was lower at this rate, and uniform specimen failure patterns were observed. Based upon this finding, the rest of the testing plan at various temperatures was conducted at the 1.0 mm/min loading rate.

3.9 Effects of Test Temperature

After optimizing the loading rate for IRT fracture test, a series of tests were performed on KY85 and US60 mixtures (Table 3.1) at various temperatures to examine the sensitivity of the IRT fracture test to the specimen temperature. The test temperatures were selected to be -22°C (exactly at the binders' low temperature grade), -12°C, and -2°C (at 20°C and 10°C higher than the low temperature end of the binder grade, respectively). Triplicate specimens with outer diameter of 150 mm and inner diameter of 26 mm were fabricated and tested per each mixture and test temperature. Based upon the findings of the loading rate study, all of the experiments for the study of the test temperature were performed at 1.0 mm/min loading rate.

The load-displacement data for the KY85 specimens at -2°C, -12°C, and -22°C are presented in Figure 3.13. These charts demonstrate how the IRT test responds to the variations in the test temperature. It should be noted that the differences between the data traces of a set of specimens conducted under similar test temperatures is partially due to the differences between their initial notch lengths. However, this difference was considered in the fracture toughness calculations by employing Equation 2-32. In addition, the fracture energy of the specimens was normalized by diving to the fracture surface area. This normalization reduced the effect of differences between the initial notch lengths of the specimens.
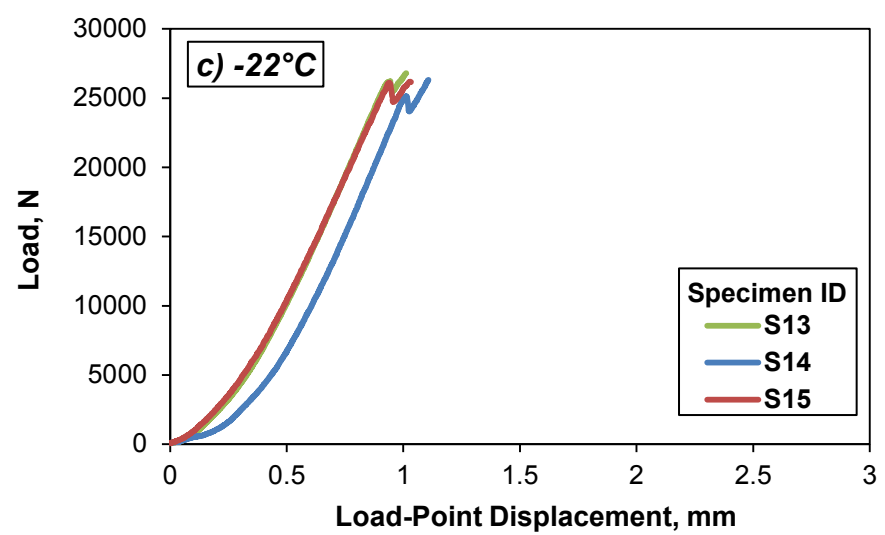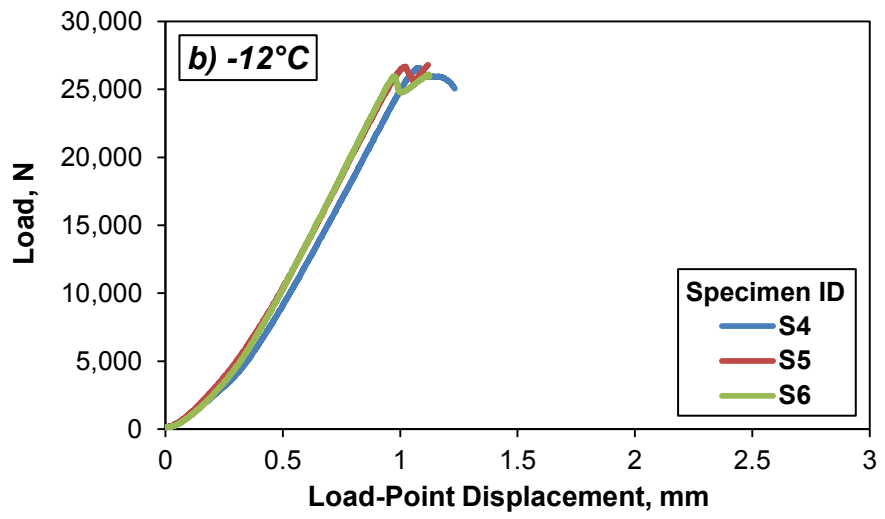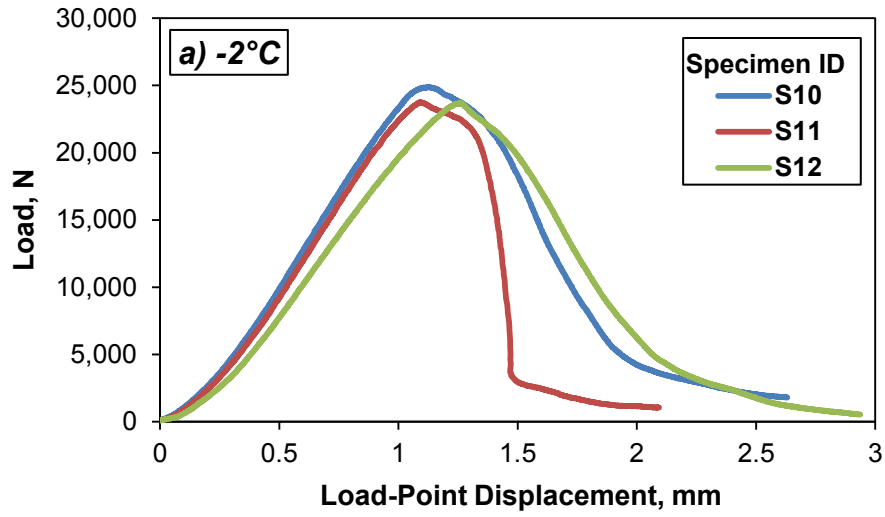
Figure 3.13. IRT Test Data at various Temperatures: a) -2°C, b) -12°C, c) -22°C
Note: Mixture ID: KY85, loading rate= 1.0 mm/min

The experiment revealed a noteworthy capability of the IRT fracture test in distinguishing the transition of the mixtures into their quasi-brittle phase. At -2°C, as depicted in Figure 3.13a, the specimens did not show a sudden failure at the end of the test. At this point, the HMA specimens have not entered the quasi-brittle phase yet. Therefore, the specimens did not show a linear elastic fracture, and the specimens experienced significant deformation. Consequently, after the initial propagation, the crack did not exhibit a sudden growth and propagated gradually into the unbroken ligament. In fact, at this temperature, liner elastic fracture toughness cannot adequately describe the fracture of the HMA material, and a significant portion of the energy was spent on plastic deformation around the crack tip as it grew. As the temperature was lowered and the HMA entered its quasi-brittle phase, the failure mode changed into a sudden crack growth. This property of the IRT fracture test could be utilized to evaluate the transition of the HMA to the glassy and quasi-brittle phases.

This capability of clearly demonstrating the transition of the mix from ductile to brittle phase has not been observed in most HMA fracture tests. It is noteworthy to mention that the cracking performance of asphalt pavements is highly dependent on ductility of HMA material and the mixture's potential for relaxing the traffic and environmentally induced loads. This capability of the IRT fracture test can be used as a powerful tool to help with the prediction of field performance of asphalt pavements.

Table 3.4 and Figure 3.14 present the measured plane-strain fracture toughness values for KY85 and US60 mixture at various test temperatures. The IRT fracture test showed a high repeatability for both mixtures with a coefficient of variation (CV) of 2.3 to 4.0 percent. All the specimens tested in this study exhibited a similar stable and well behaving crack growth patterns. The configuration of the IRT test distributes the stresses in the specimen in such a way that the initial notch helps with the propagation exactly along the vertical diametric loading line. Consequently, a uniform fracture and crack pattern was induced, which enhanced the repeatability of the test. Moreover, this uniform crack growth pattern produces a relatively pure Mode-I fracture on a consistent basis, and prevents mixed-mode fracture which often results from crack pattern deviating from the straight line. This is another advantage of the IRT fracture test to the other HMA fracture tests.

The Tukey pairwise comparison method was used to compare the fracture toughness values of the mixtures. The results of these analyses were similar for both mixtures. The fracture toughness of KY85 and US60 mixtures increased significantly as the test temperature reduced from -2°C to -12°C. However, further decreasing the temperature (from -12°C to -22°C) did not significantly change the fracture toughness. In the final analysis, the fracture toughness of the KY85 mixture was significantly higher than the US60 mixture at all of the tested temperatures.

Table 3.4. Fracture Toughness of the Mixtures for Various Testing Temperatures

Mixture	Test Temp., °C	Average Air voids, %	K_{IC}, MPa√mm	Coefficient of Variation
	-2	6.9	26.61	2.8%
KY85	-12	7.0	29.54	2.3%
	-22	7.0	28.63	2.9%
	-2	6.9	24.57	4.0%
US60	-12	7.0	26.86	2.3%
	-22	7.0	27.13	2.6%

Note: Loading rate= 1 mm/mn, R=75 mm, r=13 mm, B=50 mm
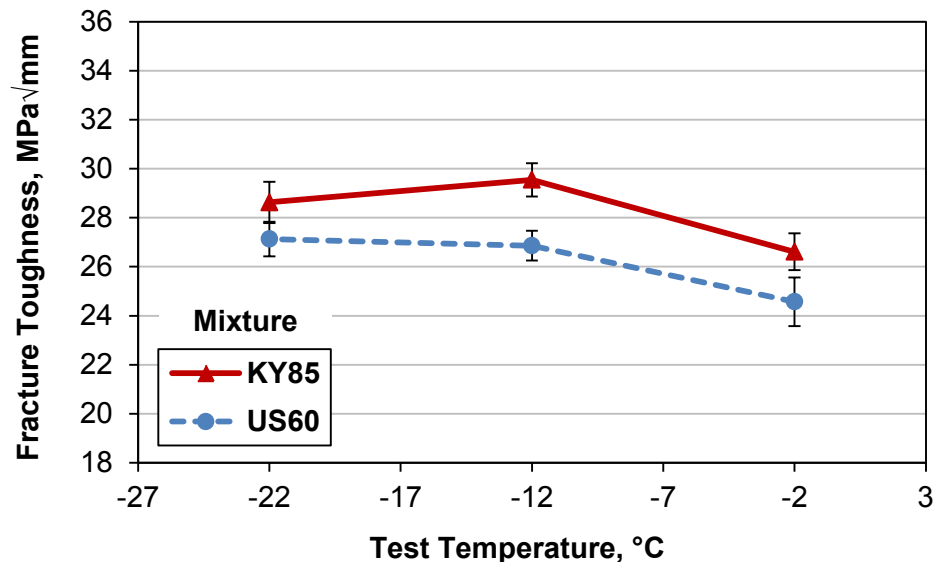
Figure 3.14. Variation of the Plane-Strain Fracture Toughness versus Test Temperature
Note: Error bars= 2×standard deviation

The fracture energy from the load-point displacement was also calculated for this set of specimens. As presented in Table 3.5, a low variation was observed in the fracture energy data at -12°C and -22°C as well (a coefficient of variation of 3 to 7 percent). However, the resulted fracture energy showed a higher variation at -2°C testing temperature. This is due to the different fracture mode at -2°C and the variations in the tail portion of the data trace. In general, the coefficient of variation for the IRT fracture test was lower than the values determined by other currently in use HMA fracture tests, which can often range as 3–27 percent for SE(B) test as reported by Mobasher et al. (1997); 15–34 percent for SCB test as reported by Li and Marasteanu (2004); and 5–25 percent as shown in the research by Wagoner et al. (2005b) and Clements et al. (2012). As Figure 3.15 displays, the fracture energy of the mixtures decreased by lowering the test temperature. The linear regressions analysis indicated that for every 1°C decrease in the test temperature, the IRT fracture energy of the KY85 and US60 mixtures decreased on average by 135 and 95 J/m^2, respectively.

Overall, mixture KY85 exhibited a better laboratory performance at low temperatures. According to the IRT fracture test results, KY85 mixture is expected to show a higher ductility, better resistance to crack growth, and an overall higher performance at low temperatures. It should be noted that both mixtures were made with PG XX-22 binders. The results of asphalt binder testing would suggest a similar performance for both of them at low temperatures. However, the IRT fracture test captured the slight difference between the fracture properties of the mixtures which could stem from the other mix properties such as aggregate-binder bond, aggregate strength, percentage of fine materials, and aggregate shape to name a few. Obviously, field studies would be required to verify such cracking performance predictions.

Table 3.5. Normalized Fracture Energy of the Mixtures at Various Temperatures

Mixture	Test Temp., °C	Average Air voids, %	Normalized Fracture Energy, J/m^2	Coefficient of Variation
KY85	-2	6.9	5024	18%
	-12	7.0	2895	7%
	-22	7.0	2315	3%
US60	-2	6.9	3872	14%
	-12	7.0	2729	7%
	-22	7.0	1975	3%

Note: R=75 mm, r=13 mm, B=50 mm
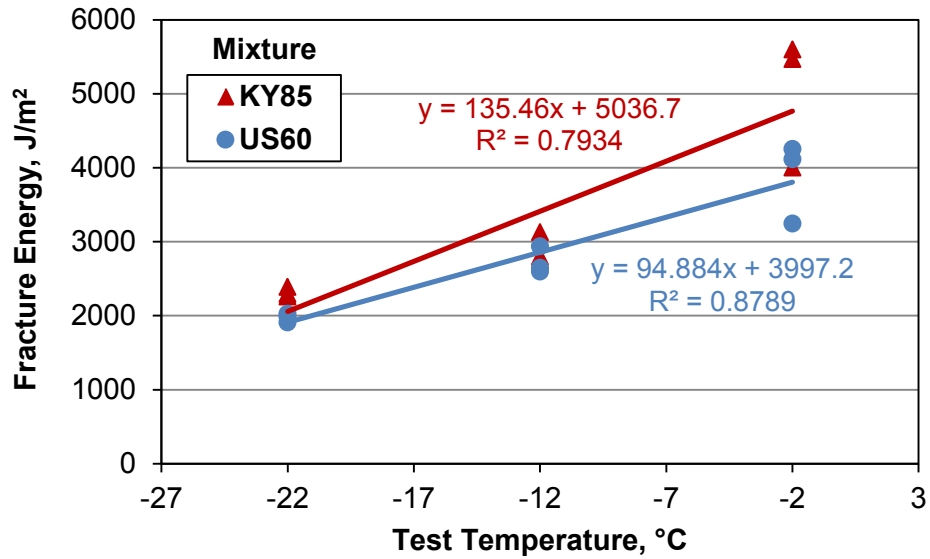
Figure 3.15. Variation of the Normalized Fracture Energy with Test Temperature

CHAPTER 4
CRACKING SUSCEPTIBILITY ANALYSIS

The indirect ring tension (IRT) fracture test showed a strong capability in discerning the difference between the HMA mixtures at low temperatures. However, the HMA materials in the field are not always exposed to a constant low temperature. Typically, cooling of an asphalt pavement starts at mid-temperatures, and as the pavement temperature decreases, the HMA layer on top of the pavement contracts. On the other hand, the HMA layer is physically restrained by its friction forces mobilized between the pavement and its base as well as the adjacent asphalt layer in the longitudinal direction. Consequently, the temperature drop causes a tensile stress in the HMA layer which is the main cause behind the low-temperature cracking of asphalt pavements.

The pavement temperature does not necessarily change at the same rate as the ambient temperature. Additionally, the temperature of a point within an HMA layer depends on the pavement temperature gradient as a function of depth. Nonetheless, the temperature drop is most rapid at the pavement surface. Consequently, the highest thermal stresses are typically formed near the pavement surface, and that is where the thermal cracks grow first. A comprehensive climatic model was developed during the SHARP program (Lytton et al. 1990), which estimated the temperature profile, moisture content, and freeze/thaw depth throughout the entire pavement layers. This model was later enhanced (Larson and Dempsey 1997) and incorporated into the Mechanistic Empirical Pavement Design Guide (MEPDG) (Zapata and Houston 2008). This model can be used to estimate the temperature drop at various depths of the HMA layer and estimate the cracking susceptibility as a function of depth.

As a viscoelastic material, asphalt's response to loading is a function of its temperature and loading time. When the temperature is higher or the loading rate is slower, HMA is better capable of relaxing the stresses. Conversely, at lower temperatures or faster loading rates (faster temperature drop), the HMA relaxes less and it may crack. In summary, not only the low-temperature performance of an asphalt pavement is a function of its fracture resistance, but also heavily related to its stress relaxation properties.

To better correlate the IRT fracture test data to the actual low-temperature performance of the HMA mixtures, an analytical method was developed in this part of the study. First, a viscoelastic model was developed to estimate the thermally induced tensile stresses at the surface of the asphalt pavements. Next, the creep compliance of the mixtures at low temperatures was measured through laboratory testing. Then, by incorporating the creep test data into the viscoelastic model, the thermally-induced tensile stresses were estimated for the pavements in the study. Finally, the IRT test data was utilized in conjunction with the thermal stress data to determine the cracking susceptibility of asphalt pavements in this study.

4.1 Linear Viscoelastic Model

Hot mix asphalt (HMA) has traditionally been assumed to have linear viscoelastic behavior at low temperatures (Roque and Buttlar 1992; Christensen 1998; Dave et al. 2010). HMA, as a viscoelastic material, is capable of relaxing some of its internal stresses if the load is applied at a slow rate. Therefore, neglecting the relaxation properties of HMA in stress analysis results in estimation of stresses that may be unrealistically too high. The relaxation modulus is expressed by the following equation:

$$E_{rel}(t) = \frac{\sigma(t)}{\epsilon_0} \qquad (4.1)$$

where:

$E_{rel}(t)$ = stress relaxation modulus function

t = loading time

$\sigma(t)$ = stress function

ϵ_0 = initial test strain

To determine the relaxation modulus of a material, it is subjected to a constant strain and the resulting stress is measured over time. This test method is cumbersome for HMA material, and instead, the creep compliance of HMA is determined through a creep test. The creep compliance is given by:

$$C_{crp}(t) = \frac{\epsilon(t)}{\sigma_0}$$
(4.2)

where:

$C_{crp}(t)$= creep compliance function

t = loading time

$\epsilon(t)$= strain function

σ_0= initial test stress

In the creep test, a constant load is applied to a specimen and the strain is measured by recording the specimen deformation over time. In fact compliance is a convenient way of characterizing the stiffness of a material.

Since the response of a viscoelastic material is related to both time and temperature, the creep compliance test of HMA must be conducted at various temperatures and long loading times in order to provide a comprehensive understanding of the stiffness behavior at different conditions. To do this, the creep test is typically conducted at different temperatures, and the time-temperature superposition principle of the viscoelastic materials is applied to build a creep master curve (Christensen 1968). By using this principle, several creep-versus-time curves for a single material in log-log scale can be shifted relative to loading time and construct a single master curve. This master curve can then be used in conjunction with the proper shift factors to characterize the creep compliance properties at various temperatures and loading durations.

In this study, a power law model was fitted to the final creep compliance master curve data in the following form:

$$C_{crp}(t) = D_0 + D_1 t^m$$
(4.3)

where:

$C_{crp}(t)$= creep compliance at time t

D_0, D_1, m = constants in the power law model

Furthermore, an Arrhenius type function in the following form was employed to describe the variation of shift factors with respect to temperature:

$$log(a_T) = a_0 + a_1 \left(\frac{1}{T} - \frac{1}{T_{ref}} \right)$$

(4.4)

where:

a_T = shift factor at temperature T

a_0, a_1 = Arrhenius function constants

T = test temperature in degrees Kelvin (°K)

T_{ref} = reference temperature at which the master curve is constructed (in °K)

A time-temperature shift factor $a_T(T)$ is defined as the horizontal shift that must be applied to the response curve of $C_{crp}(t)$, which is measured at an arbitrary temperature T in order to move it to the curve measured at the reference temperature T_{ref}. This can be formulated as:

$$\log a_T = \log t(T) - \log t(T_{ref})$$

(4.5)

where:

a_T = shift factor at temperature T

$t(T)$ = loading time at temperature T

$t(T_{ref})$ = loading time at temperature T_{ref}

While the Williams-Landel-Ferry (WLF) equation has been used for viscoelastic modeling of HMA in some studies (Christensen and Anderson 1992; Christensen 1998), an Arrhenius type function was used in this research since it has shown better performance for viscoelastic modeling of HMA at low temperatures (Rowe et al. 2001; Rowe and Sharrock 2001). When the temperature is constant, Equation 4.5 can be used to easily determine the effective time. However, in the case of a temperature drop in an asphalt pavement, the temperature varies as a function of time, therefore a_T becomes an implicit function of time:

$$T = T(t) \tag{4.6}$$

In this case, the effective time for continuous functions can be written as:

$$t' = \int_0^t \frac{d\xi}{a_T(\xi)} \tag{4.7}$$

where ξ is a dummy time variable. It should be noted that this approach only accounts for the variation of temperature as a function of time. Other factors such as damage due to applied stress, or environmental exposure can accelerate or retard the rate of given response and should be applied into the model separately. By using the Equation 4.4 as the shift factor function, the effective time in Equation 4.7 yields:

$$t' = 10^{\left(\frac{a_1}{T_{ref}} - a_0\right)} \int_0^t \frac{d\xi}{10^{\left(\frac{a_1}{T_i} + r\xi\right)}} \tag{4.8}$$

where:

t' = effective time

t = time from the beginning of cooling

T_i = the initial temperature from which the cooling starts

r = cooling rate (°C/hr)

ξ = dummy time variable

Equation 4.8 is based upon the assumption of a pavement cooling scenario as follows:

$$T = T_i - r.t \tag{4.9}$$

By combining the effective time from Equation 4.8 and the stress relaxation modulus of the HMA, the internal stress can be calculated at any time after the cooling starts. However, the HMA stress relaxation modulus is not known at this point and it should be derived from the creep compliance equation. It should be noted that the inverse of the creep compliance modulus only gives the creep stiffness of the material which is

very different from the relaxation modulus. Formally, the stress relaxation modulus and creep compliance can be related through their Laplace transforms and the following equation:

$$\bar{C}_{crp}(s)\bar{E}_{rel}(s) = \frac{1}{s^2} \tag{4.10}$$

where $\bar{C}_{crp}(s)$ and $\bar{E}_{rel}(s)$ are Laplace transforms of the creep compliance and stress relaxation modulus, respectively. The Laplace transforms of a known function is mathematically determined as follows:

$$\mathcal{L}F(s) = \overline{F}(s) = \int_0^\infty e^{-st}F(t)dt \tag{4.11}$$

where s is the transform variable. Essentially, the Laplace transformation reduces differential equations to algebraic ones, and thus it is very convenient tool in many viscoelastic problems. For the power law function (Equation 4.3) as it is fitted to the creep compliance data, the Laplace transform would be (Spiegel 1992):

$$\bar{C}_{crp}(s) = \frac{D_0}{s} + D_1 \frac{\Gamma(m+1)}{s^{m+1}} \tag{4.12}$$

where,

D_0, D_1, m = constants in the power law model

When $n > 0$, the gamma function is defined by:

$$\Gamma(n) = \int_0^\infty u^{n-1}e^{-u}\,du \tag{4.13}$$

From Equations 4.10 and 4.12, the Laplace transform of the stress relaxation modulus can be found as:

$$\bar{E}_{rel}(s) = \frac{1}{sD_0 + D_1\Gamma(m+1)t^{(1-m)}} \tag{4.14}$$

To obtain the stress relaxation function, the inverse Laplace transformation must be performed on the Equation 4.14. However, a closed form solution is not available for this function. An approximate method was developed by Christensen (1986) based on theory which produces satisfactory results when the function changes slowly with respect to its primary variable. Based upon this method, the stress relaxation modulus is determined as follows:

$$E_{rel}(t) \cong \frac{1}{D_0 + D_1\Gamma(m+1)(1.73t)^m} \tag{4.15}$$

Christensen (1998) evaluated this method for typical HMA creep compliance values and concluded that it could over-estimate the actual value by five to ten percent, and generate more conservative results.

When a pavement temperature drops, the asphalt layer contracts and the magnitude of the thermally-induced stresses are governed by the tensile strains which result from material contraction. For the asphalt layer, by assuming a linear contraction coefficient, the thermal strain is determined by:

$$\epsilon_T = \alpha.\Delta T \tag{4.16}$$

where,

ϵ_T = thermal strain

α = coefficient of thermal contraction

Once the stress relaxation modulus function of a linear viscoelastic material is known, the stress at time t can be obtained by the Boltzman superposition integral:

$$\sigma(t') = E_{rel}(t')\epsilon_0 = \int_0^{t'} E_{rel}(t'-\xi)\frac{d\epsilon(\xi)}{d\xi}\,d\xi \tag{4.17}$$

By inserting Equation 4.16 into Equation 4.17, the one-dimensional stress function for the pavement surface is defined by:

$$\sigma(t') = E_{rel}(t')\epsilon_0 = \int_0^{t'} E_{rel}(t' - \xi)\,\alpha\frac{dT}{d\xi}\,d\xi \tag{4.18}$$

To solve the integral in Equation 4.8, the slice method (Charpa and Canale 2009) was utilized. This method solves the constitutive equation through a stepwise numerical approach as follows:

$$\sigma(T_n) = \alpha\,\Delta T \sum_{j=1}^{n} E_{rel}[t'(T_i + n\Delta T) - t'(T_1 + j\Delta T - \Delta T/2)] \tag{4.19}$$

This method is advantageous over the trapezoidal method since it does not involve calculation of the stress relaxation modulus at time zero. Mathematically, $E_{rel}(0)$ is a very large number and including it in the model results in over-estimation of the thermal stresses.

4.2 Creep Compliance Testing of the Mixtures

The indirect tensile mode was utilized in this study to measure the creep compliance of the HMA samples at low temperatures. In this test, a compressive load is applied along the diametric line of a disk-shaped specimen of HMA. As the compressive load remains constant, the horizontal and vertical deformations are measured using four extensometers which are mounted at the center of the specimen, both on the front and back. The creep compliance of the HMA sample is then calculated by analyzing the deformation data. Using the indirect tension mode eliminates the need for loading grips or gluing the sample to the test fixture as needed in a direct tension creep test. Figure 4.1 illustrates a prepared IDT creep specimen with the extensometers installed on its both faces.
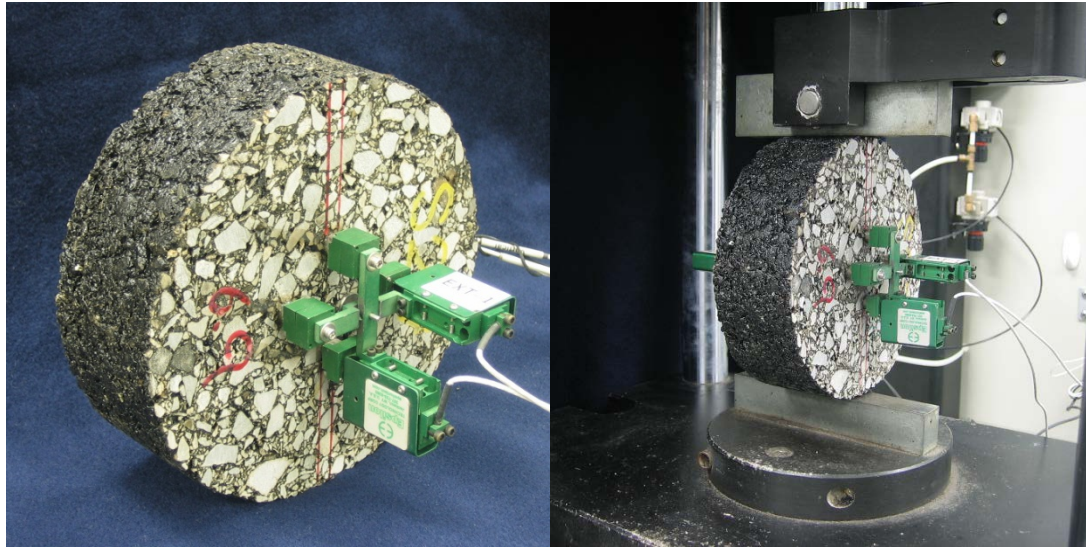
Figure 4.1. a) Prepared IDT Creep Compliance Specimen, b) IDT Creep Specimen in the Testing Device

4.2.1 Materials and Specimen Preparation

Five plant-produced HMA mixtures were tested for creep compliance at low temperatures. Two of these mixtures were previously used in the initial test development experiments. Table 4.1 presents the design properties of the mixtures as well as their job mix formulae (JMF). All mixtures properties reported in Table 1 are from the as-built information provided by Kentucky Transportation Cabinet (KYTC) except for the binder contents. The binder contents of the samples were checked through chemical extraction of asphalt in the laboratory. Since these vary significantly from the as-built information, the extracted binder data were reported. Additionally, the aggregate gradations were determined through sieve analysis and cross-checked with the design JMF.

As recommended in the test procedure, the HMA samples were subjected to loose mix aging prior to testing. This process would simulate the aged condition of the mixtures (7-10 years aging in the field), when they are more susceptible to cracking. After aging, the creep compliance samples were compacted and fabricated according to the same procedure used for IRT disk-shaped samples. All the specimens were compacted to 7.0±0.5 percent air voids, and individually tested for bulk specific gravity to ensure that their air void content is within the acceptable range.

Table 4.1. Mixture Properties (road projects in various Kentucky counties)

Mixture Property	KY55 Adair	KY85 Ohio	KY98 Allen	US42 Oldham	US60 Meade
Design ESAL	4,282,478	718,793	908,092	8,242,663	4,635,119
Binder	PG 76-22	PG 76-22	PG 64-22	PG 76-22	PG 64-22
G_{mm}	2.489	2.445	2.453	2.548	2.465
AC, %	5.2	5.4	4.2	5.4	5.9
Eff. AC, %	4.6	5.1	3.6	4.4	4.9
NMAS, mm	9.5	9.5	9.5	9.5	9.5
VFA, %	84.0	75.7	74.0	74.0	73.0
VMA, %	15.7	16.7	15.8	15.3	15.3
G_{sb}	2.67	2.65	2.63	2.72	2.62
G_{se}	2.715	2.675	2.672	2.797	2.692
G_b	1.03	1.03	1.03	1.03	1.03
Sieve No.	Job Mix Formula, Percent Passing				
1/2 "	100	100	100	100	100
3/8 "	97	94	95	99	97
#4	61	64	68	76	72
#8	35	31	42	41	34
#16	26	18	28	25	22
#30	14	12	20	18	17
#50	10	9	12	13	9
#100	7	7	5	10	5
#200	5.5	5.4	3.4	6.5	4.5

4.2.2 Creep Compliance Test Data

The IDT creep compliance tests were conducted in accordance with the AASHTO T 322 (2007) standard method. Although the standard method indicates that a 100-sec loading time is sufficient for the creep test, the samples in this study were tested for 300 seconds. This extra time provides more creep data and results in more accurate master curves. KY55, KY85, KY98, and US42 mixtures were tested at 0, -10, -20, and -30°C. US60 mix was tested at -10, -20, and -30°C only due to the limitations in the collected sample size. Each test was conducted on triplicate specimens and a total number of 57 specimens were tested. The test data were analyzed as per the method describe in the AASHTO T 322 (2007) standard and creep compliance information were obtained. The isothermal creep compliance data are shown in Appendix A for various temperatures.

The isothermal creep compliance data were then shifted to the reference temperature of -30°C to build the creep master curves. The power law function in Equation 4.3 was fitted to the shifted master curve data. Moreover, the Equation 4.4 was fitted to the shift factor values for each master curve to develop the Arrhenius type shift factor functions. Figure 4.2 depicts the shifted creep compliance data as well as the fitted master curves. The final coefficients of the master curves are presented in Table 4.2 along with the coefficients of the shift factor functions.
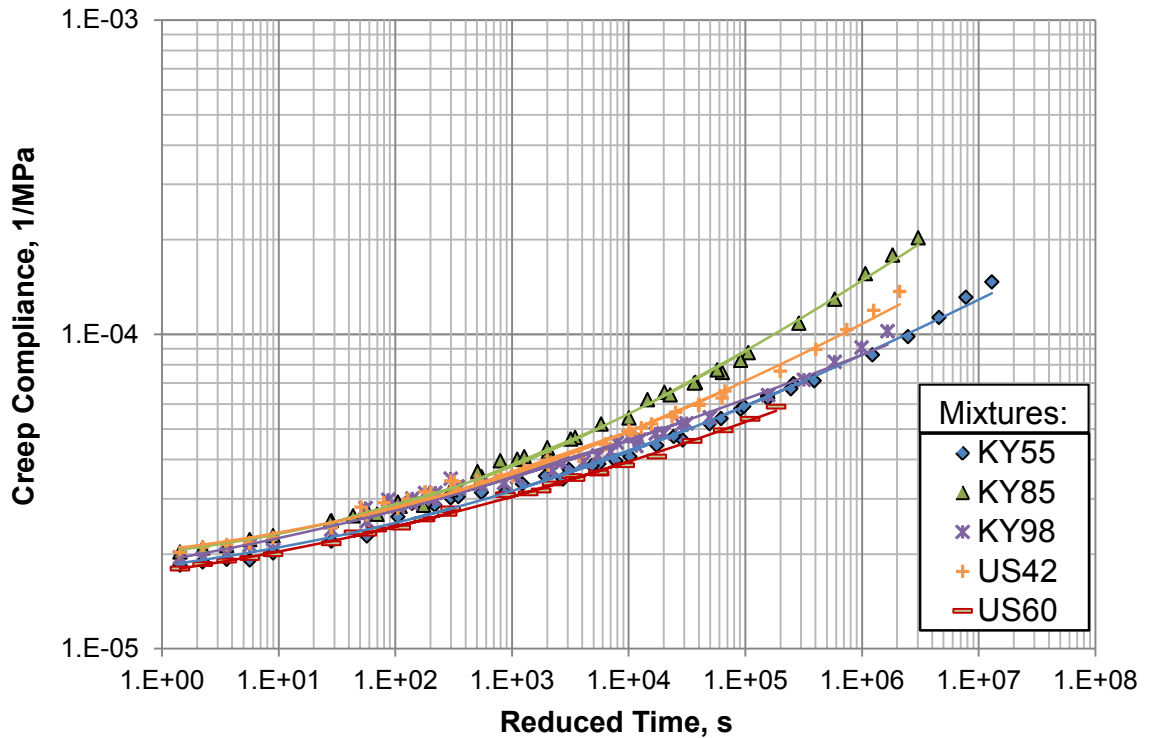
Figure 4.2. Creep Compliance Master Curves at -30°C

Table 4.2. Master Curve and Shift Factor Function Coefficients

Mix	Arrhenius Function		Power Function–Master Curve		
	a0	a1	D0	D1	m
KY55	-0.1018	9881.4	1.40397E-05	4.35591E-06	0.20303
KY85	0.0786	8809.3	1.68729E-05	3.43217E-06	0.263841
KY98	-0.0439	7705.1	1.18253E-05	7.22655E-06	0.168673
US42	-0.0392	8196.5	1.64871E-05	4.12888E-06	0.224255
US60	-0.0138	8928.2	1.20025E-05	5.63063E-06	0.171664

4.3 Analysis of Critical Crack Sizes

4.3.1 Thermal Stress Calculations

The stress relaxation function of each HMA mix was determined by combining its creep compliance master curve function and Equation 4.15. To estimate the thermal stresses induced in the pavements by temperature drop, a hypothetical cooling scenario was assumed that would conform to the environmental conditions of central Kentucky. This scenario assumes that the tensile stress is zero in the pavements at 5°C. Then the pavement temperature starts to drop at the rate of 2°C/hour. These numbers were used as the coefficients in Equation 4.9. Additionally, a linear thermal contraction coefficient of 0.00002 /°C was assumed for all of the pavements.

By knowing the stress relaxation functions, the thermally-induced stresses were then calculated through Equation 4.19 at 1°C temperature intervals ($\Delta T = 1$°C). At every step, the effective time (t') was determined by solving the integral in Equation 4.8 using the trapezoidal rule (Charpa and Canale 2009). The thermal stress calculations and its associated integrations were executed in a Microsoft® Excel® spreadsheet. The resulting thermal stresses are presented in Figure 4.3.

4.3.2 Analysis of Allowable Crack Size

Knowing thermal stresses in a pavement enables determination of the stress intensity factor in the vicinity of existing cracks and flaws in the HMA layer. Since thermal cracking of asphalt pavements typically occurs at temperatures where asphalt has already entered into its quasi-brittle and mostly linear zone, the linear fracture mechanics assumptions can be applied for the calculations of stress intensity factor. If the crack size in a pavement is known, comparing the stress intensity factor in the field to the K_{IC}, which can be obtained from the IRT fracture test, would yield the temperature at which the crack would start growing. On the other hand, if the temperature is known, the comparison between the stress intensity factor and K_{IC} would determine the maximum allowable crack size (MACS).
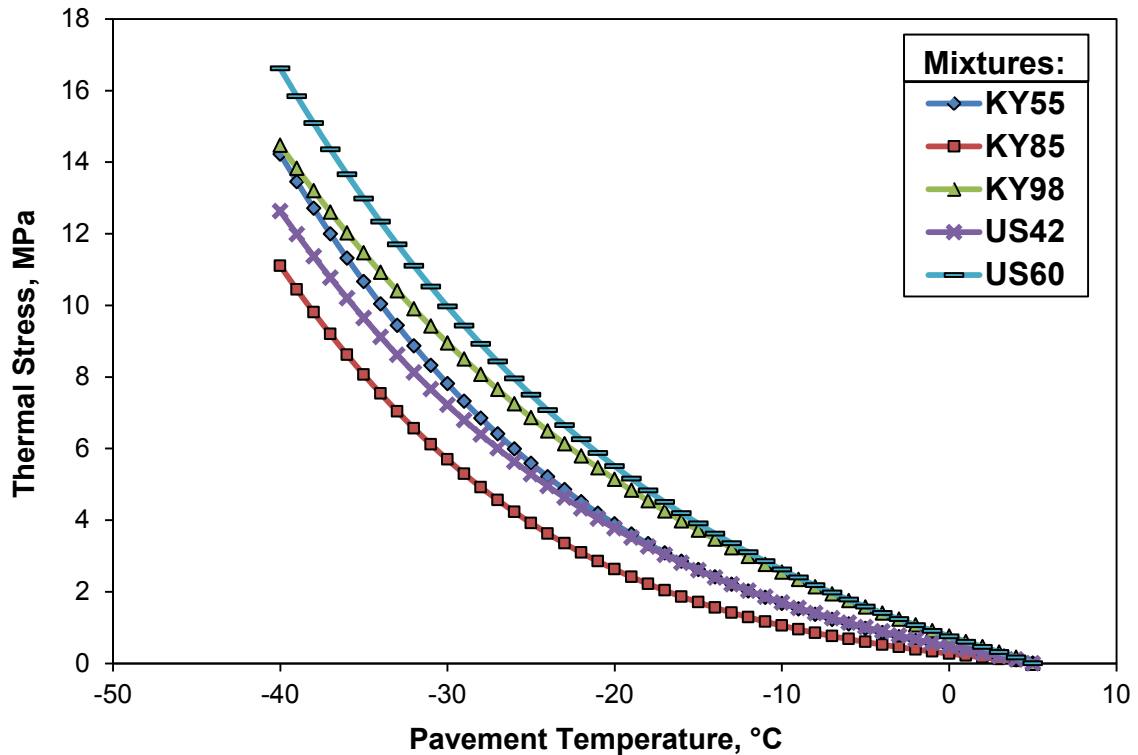
Figure 4.3. Thermal Stresses as Calculated by the Viscoelastic Model
Note: initial temperature = 5°C, cooling rate = -2°C/hr, temperature increment = 1°C, linear
contraction coefficient= 0.00002 /°C

A set of IRT fracture tests were executed on the HMA mixtures in this part of the study to measure the fracture properties of the mixtures at low temperatures. All five mixtures were made with PG xx-22 binders; therefore, the IRT tests were conducted at -22°C to ensure that mixes are in the quasi-brittle phase. The loose-mix samples were conditioned for 24 hours at 135°C to simulate the long-term aged conditions of the pavements. IRT test specimens were produced at 7.0±0.5 percent air voids content, which is typical for mechanical testing of HMA. Table 4.3 contains the average fracture toughness and normalized fracture toughness of the mixtures along with their coefficient of variation based upon three replicate samples.

Several formulae have been developed for calculating the stress intensity factor in plates with various forms of flaws and crack locations (Hertzberg 1996; Anderson 1995). For instance, in an infinitely large body subjected to pure tension in the direction normal to the crack face, the stress intensity factor can be determined by:

$$K_I = \sigma\sqrt{\pi a} \tag{4.20}$$

where σ is the tensile stress and a is the one-half crack length. According to the linear fracture mechanics theory, an existing crack in an infinitely large and thick plate (plane-strain condition) starts growing when K_I from Equation 4.20 reaches the critical value of plane-strain fracture toughness (K_{IC}) of the material.

Table 4.3. Average IRT Fracture Test Results at -22°C

Mix	K_{IC}, MPa√mm	COV	Fracture Energy, J/m	COV
KY55	30.18	3.5%	2346	9.4%
KY85	28.63	2.9%	2315	2.9%
KY98	26.30	3.2%	1996	5.3%
US42	28.40	4.3%	2357	3.6%
US60	27.13	2.6%	1975	3.0%

Note: Specimens were compacted to 7.0±0.5 percent air voids after 24 hours of loose mix aging at 135°C

The geometric conditions of Equation 4.20 are similar to those in an asphalt pavement with a transverse crack, which is far from the pavement edge. By substituting the K_{IC} values obtained from the IRT fracture testing of the five HMA mixtures (Table 4.3) and thermally induced stresses based upon the hypothetical cooling scenario which was described earlier (Figure 4.3), the maximum allowable crack sizes in the asphalt surface were estimated as depicted in Figure 4.4. This figure demonstrates how the existing transverse cracks and flaws in the pavements would react to the temperature cooling. For example, as the pavement's surface temperature drops to -12°C at the assumed rate, the transverse cracks with an approximate length of 49 mm or longer would start growing on the US60 pavement. For similar cooling conditions, KY85 mixture is estimated to exhibit a better performance and cracks shorter than 315 mm would not start growing (Figure 4.4). Generally, the MACS parameter has an inverse relationship to the cracking potential of the pavement, and the mixtures with higher

MACS would be expected to show a better performance at low temperatures. It should be noted that this analysis was only performed to estimate the cracking potential of a single thermal event. Other factors, such as cyclic thermal loading, crack initiation, and crack healing could also contribute to the overall low-temperature cracking performance.

The cracking susceptibility analysis indicates that the maximum allowable crack size in an asphalt pavement is highly sensitive to the HMA fracture toughness. Additionally, as the temperature drops to below freezing point, the pavement susceptibility to thermal cracking grows rapidly. In other word, this analysis shows that small changes in the HMA fracture toughness could translate into significant changes in terms of the asphalt pavement thermal cracking performance.
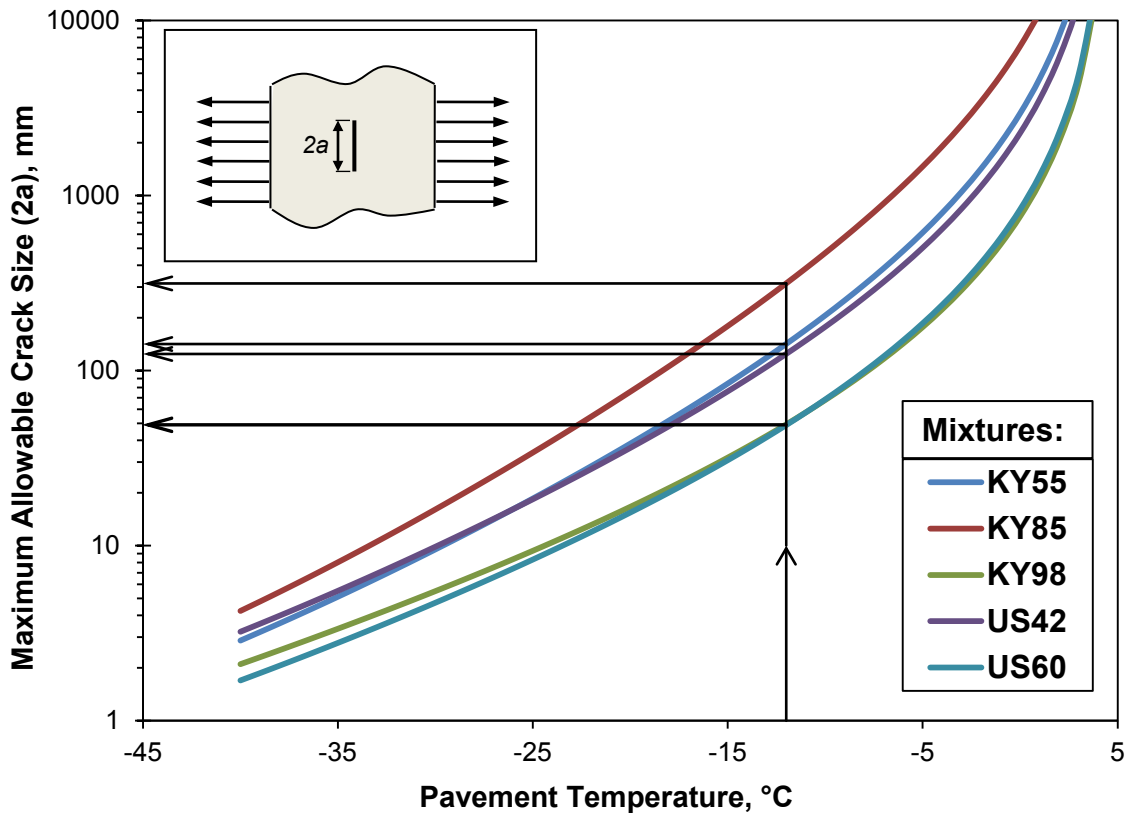
Figure 4.4. Maximum Allowable Transverse Crack Size in Asphalt Pavements

Table 4.4 presents the maximum allowable crack size (MACS) values for the mixtures at various temperatures. This data implies that although all the HMA mixtures were made with PG xx-22 asphalt binders, they could show very different performances

with respect to low-temperature cracking. In fact, the test information derived from asphalt binder testing indicated that the mixtures would have similar performance at low temperatures; however, the HMA mixtures showed very different susceptibility to thermal cracking.

Table 4.4. Maximum Allowable Crack Sizes at Various Temperatures

Temperature	Maximum Allowable Crack Size, mm				
	KY55	KY85	KY98	US42	US60
-7°C	384	902	117	321	121
-12°C	142	315	49	125	49
-17°C	61	126	24	56	23
-22°C	28	55	13	27	12
-27°C	14	25	8	14	7

4.3.3 Comparison to the Tensile Strength Analysis

In the traditional methods of analyzing the low-temperature cracking of asphalt pavements, often the tensile strength of the HMA sample as manufactured in the laboratory is employed as the failure criterion. In essence, these traditional analyses represent the rupture of the HMA material without any cracks or flaws under tensile load. This rupture failure was not considered in the maximum allowable crack analysis as presented in Figure 4.4. However, if a body of material reaches its rupture strength before its critical stress intensity factor, the rupture-type failure will precede the crack-propagation-type failure.

In this part of the study, a comparison was made between the crack propagation analysis and the tensile strength analysis to see if the traditional method can sufficiently represent the cracking potential in asphalt pavements. Tensile strength of HMA is typically measured in an asphalt laboratory by the means of the indirect tension (IDT) test on disk-shaped samples. In this test, a compressive load is applied along the diametric line of a disk-shaped specimen of HMA. The load increases at 12.5 mm/min rate, and consequently, the tensile stress increases on the loading line. The load increase continues until the specimen fails and splits into two pieces. The IDT strength test was conducted on the five mixtures shown in Table 4.1 at -10°C, and according to the AASHTO T 322

82

(2007) standard method. As presented in Table 4.5, three specimens were tested for each mix and the average was used as the tensile strength of the HMA mixtures.

The tensile strength values were used in conjunction with the thermal stress data, which were calculated through the viscoelastic model, to determine the critical rupture temperature (T_C) of the mixtures. This was basically accomplished by inserting the tensile strength values into the vertical axis of the plot in Figure 4.3 and finding the corresponding temperature for the tensile strength. The calculations were made by fitting a third degree polynomial function to the thermal stress curve of the mixtures with coefficient of determination (R^2) values higher than 0.9999. The resulting critical rupture temperatures are shown in Table 4.5.

Table 4.5. IDT Tensile Strength Results and Critical Rupture Temperatures

Mix	Rupture Load	Tensile Strength	Avg. Tensile Strength	COV	$T_C{}^*$, °C	$2a_C{}^{**}$, mm
KY55	52326	4.44	4.44	2.3%	-21.8	29
	51168	4.34				
	53592	4.55				
KY85	50508	4.29	3.91	12.2%	-25.0	34
	39746	3.37				
	47880	4.06				
KY98	44910	3.81	3.82	3.7%	-15.4	30
	43374	3.68				
	46662	3.96				
US42	52362	4.44	4.58	2.8%	-22.8	25
	55345	4.70				
	54233	4.60				
US60	51316	4.36	4.33	2.6%	-16.5	25
	52077	4.42				
	49475	4.20				

* Critical rupture temperature from tensile strength
** Minimum crack size that propagate before tensile rupture

By assuming the hypothetical cooling scenario, which was described earlier, and conducting the maximum allowable crack size (MACS) analyses, a critical crack size was found for every pavement temperature as demonstrated in Figure 4.4. This data can also be used to determine the corresponding MACS value to the critical rupture temperature

(T_C), which was obtained from the tensile strength analysis. This MACS value, which is denoted by $2a_C$, represents the lower boundary for the size of the cracks which would start growing before the tensile stress in the pavement reaches its critical rupture strength.

The $2a_C$ value of the mixtures was determined by fitting polynomial functions to the thermal stress and MACS curves. As presented in Table 4.5, $2a_C$ varied between 25 and 34 mm for the pavements in the study. Figure 4.5 schematically demonstrates the physical concept of $2a_C$.
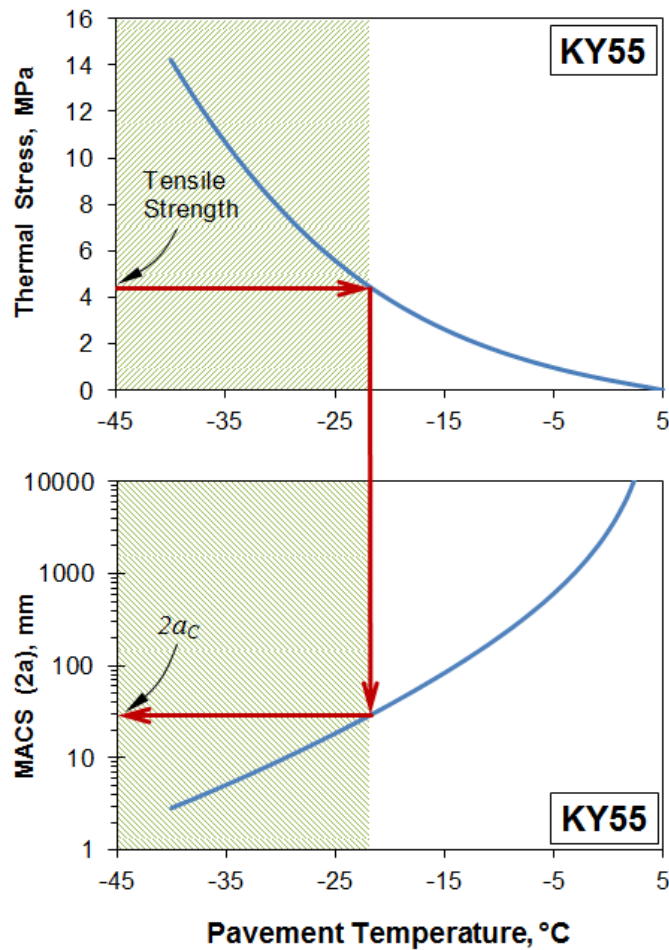
Figure 4.5. Determination of $2a_C$

As the temperature drops, the stress in the KY55 pavement would presumably reach its critical rupture value at T_C= -21.8℃, and the temperature plot would not enter the hatched zones in Figure 4.5. In essence, $2a_C$ represents the maximum size of the

cracks that are considered in the traditional tensile strength analysis. In other words, by using the tensile rupture strength as the failure criterion, the effect of any cracks larger than 29-mm was neglected. Therefore, by designing the pavement of KY55 for any MACS larger than 20-mm, the tensile strength method produces a less conservative design and imposes higher risk of thermal cracking. The $2a_C$ values for the other pavements are presented in Table 4.5. All the pavements showed relatively small $2a_C$ values. Considering the current practices of design and construction of asphalt pavements, much larger cracks may form in the pavements, particularly when they age and undergo a high number of traffic loads.

CHAPTER 5
EFFECT OF DENSITY ON THERMAL CRACKING

The in-place density of the hot-mix asphalt (HMA) is one of the most important factors that would influence the performance of an asphalt pavement (Asphalt Institute 2007). The desired level of construction density in HMA layers in the field is achieved by the means of roller compaction. The aggregate particles in an HMA layer tend to interlock as the result of the compaction process and ideally would form a stone-on-stone type of structure. An asphalt layer after compaction is a denser layer with lower air voids, and a smooth and uniform surface.

The achieved in-place density of an asphalt pavement results from a combination of different activities involved in proper design, production, placement, compaction, and quality control of the mixture (Asphalt Institute 2007). The density of an asphalt mixture is normally expressed as a percent of its theoretical maximum specific gravity (G_{mm}). An HMA mixture behind a paver typically has a density of 75 to 85 percent of its G_{mm}. The goal of compaction is often to increase the in-place density to a target level of 92 to 93 percent of G_{mm}, which translates to 7 to 8 percent air voids, for typical pavements.

Some research studies have been conducted to evaluate the effect of density on rutting and fatigue performance of HMA (Akhtarhusein et al. 1994; Harvey and Tsai 1996; Kim et al. 2008). However, the effect of density on low-temperature fracture properties of HMA has not been investigated thoroughly. In general, density has a high impact on the performance of HMA material, and it is has been used as the primary quality control factor for asphalt pavement construction for many years.

The Kentucky Transportation Cabinet (KYTC) launched a research project in 2007 to better understand the effect of density on durability of asphalt pavements. The first phase of this study involved conducting a series of performance tests to see if increasing the initial in-place density from 92 to 93 percent of G_{mm} would cause a significant improvement in the asphalt pavements performance (Blankenship and Anderson 2010). The results showed that for a 1.5 percent increase in the initial density, the fatigue life of the tested specimens increased by up to 10 percent. Furthermore, the flow number increased by 34 percent for a similar increase in the mixture's density.

For the second phase of the KYTC density project, HMA samples were collected from five pavement construction projects in central Kentucky. The in-situ measurements on the pavements after construction revealed that the actual densities of the pavements were considerably lower than the desired 92 percent of G_{mm}. Although the measured in-place densities were lower than their target values, the results were not outside of the KYTC's expectations based on the requirements (rolling pattern only) for lower traffic pavements placed at a 25-mm lift thickness. It should be noted that if these were higher-type facilities, the lower densities would have been addressed by the KYTC.

The KYTC density project provided a unique opportunity to utilize the indirect ring tension (IRT) fracture test and evaluate the effect of in-place density on low-temperature fracture properties of the field mixtures. Furthermore, the IRT fracture data could be compared to the DC(t) test, which is another fracture test geometry for HMA material.

5.1 Material and Testing Plan

5.1.1 In-Place Densities

The mix samples were collected from several sections of five non-primary pavements with traffics lower than 10 million equivalent single axle loads (ESALs). Design properties of the mixtures are presented in Table 4.1. At each sampling location, the in-place density profile of the pavement was determined using a non-nuclear density gauge. The density was measured at the centerline, as well as at 15, 45, and 152 cm distances on each side of the centerline for a total of seven measurements. It should be noted that the in-place density readings were taken before any traffic was allowed on the new pavements. Moreover, all of the highway projects were 25-mm (1-in) lift resurfacing projects with little or no milling.

Results from the field measurements indicated that the density of the middle portion of the pavement was consistently lower than the density of the pavement farther from the centerline. For each section, the trimmed average density was calculated by omitting the highest and lowest measured densities as outliers. Then, for each individual

project, the average in-place density was determined by taking the average density of the sampling sections (Table 5.1).

Table 5.1. In-Place Density of the Pavements

Property	KY55 Adair	KY85 Ohio	KY98 Allen	US42 Oldham	US60 Meade
Avg. In-Place Air Voids (%)	11.5	10.7	13.2	11.6	12.9
Avg. In-Place Density (%)	88.5	89.3	86.8	88.4	87.1

5.1.2 Experimental Plan

An experimental laboratory plan was developed to evaluate the potential low-temperature performance of the HMA mixtures at various densities. The IRT fracture test specimens were produced and tested at four density levels for each mixture:

- 4 percent air voids, which represents the standard for the laboratory compaction.
- 7 percent air voids, which is the typical value for laboratory mechanical testing.
- 8 percent air voids, the desirable level after compaction in the field.
- Average in-place density of each pavement as measured in the field (Table 5.1).

This experimental plan was basically developed to determine whether or not the deficiencies in the in-place density would affect the performance of the pavements at low temperatures. Additionally, testing at various density levels would help quantify the effect of changes in the air voids content on thermal cracking potential of the HMA mixtures.

5.1.3 Specimen Preparation and Testing

Three IRT replicate specimens were produced per each density level for each HMA mix. The desired density levels were achieved in the lab by adjusting the weight of the loose-mix samples that were placed in each gyratory compactor mold. All the IRT specimens were fabricated with the geometry parameters that were recommended in Chapter 3, with

$R= 75$ mm, $r= 13$ mm, and 9 mm$< a < 11$ mm. Prior to compaction, the loose-mix samples were conditioned for 24 hours in a forced-draft oven at 135°C to simulate the long-term aging.

All the specimens were individually tested for bulk specific gravity. An air void content tolerance of ±0.5% was employed for all the samples, and those outside of the acceptable range were discarded. The preliminary measurements showed that the water could become trapped in the specimens with 10.7 to 13.2 percent air voids, and the specimens were not completely dry even after several days of storage at room temperature. This water entrapment range is also seen in pavements where water becomes trapped.

To overcome this problem, a CoreDry® device (Figure 3.4) was used to make sure that all the water in the specimens from trimming was removed. The CoreLok® bulking procedure (vacuum sealed bag) was used to achieve a consistent and accurate method for determining the air voids of all the specimens. After sample preparation and temperature conditioning, the IRT fracture tests were conducted at -22°C, which is the temperature that represents the lower PG grade of the asphalt binders in the study.

5.2 IRT Fracture Test Results

5.2.1 Fracture Toughness

The IRT fracture tests were conducted in accordance with the procedures recommended in Chapter 3. The raw test data for this group of specimens is presented in Appendix B. After testing the samples and measuring their initial notch length, the Equation 3.1 was employed to determine the plane-strain fracture toughness (K_{IC}) of the mixtures. The calculated K_{IC} values are presented in Tables 5.2 to 5.6 for the five mixtures in the study. As seen in these tables, the IRT fracture test produced consistent K_{IC} values for the HMA mixtures with a relatively high repeatability. The coefficient of variation for the obtained K_{IC} values from this set of specimens ranged from 1.8 to 6.2 percent.

In general, the specimens which were fabricated at the in-place air voids content (10.7 to 13.2 percent) demonstrated slightly less repeatable results. Furthermore, the specimens with high air voids showed more diverse failure patterns toward the end of the

test. This was not unexpected, since the higher air voids in such specimens would tend to cause more non-homogeneity which can result in more scattered test data.

Table 5.2. Fracture Toughness of KY55 Mix at -22°C and Various Densities

Target Air voids (%)	Sample	Air Voids (%)	Crack Length, (mm)	Max Load (N)	K_{IC} (MPa√mm)	Average $K_{IC,}$ (MPa√mm)	COV (%)
	KY55-1	4.2	10.64	29395	32.47		
4.0	KY55-2	3.5	9.49	29961	33.69	33.13	1.9%
	KY55-3	3.9	10.12	29835	33.21		
	KY55-4	6.8	9.41	27667	31.16		
7.0	KY55-5	6.8	10.13	27226	30.30	30.18	3.5%
	KY55-6	6.9	11.12	26492	29.08		
	KY55-26	8.4	10.28	23515	26.11		
8.0	KY55-27	8.5	10.19	23932	25.61	26.09	2.0%
	KY55-28	8.2	11.04	23247	25.55		
	KY55-7	11	9.56	20635	23.18		
11.5	KY55-8	12	11.21	19348	21.22	22.10	4.5%
	KY55-9	11.6	10.03	19639	21.89		

Note: test temperature= -22°C

Table 5.3. Fracture Toughness of KY85 Mix at -22°C and Various Densities

Target Air voids (%)	Sample	Air Voids (%)	Crack Length, (mm)	Max Load (N)	K_{IC} (MPa√mm)	Average $K_{IC,}$ (MPa√mm)	COV (%)
	KY85-1	4.0	11.23	26203	28.73		
4.0	KY85-2	3.5	10.69	27888	30.79	30.03	3.8%
	KY85-3	3.7	10.76	27710	30.56		
	KY85-4	7.0	10.30	26227	29.12		
7.0	KY85-5	6.9	10.97	25141	27.65	28.63	2.9%
	KY85-6	6.9	10.02	26111	29.11		
	KY85-21	8.5	10.52	23651	26.17		
8.0	KY85-22	7.6	10.65	23321	25.76	26.11	1.2%
	KY85-23	8.2	10.30	23766	26.38		
	KY85-7	10.9	10.40	18990	21.05		
10.7	KY85-8	10.7	12.17	19066	20.69	21.64	6.2%
	KY85-9	10.3	10.72	20990	23.16		

Note: test temperature= -22°C

Table 5.4. Fracture Toughness of KY98 Mix at -22°C and Various Densities

Target Air voids (%)	Sample	Air Voids (%)	Crack Length, (mm)	Max Load (N)	K_{IC} (MPa√mm)	Average $K_{IC,}$ (MPa√mm)	COV (%)
	KY98-1	4.4	9.37	28266	31.85		
4.0	KY98-2	4.2	9.47	26395	29.69	30.60	3.7%
	KY98-3	3.6	10.18	27211	30.26		
	KY98-4	7.0	10.10	22774	25.36		
7.0	KY98-5	6.9	10.04	23823	26.55	26.30	3.2%
	KY98-6	7.0	9.59	24025	26.97		
	KY98-23	8.5	8.77	22059	25.13		
8.0	KY98-24	7.9	8.85	21493	24.45	24.62	1.8%
	KY98-25	8.0	9.00	21403	24.28		
	KY98-7	12.6	9.90	15021	16.78		
13.2	KY98-8	13.0	9.98	16070	17.93	17.77	5.2%
	KY98-9	13.1	9.58	16570	18.61		

Note: test temperature= -22°C

Table 5.5. Fracture Toughness of US42 Mix at -22°C and Various Densities

| Target Air voids (%)	Sample	Air Voids (%)	Crack Length, (mm)	Max Load (N)	K_{IC} (MPa√mm)	Average $K_{IC,}$ (MPa√mm)	COV (%)
	US42-1	4.5	10.15	27125	30.18		
4.0	US42-2	3.9	9.68	28505	31.96	31.20	2.9%
	US42-3	3.9	10.37	28368	31.46		
	US42-4	7.2	10.34	26852	29.79		
7.0	US42-5	7.2	10.24	25177	27.98	28.40	4.3%
	US42-6	6.8	11.96	25227	27.43		
	US42-11	8.1	10.32	25965	28.82		
8.0	US42-12	8.2	10.94	24866	27.36	27.40	5.1%
	US42-26	8.1	10.24	23416	26.02		
	US42-7	12	10.83	19407	21.38		
11.6	US42-8	11.6	9.74	21096	23.63	22.73	5.2%
	US42-9	11.7	9.85	20721	23.16		

Note: test temperature= -22°C

Table 5.6. Fracture Toughness of US60 Mix at -22°C and Various Densities

Target Air voids (%)	Sample	Air Voids (%)	Crack Length, (mm)	Max Load (N)	K_{IC} (MPa√mm)	Average $K_{IC,}$ (MPa√mm)	COV (%)
	US60-1	3.8	10.13	27077	30.14		
4.0	US60-2	3.7	10.59	27697	30.62	30.81	2.6%
	US60-3	3.6	9.96	28384	31.68		
	US60-4	7.0	9.49	23587	26.53		
7.0	US60-5	7.1	9.53	23985	26.96	27.13	2.6%
	US60-6	6.8	9.64	24873	27.90		
	US60-31	8.1	11.70	22880	24.95		
8.0	US60-32	7.7	10.80	21235	23.41	24.38	3.5%
	US60-33	8.3	10.73	22469	24.79		
	US60-7	12.8	10.20	18176	20.21		
10.7	US60-8	11.6	9.98	19798	22.09	21.01	4.6%
	US60-9	11.7	10.51	18734	20.73		

Note: test temperature= -22°C

Figure 5.1 displays the relationship between the specimens' density and their fracture toughness (K_{IC}) as determined by the IRT fracture test. Statistical linear regression was performed to analyze the effect of air voids content on K_{IC}. The General Linear Model procedure in the SAS/STAT® program was utilized to conduct the analysis. The resulted regression lines are presented in Figure 5.1 along with their coefficient of determination (R^2) values. The regression analysis indicated that the effect of air voids content on specimen K_{IC} was highly significant. All the resulting P-values for the regression lines slope, as presented in Table 5.7, concluded that increasing the air voids content of the specimens significantly lowered the fracture toughness of the specimens. In other words, the IRT test data implied that pavements with higher air voids content could be more susceptible to thermal cracking.

In general, the IRT test seemed to be an effective tool for examining the effect of density on low-temperature properties of the HMA mixtures. The test produced relatively repeatable results and generated adequate information to discern the differences between the cracking potential of various asphalt mixtures.
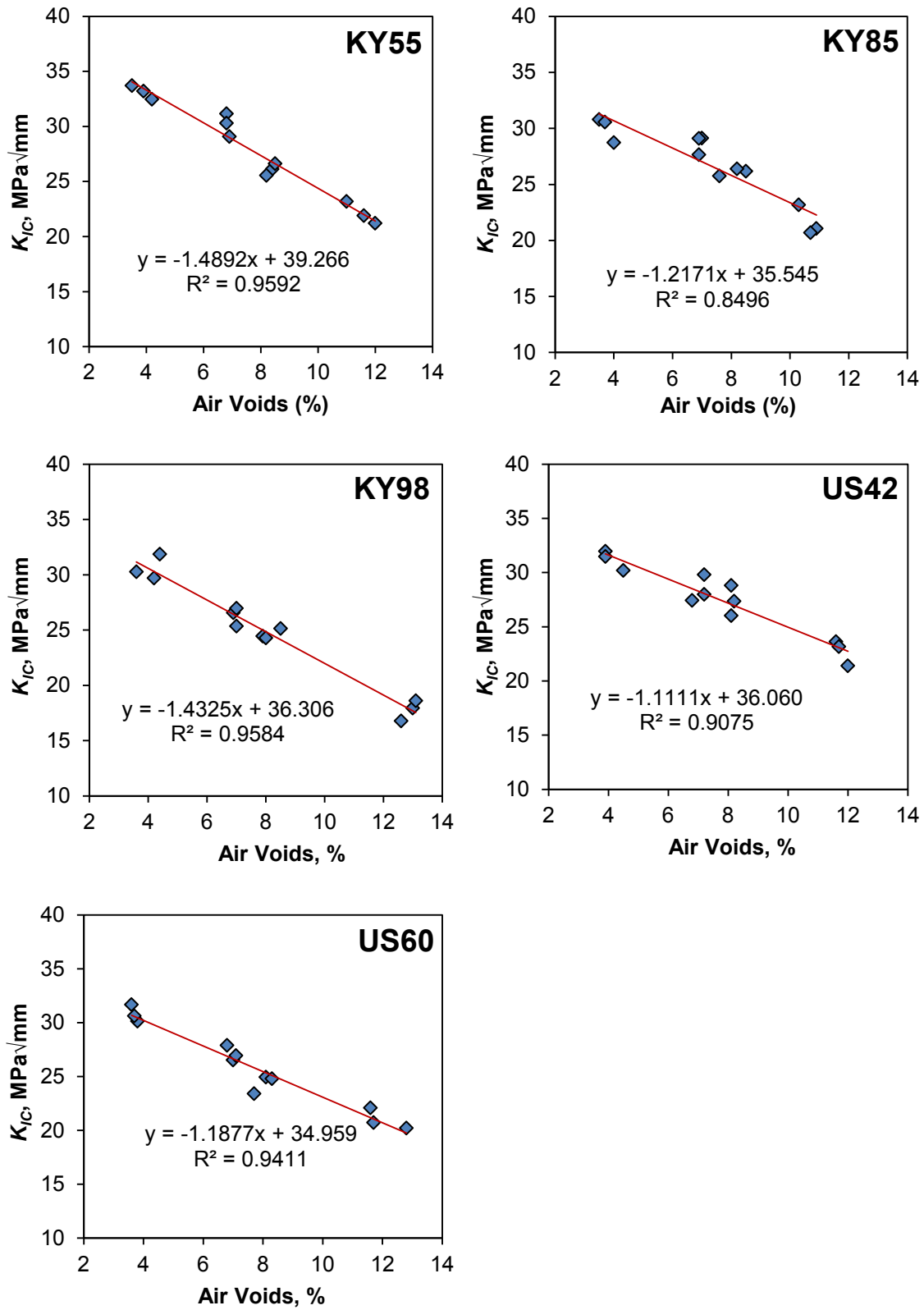
Figure 5.1. Fracture Toughness of the HMA Mixtures at Various Densities
Note: test temperature= -22°C

Table 5.7. Regression Analysis Results on K_{IC} at Various Densities

Mix		DF	Parameter Estimate	Standard Error	t statistic	P-value
KY55	Intercept	1	39.26612	0.79036	49.68	< .0001
	Slope	1	-1.48919	0.09712	-15.33	< .0001
KY85	Intercept	1	35.62844	1.28357	27.75737	< .0001
	Slope	1	-1.20897	0.16539	-7.30996	< .0001
KY98	Intercept	1	36.30573	0.81421	44.59	< .0001
	Slope	1	-1.43254	0.09435	-15.18	< .0001
US42	Intercept	1	36.06041	0.92424	39.02	< .0001
	Slope	1	-1.11105	0.11218	-9.90	< .0001
US60	Intercept	1	34.95850	0.77477	45.12	< .0001
	Slope	1	-1.18767	0.09397	-12.64	< .0001

By calculating the maximum allowable crack size (MACS) for each IRT test data, more information can be procured about the cracking susceptibility of the mixtures and their differences. By employing the creep compliance data and the thermal stresses that were estimated in Chapter 4, the MACS values were calculated individually for each test specimen based upon its facture toughness (Tables 5.2 to 5.6). By assuming the same cooling scenario as described in Chapter 4 (cooling starts at 5°C, and pavement temperatures drops at the rate of 2°C/hr), the MACS values were determined for the pavements with the final temperatures of -12°C. This is the temperature at which mixtures have entered their quasi-brittle phase and have become more susceptible to thermal cracking. The final MACS information was achieved by inputting the K_{IC} data from the IRT test into the curves in Figure 4.4.

Figure 5.2 illustrates the variation of the calculated maximum allowable crack size of the pavements with respect to their in-place air voids content. Calculation of MACS involves consideration of the relaxation properties of the mixtures in addition to their fracture susceptibility. Therefore, by converting the fracture toughness data into MACS, the difference between the mixtures cracking susceptibility became clearer. A comparison between the regression lines in Figure 5.2 would reveal that there is a substantial difference between the cracking susceptibility of the mixtures even though they were all designed to have similar critical cracking temperature of -22°C.
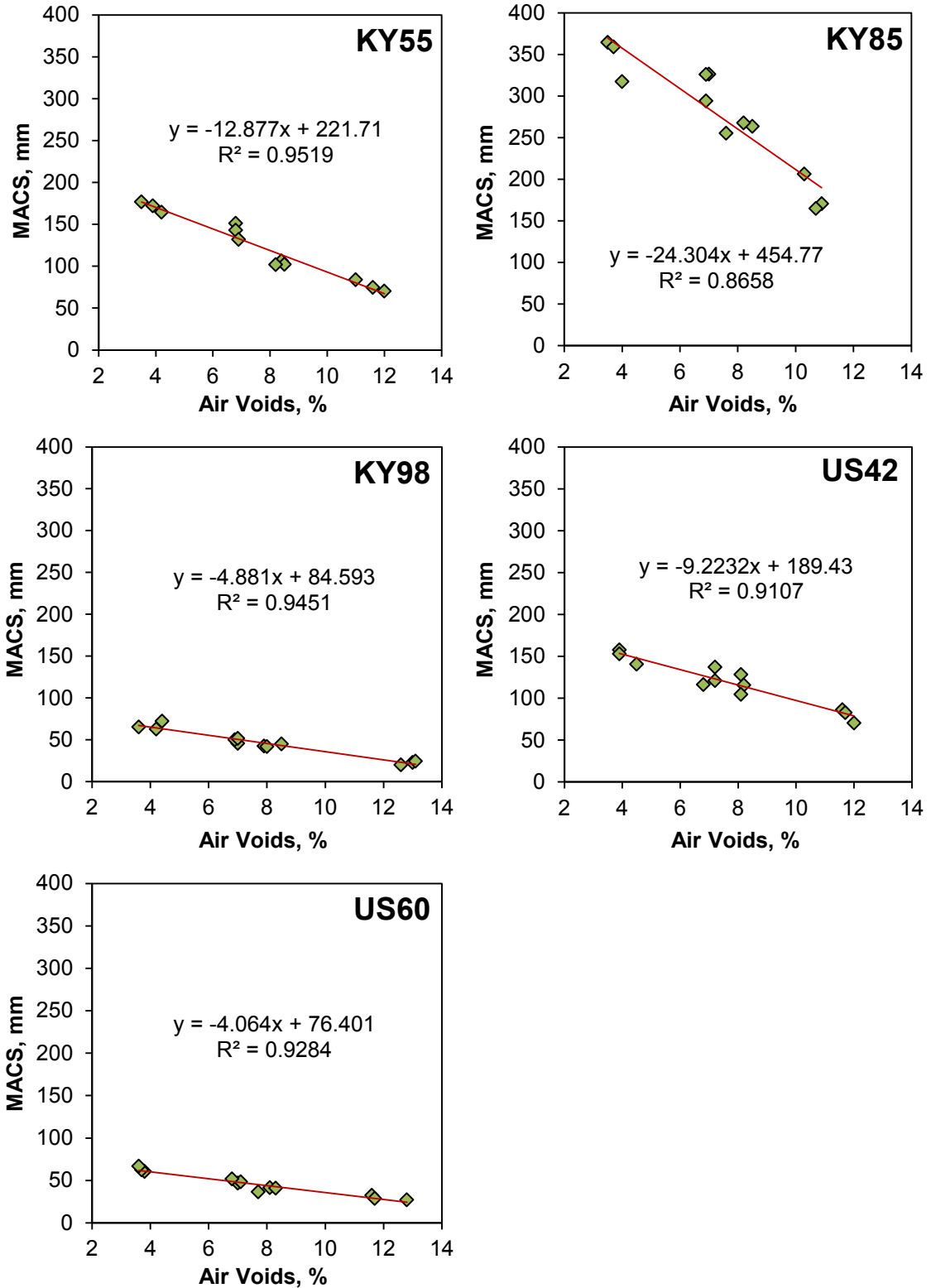
Figure 5.2. Maximum Allowable Crack Size for the HMA Mixtures at -12°C and Various Densities

Note: initial temperature = 5°C, cooling rate = -2°C/hr, contraction coefficient= 0.00002 /°C

In general, the maximum allowable crack size (MACS) parameter is directly related to the cracking potential of HMA at low temperatures, and the mixture with higher MACS value would exhibit a higher resistance to crack propagation. Among the HMA mixtures in this study, as illustrated in Figure 5.2, KY85 mix would be expected to show the highest resistance to crack propagation.

5.2.2 Normalized Fracture Energy

In addition to the fracture toughness of the HMA specimens, their normalized fracture energy was determined by calculating the area under the load-displacement curve and dividing it by the fracture surface area. The load-displacement curves for this set of specimens are shown in Appendix B. The normalized fracture energy data are presented in Tables 5.8 to 5.12 for the five mixtures in the study. The fracture energy as determined by this method is not a fundamental material property, and is based on the total energy consumed by the test device and the cohesive zones that are created by the tensile load. As expected, the fracture energy data were not as repeatable as the fracture toughness data; however, they can still demonstrate the effect of density variation on the cracking potential of the HMA mixtures.

Table 5.8. Normalized Fracture Energy of KY55 Mix from IRT Test

Target Air voids (%)	Sample	Air Voids (%)	Fracture Surface Area (mm^2)	Normalized Fracture Energy (J/m^2)	Average FE (J/m^2)	COV (%)
4.0	KY55-1	4.2	5136	2490	2669	5.9%
	KY55-2	3.5	5251	2788		
	KY55-3	3.9	5188	2730		
7.0	KY55-4	6.8	5259	2549	2346	9.4%
	KY55-5	6.8	5187	2376		
	KY55-6	6.9	5088	2113		
8.0	KY55-26	8.4	5172	1920	2102	8.0%
	KY55-27	8.5	5181	2253		
	KY55-28	8.2	5096	2134		
11.5	KY55-7	11	5244	1645	1592	12.2%
	KY55-8	12	5079	1376		
	KY55-9	11.6	5197	1755		

Note: test temperature= -22°C

Table 5.9. Normalized Fracture Energy of KY85 Mix from IRT Test

Target Air voids (%)	Sample	Air Voids (%)	Fracture Surface Area (mm^2)	Normalized Fracture Energy (J/m^2)	Average FE (J/m^2)	COV (%)
	KY85-1	4.0	5077	2273		
4.0	KY85-2	3.5	5131	2368	2370	4.1%
	KY85-3	3.7	5124	2468		
	KY85-4	7.0	5170	2292		
7.0	KY85-5	6.9	5103	2261	2315	2.9%
	KY85-6	6.9	5198	2391		
	KY85-21	8.5	5148	1829		
8.0	KY85-22	7.6	5135	1738	1909	11.6 %
	KY85-23	8.2	5170	2159		
	KY85-7	10.9	5160	1441		
10.7	KY85-8	10.7	4983	1711	1653	11.5%
	KY85-9	10.3	5128	1807		

Note: test temperature= -22°C

Table 5.10. Normalized Fracture Energy of KY98 Mix from IRT Test

Target Air voids (%)	Sample	Air Voids (%)	Fracture Surface Area (mm^2)	Normalized Fracture Energy (J/m^2)	Average FE (J/m^2)	COV (%)
	KY98-1	4.4	5263	2295		
4.0	KY98-2	4.2	5253	2512	2474	7%
	KY98-3	3.6	5182	2614		
	KY98-4	7.0	5190	1880		
7.0	KY98-5	6.9	5196	2089	1996	5%
	KY98-6	7.0	5241	2019		
	KY98-23	8.5	5323	1830		
8.0	KY98-24	7.9	5315	1811	1793	2.7%
	KY98-25	8.0	5300	1738		
	KY98-7	12.6	5210	1404		
13.2	KY98-8	13.0	5202	1288	1371	5.3%
	KY98-9	13.1	5242	1422		

Note: test temperature= -22°C

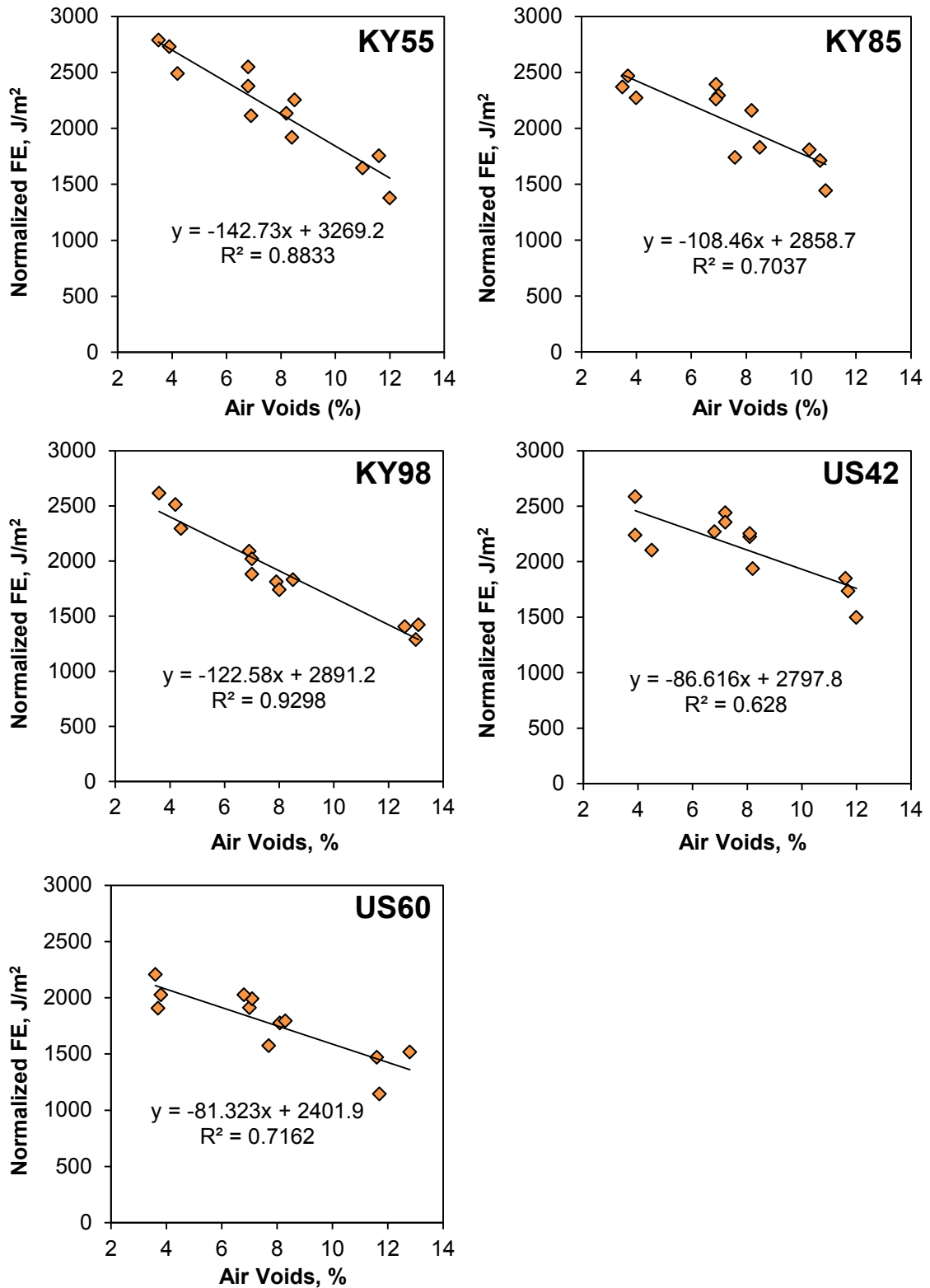**Table 5.11. Normalized Fracture Energy of US42 Mix from IRT Test**

Target Air voids (%)	Sample	Air Voids (%)	Fracture Surface Area (mm²)	Normalized Fracture Energy (J/m²)	Average FE (J/m²)	COV (%)
	US42-1	4.5	5185	2104		
4.0	US42-2	3.9	5232	2240	2310	10.8%
	US42-3	3.9	5163	2586		
	US42-4	7.2	5166	2441		
7.0	US42-5	7.2	5176	2357	2357	3.6%
	US42-6	6.8	5004	2272		
	US42-11	8.1	5168	2225		
8.0	US42-12	8.2	5106	1938	2139	8.2%
	US42-26	8.1	5176	2253		
	US42-7	12	5117	1498		
11.6	US42-8	11.6	5226	1851	1695	10.6%
	US42-9	11.7	5215	1736		

Note: test temperature= -22°C

Table 5.12. Normalized Fracture Energy of US60 Mix from IRT Test

Target Air voids (%)	Sample	Air Voids (%)	Fracture Surface Area (mm²)	Normalized Fracture Energy (J/m²)	Average FE (J/m²)	COV (%)
	US60-1	3.8	5187	2024		
4.0	US60-2	3.7	5141	1906	2045	7%
	US60-3	3.6	5204	2204		
	US60-4	7.0	5251	1910		
7.0	US60-5	7.1	5247	1989	1975	3%
	US60-6	6.8	5236	2024		
	US60-31	8.1	5030	1774		
8.0	US60-32	7.7	5120	1573	1713	7.1%
	US60-33	8.3	5127	1792		
	US60-7	12.8	5180	1517		
10.7	US60-8	11.6	5202	1468	1376	14.8%
	US60-9	11.7	5149	1142		

Note: test temperature= -22°C

Figure 5.3. Normalized Fracture Energy of the HMA Mixtures at Various Densities
Note: test temperature= -22°C

In general, fracture energy is inversely related to the cracking potential, and a mix with lower fracture energy would be more susceptible to crack. For all of the mixtures in the study, a decreasing trend was observed in the fracture energy as the air voids content increased. Figure 5.3 displays the effect of air voids content on the fracture energy of the specimens as determined by the IRT fracture test. The coefficient of variation of the fracture energy data range was 2.7 to 12.2 percent.

A series of linear regression analyses were conducted on the fracture energy data to quantify the impact of specimen air voids content on normalized fracture energy. The regression analysis revealed that the air voids had a significant impact on the fracture energy at the significance level of $\alpha=0.05$. The results showed that on average, for every one percent increase in the air voids content of the specimens, the fracture energy decreased by 143,108, 123, 87, and 81 J/m^2 for the KY55, KY85, KY98, US42, and US60 asphalt mixtures, respectively.

Table 5.13. Regression Analysis Results on Normalized Fracture Energy Data at Various Densities

Mix		DF	Parameter Estimate	Standard Error	t statistic	P-value
KY55	Intercept	1	3269.1748	133.5003	24.4881	< .0001
	Slope	1	-142.7254	16.4038	-8.7008	< .0001
KY85	Intercept	1	2858.6870	172.7127	16.5517	< .0001
	Slope	1	-108.4572	22.2539	-4.8736	0 .0006
KY98	Intercept	1	2891.1510	91.9055	31.4579	< .0001
	Slope	1	-122.5780	10.6503	-11.5094	< .0001
US42	Intercept	1	2797.8109	173.6632	16.1106	< .0001
	Slope	1	-86.61589	21.0791	-4.1091	0 .002
US60	Intercept	1	2401.8952	133.4810	17.9943	< .0001
	Slope	1	-81.3228	16.1887	-5.0234	0 .0005

In summary, three parameters were derived from the IRT fracture test data for the five HMA mixtures in the study: fracture toughness, maximum allowable crack size, and normalized fracture energy. Among these three parameters, the maximum allowable crack size (MACS) seemed to better distinguish the difference between the mixtures

since it provides more tangible information about the cracking susceptibility of the pavements. Fracture toughness has the advantage of being a fundamental material property which can be determined with various specimen geometries. However, it should be noted that fracture toughness is a very sensitive parameter and a small change in the fracture toughness results in highly significant changes in the thermal cracking performance.

5.3. Comparison to DC(t) Test Data

As a part of the KYTC density project, the field mixtures in Table 4.1 were subjected to the disk-shaped compact tension [DC(t)] fracture test to evaluate the mixtures resistance to crack propagation at low temperatures (Zeinali et al. 2014). The DC(t) data from the KYTC density project could be used to make a comparison with the IRT fracture test since the same mixtures were used for both tests.

In the DC(t) test, a tensile load at a constant displacement rate is applied on a pre-notched specimen. As the notch grows into the specimen in its cohesive zone, the load magnitude is recorded against the crack mouth opening displacement (CMOD). The fracture energy is then determined by calculating the normalized area under the recorded load–CMOD curve. Higher fracture energy indicates a more ductile mixture behavior at low temperatures and consequently, more resistance to cracking (Wagoner et al. 2006). Figure 5.4 depicts the DC(t) apparatus test that was used in this study.

The DC(t) test in this part of the study was conducted in accordance with the ASTM D7313 (2013) standard method. For each mixture, two sets of triplicate specimens were tested which were produced at two air void levels:

- 8 percent air voids, the desirable level after compaction in the field, and
- Average in-place air voids of each pavement as measured in the field (Table 5.1).

These air void levels were selected to determine whether the pavement would provide a better low-temperature performance if it had been compacted at the desirable air voids level of 8 percent. The DC(t) specimens were made with 50-mm thickness and within the ±0.5 percent of their specified air voids in the experimental plan. The DC(t) test results at

-22°C are illustrated in Figure 5.5. Each diagram in this figure shows the fracture energy of a mixture at two density levels as well as the linear regression line for each dataset.
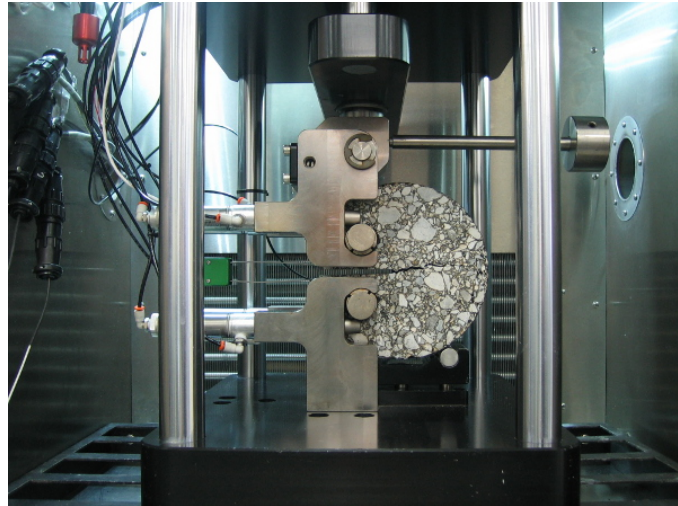
Figure 5.4. DC(t) Test Apparatus

The difference between the capability of the IRT and DC(t) tests in capturing the variations in the material properties can be evaluated by comparing the data in Figure 5.5 to those in Figures 5.1, 5.2, and 5.3. This comparison reveals that the variability in the DC(t) fracture energy data is higher than all three parameters measured form the IRT fracture tests: plane-strain fracture toughness, maximum allowable crack size, and IRT normalized fracture energy. A series of linear regression analyses was performed on the DC(t) fracture energy data, which was similar to the analysis on the IRT fracture test data. These regression analyses, as presented in Table 5.14, did not conclude that specimen density has a significant effect on reducing the fracture energy. In other words, the DC(t) test could not effectively discern the impact of air voids content on cracking susceptibility.

It is noteworthy to mention that DC(t) fracture energy is highly influenced by the specimen geometry, its stiffness, and both elastic and permanent deformations of the test specimen during the test. Consequently, the resulting fracture energy as normalized on cohesive zone can be different from one test to another. However, the data could be used to rank the potential cracking performance of various asphalt mixtures.
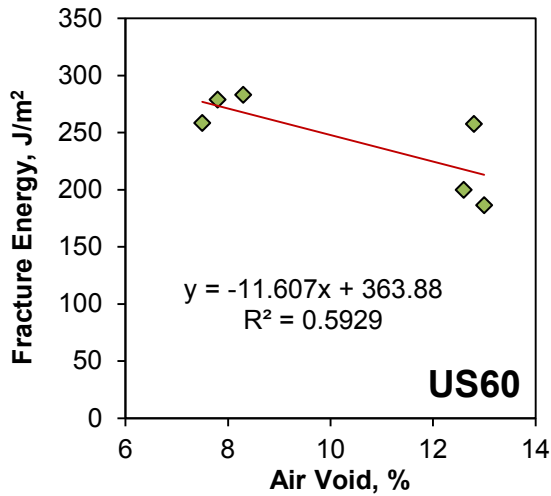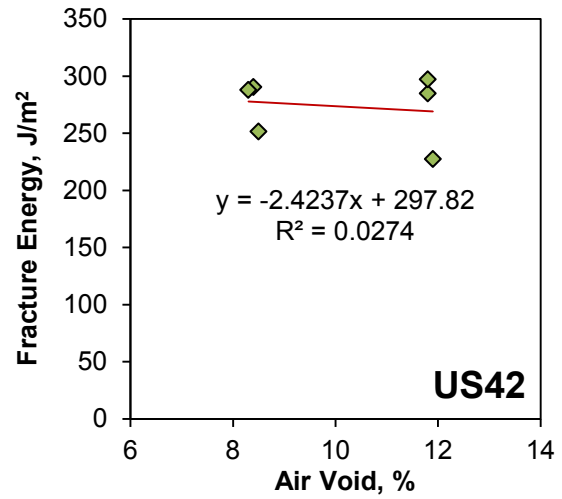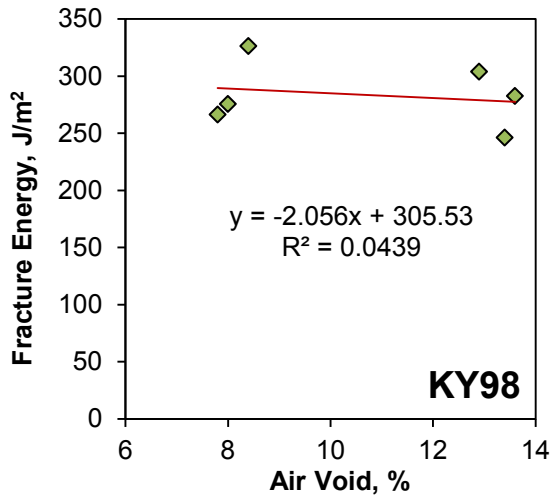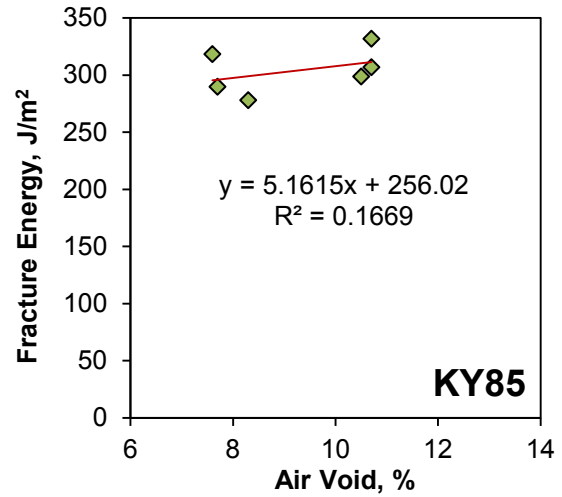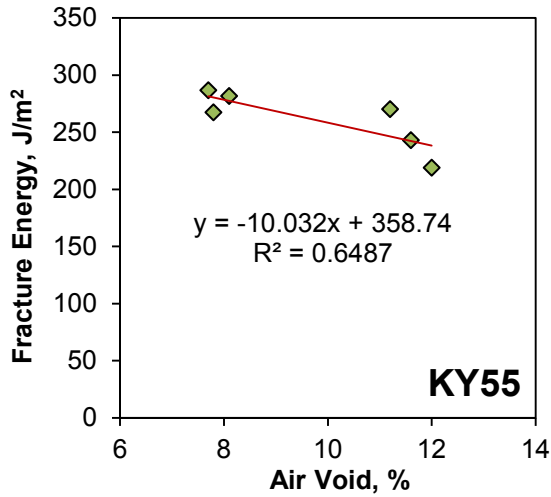
Figure 5.5. DC(t) Fracture Energy for the HMA Mixes at Various Densities
Note: test temperature= -22°C

Table 5.14. Regression Analysis Results on DC(t) Data at Various Densities

Mix		DF	Parameter Estimate	Standard Error	*t* statistic	P-value
KY55	Intercept	1	358.7424	36.5928	9.8036	0.0006
	Slope	1	-10.0317	3.6910	-2.7179	0.0531
KY85	Intercept	1	256.0227	53.9375	4.7467	0.0090
	Slope	1	5.1615	5.7652	0.8953	0.4212
KY98	Intercept	1	305.5319	52.8050	5.7860	0.0044
	Slope	1	-2.0560	4.7994	-0.4284	0.6904
US42	Intercept	1	297.8199	74.0821	4.0201	0.0159
	Slope	1	-2.4237	7.2194	-0.3357	0.7540
US60	Intercept	1	363.8761	51.1039	7.1203	0.0021
	Slope	1	-11.6074	4.8089	-2.4137	0.0733

CHAPTER 6
SENSITIVITY OF IRT FRACTURE TEST TO ASPHALT AGING

Hot-mix asphalt (HMA) is an engineering material which is composed of asphalt binder and mineral aggregates. The brittleness of an HMA mix is highly dependent upon the stiffness of the binder that is incorporated into the aggregate. Asphalt binder is only one of the many products that are refined from crude oil, and it undergoes an oxidative reaction with air continuously during its production and in service (Asphalt Institute 2008). Oxidation of the asphalt molecules takes place over years; however, this gradual reaction can translate into substantial changes in the mechanical properties of asphalt after a few years.

In the most prominent form, oxidative aging of asphalt binders manifests itself in the form of a non-reversible stiffening and hardening of asphalt. The degree of stiffening and hardening of binder is also a function of its crude source and chemical composition (Branthaver et al. 1993). Moreover, the oxidative reaction of asphalt molecules makes the asphalt material more brittle and undermines its stress relaxation capabilities. Thus, HMA pavements become more susceptible to cracking as they age. At the pavement surface, where the asphalt is exposed to the traffic and environmental factors, the rate of aging is faster than in deeper layers. As the result, aging creates a gradient in the material properties due to variation in the amount of aging across the depth of pavement.

Two primary stages are typically defined for oxidative aging of asphalt (Mirza and Witczak 1996):

- Short-term aging, which occurs during the production, hauling, placement, and compaction of the HMA pavement.
- Long-term aging, which takes place in the field and during the service life of the pavement.

Due to the higher temperatures of asphalt during the construction process, the short-term oxidative reaction takes place at a faster rate. This process in a laboratory is typically simulated by conditioning the HMA samples in a forced-draft oven.

To simulate the short-term aging, 4 hours of loose-mix conditioning at 135°C was recommended for HMA at the end of the Strategic Highway Research Program (Bell et al. 1994) for both volumetric design and mechanical testing. To expedite the mixture design process and reduce the number of ovens required for mixture design, the FHWA Mixtures and Aggregates Expert Task Group (ETG) recommended that the short-term oven conditioning time for mixture design be changed to two hours at the compaction temperature. These recommendations were later standardized under AASHTO R 30 (2002) practice.

According to AASHTO R 30, to simulate long-term aging, compacted specimens must be conditioned at 85°C for five days in a forced-draft oven. Nonetheless, this method has not shown to be practical in aging the HMA specimens (Braham et al. 2009; Azari and Mohseni 2013). Instead, a modified loose-mix conditioning has been developed by researchers which recommends for the loose HMA samples to be conditioned at 135°C for 24 hours (Zeinali et al. 2014; Blankenship et al. 2010; Braham et al. 2009). For this type of conditioning, the loose-mix samples are spread in metal pans at 25 to 50 millimeters depth.

The modified long-term oven aging was used in this part of the study to execute an experimental study to investigate the effect of aging via the IRT fracture testing. This experimental study would reveal whether the IRT fracture test is capable of distinguishing the changes that occur in the HMA material properties as a result of long-term oven aging. This study would also provide more information about the changes that may occur in the low-temperature performance of the asphalt pavements as they age and become more brittle.

6.1 Materials and Test Matrix

Four out of five HMA mixtures from the KYTC Density project (Table 4.1) were used in the experimental study on HMA aging: KY55 (Adair County), KY85 (Ohio County), KY98 (Allen County), US42 (Oldham County). Before compaction, two different conditioning methods were performed on the loose-mix samples:

1- 0-hr conditioning: loose- mix samples were reheated in metal pans until they reached the compaction temperature. Since the samples had been collected from hauling trucks, they had already undergone the short-term aging in the field. Therefore, the metal pans were covered with aluminum foil during the laboratory heating to minimize aging during this period of time.

2- 24-hr conditioning: loose-mix samples were conditioned at 135°C for 24 hours. The samples were spread in a single metal pan at the depth of 40 millimeters during the 24-hr conditioning.

After conditioning, all the samples were compacted to 8.0±0.5 percent air voids. This air voids level was selected to make the data comparable to those of the KYTC Density project. The IRT fracture test specimens were produced according to the procedures developed in Chapter 3. For each mix, the IRT fracture test was conducted at three temperatures and two conditioning types. Triplicate specimens were tested for each combination and 72 specimens were tested in total for this experimental study.

6.2 IRT Fracture Test Data

6.2.1 Fracture Toughness Results

The IRT fracture test was conducted at -2, -12, and -22°C for each HMA type. The original load-displacement plots for these tests are shown in Appendix C. The test data were then used in conjunction with Equation 3.1 to calculate the fracture toughness of the mixtures at various temperatures and aging durations. Figure 6.1 displays the variation of the fracture toughness of the mixtures at various temperatures and conditioning durations. The variation of fracture toughness with respect to test temperature in these plots follows the same pattern that was observed in the test development procedure (Figure 3.14). The Tukey's HSD pairwise comparison that was conducted on the data showed that by decreasing the temperature from -2°C to -12°C, the fracture toughness of all mixtures increased significantly. Nonetheless, no significant change in fracture toughness was observed by further decreasing the temperature to -22°C.
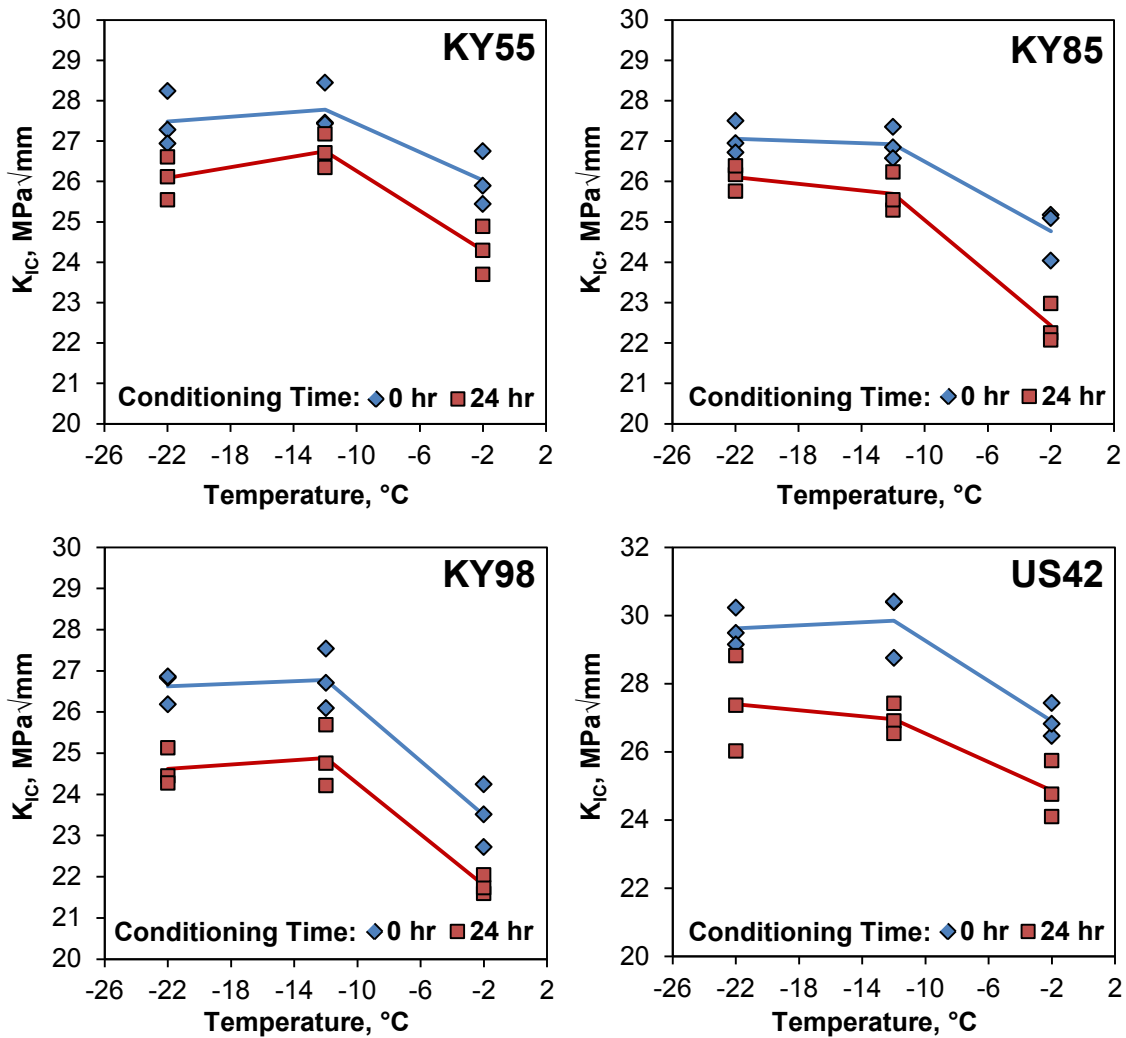
Figure 6.1. Fracture Toughness of the HMA Mixtures after Short-Term and Long-Term Aging

A set of statistical one-tail t-tests were conducted on the data to see if the long-term conditioning had a significant effect on fracture toughness (K_{IC}) of the HMA mixtures. The t-tests compared the means of K_{IC} data at each temperature with two different aging durations. The resulting p-vlaues from t-tests are presented in Table 6.1. This analysis showed that long-term aging of the mixture significantly decreased the fracture toughness of all HMA mixtures at all temperatures at the confidence level of α=0.05. In general, the IRT fracture test showed an acceptable capability in discerning the long-term aging of the mixtures. Additionally, K_{IC} seemed to be a good indicator of

the HMA mixtures brittleness and the changes that long-term aging caused in their properties.

Table 6.1. P-Values from t-Tests on the K_{IC} Data with Two Different Conditioning Durations

Mix	P-value		
	-2°C	-12°C	-22°C
KY55	0.01403	0.03324	0.02404
KY85	0.00346	0.01351	0.01598
KY98	0.01035	0.01744	0.00206
US42	0.01064	0.00441	0.03134

6.2.2 Fracture Energy Data

The fracture energy of the IRT specimens was calculated by the normalized area under the load-displacement curve. Figure 6.2 illustrates the fracture energy data at various temperatures and conditioning durations. A set of statistical one-tail t-tests, similar to the analysis on K_{IC} data, was conducted on the fracture energy data. The resulting P-values are presented in Table 6.2. At the confidence level of $\alpha=0.05$, the t-tests showed a significant difference between the mixtures with different conditioning durations at -2°C. However, at -12°C and -22°C, the statistical results were not conclusive. Overall, the conditioning duration seemed to have a significant impact on the fracture energy at -2°C, however, by further decreasing the temperature, the difference between the fracture energy data for various conditioning durations diminished.

Table 6.2. P-Values from t-Tests on the Fracture Energy Data with Two Different Conditioning Durations

Mix	P-value		
	-2°C	-12°C	-22°C
KY55	0.01280	0.00892	0.07199
KY85	0.0111	0.30229	0.02663
KY98	0.00652	0.19544	0.11516
US42	0.00376	0.01001	0.02536

Note: gray cells indicate non-significant effects at $\alpha=0.05$
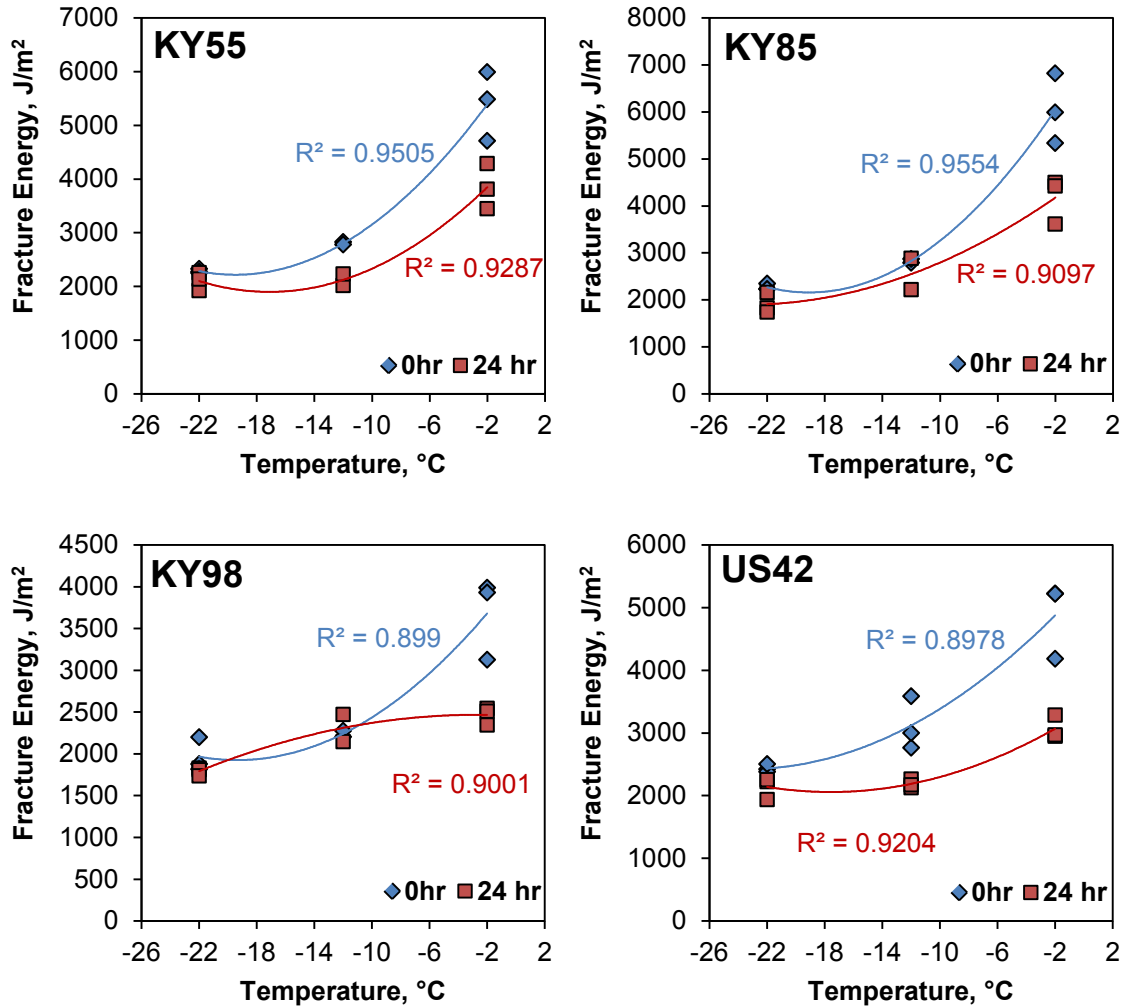
Figure 6.2. Fracture Energy of the HMA Mixtures after Short-Term and Long Term Aging

A multiple linear regression analysis was utilized to evaluate the overall impact of the test temperature and conditioning duration on the IRT normalized fracture energy. The MLR model was:

$$Y = b_0 + b_1 . X_1 + b_2 . X_2 \qquad (6.1)$$

where,

Y: fracture energy (J/m^2)
X_1: test temperature (°C)
X_2: aging duration (0 or 24 hours)
b_0, b_1, b_2: regression constants

110

The summary of the multiple linear regression analysis results is shown in Table 6.3. The regression coefficient b_1 (Temperature) indicates that how much the fracture energy changes on average for 1°C decrease in the test temperature while keeping the conditioning time constant. Similarly, the coefficient b_2 (Aging) indicates how much the fracture energy changed on average if the conditioning time increased by one hour while keeping the test temperature constant. The multiple linear regression analysis revealed that the overall effect of both test temperature and conditioning duration on the fracture energy was significant for all the mixtures in the study. In general, the statistical analysis indicated that the mixtures became more susceptible to cracking as they were aged for a longer duration, or tested at lower temperatures.

Table 6.3. Results of Multiple Linear Regression Analysis on Fracture Energy Data

Mix		DF	Parameter Estimate	Standard Error	t Statistic	P-value	Standardized Estimate
	Intercept	1	4907.0111	328.5714	14.93	<.0001	0
KY55	Temperature	1	121.4083	19.7301	6.15	<.0001	0.80461
	Aging	1	-31.8333	13.4246	-2.37	0.0315	-0.31006
	Intercept	1	5466	373.7427	14.63	<.0001	0
KY85	Temperature	1	151.0833	22.4425	6.73	<.0001	0.83485
	Aging	1	-33.1204	15.270	-2.17	0.0466	-0.26898
	Intercept	1	3418.4556	178.6941	19.13	<.0001	0
KY98	Temperature	1	59.7417	10.7302	5.57	<.0001	0.74614
	Aging	1	-22.7176	7.3010	-3.11	0.0071	-0.41699
	Intercept	1	4488.2778	243.8794	18.4	<.0001	0
US42	Temperature	1	84.2917	14.6445	5.76	<.0001	0.70836
	Aging	1	-42.15278	9.96431	-4.23	0.0007	-0.52062

Since the temperature and conditioning time are two physical variables with different measuring units, the importance of their effects on normalized fracture energy cannot be compared directly with their physical units. A standardized partial regression coefficient can be used to rank the independent variables in terms of their relative importance on the response variable, regardless of their units. The standardized estimates are computed by multiplying the original estimates by the standard deviation of the

regressor (independent) variable and then dividing by the standard deviation of the dependent variable.

The standardized partial regression coefficients were generated for the IRT fracture test data, and presented in the Table 6.3. A comparison between the standardized estimated values for Temperature and Aging coefficients showed that the test temperature was slightly more impactful on fracture energy than aging duration in the analyzed range. It should be noted that using a linear regression model does not necessarily signify that there is a causal relationship between the fracture energy and aging time or test temperature.

In summary, fracture energy seemed to be sensitive to aging duration at -2°C. However, at -12°C and -22°C, fracture energy did not distinguish the change in material properties. The reason behind this could be the sensitivity of the fracture energy to the specimen stiffness. By reducing the temperature, the rate of change in the specimen stiffness slows down and consequently, the fracture energy becomes less sensitive to the changes in material property.

FUTURE RESEARCH SUGGESTIONS

The primary focus of this research was to develop an implementable and repeatable test for characterizing the fracture properties of HMA. The background on development of the test and measuring the elastic fracture properties of the HMA was also covered in the research. Although the test results showed a brittle fracture at below glass transition temperatures, further research is required to determine whether a significant portion of the fracture energy has been consumed in plastic deformation of the material in the vicinity of the notch tip. The results of such research would assist in refining a fracture-based model to analyze low-temperature cracking in asphalt pavements. Such an analysis should also account for the effect of repeated environmental and traffic loading on changing the fracture properties of HMA.

In order to standardize the IRT fracture test by American Society for Testing and Materials (ASTM), more experiments re required on the possible factors that may influence the test results. Such experimental studies may include testing at different temperatures with small intervals, various sample sizes, and different binder types. The minimum specimen thickness to satisfy the plane-strain conditions can also be determined more accurately from such studies.

The experimental studies which were conducted during this research revealed that the IRT test has a good capability in discerning the variations in asphalt mixtures. An analysis method was also developed to correlate the test results to field performance. To examine the accuracy of this analysis and find a better correlation to pavements performance, the analysis results should be compared and calibrated to the thermal cracking data of the pavements which can be collected by field cracking surveys. Moreover, implementing the test at the DOT level requires a full understanding of the variables that may affect the test results as well as the test's response to a wide range of various mixture properties.

SYNOPSIS AND CONCLUSIONS

The Indirect Ring Tension (IRT) fracture test, which is also known as Kentucky Fracture Test (KFT), was developed as a user-friendly tool for fracture characterization of hot-mix asphalt. An IRT fracture specimen is basically made from a cylindrical sample of HMA. To make an IRT fracture specimen, first, a disk-shaped specimen of HMA is cut from a gyratory compacted sample or a field core. Then, a small cylinder is cored out from the center of the disk-shaped sample to form a ring-shaped specimen. Then, a cutting device is passed through the central hole to cut two notches with equal lengths along the diametrical loading line, on two sides of the central circle.

The IRT test proved to be very effective in measuring the fundamental fracture properties of hot-mix asphalt (HMA) while maintaining its practicality and user-friendliness. In general, the IRT test seemed to be advantageous over all other existing test configurations for low-temperature fracture characterization of HMA. The simplicity of the IRT test configuration combined with the widespread availability of its test device enables preforming the test at the state highway agency level. The main advantages of the IRT fracture test include:

- Potential for low-cost implementation at the highway agencies level
- Capability of testing both field cores and laboratory-compacted samples
- Execution with the existing equipment in most HMA laboratories
- Simulating the stress distribution of an HMA layer under low-temperature tensile loads
- Clearly distinguishing the transition of HMA from ductile to quasi-brittle phase
- Producing a straight crack growth pattern and mode-I fracture on a relatively consistent basis
- Higher repeatability than other fracture tests currently in use for HMA
- Relatively large fracture surface zone

To develop a fracture-mechanics-based test, the stress intensity factor formula for the IRT geometry was calibrated by a numerical solution method. Finite element (FE) modeling was used to calculate the stress distribution and displacement of IRT test, and obtain the mode-I stress intensity factor based upon the solution results. In order to

develop a comprehensive numerical solution, numerous FE models were generated with various geometric parameters (inner radius, outer radius, and notch length) and under different loads. Crack tip elements were used in the FE models to account for the singularity of the stress at the crack tip and produce accurate displacement data. Moreover, the loading platens were included in the model to account for the effect of load distribution on the specimen surface.

The finite element model was verified by simplifying it to the centrally cracked IDT specimen and comparing its FE results to the closed-form solutions in the literature. After satisfactory verification of the model, the results of more than 3600 FE model runs were consolidated in the form of a single equation, which allows for fracture toughness (K_{IC}) and fatigue fracture testing of linear elastic materials using the IRT specimen with a range of dimensions. This equation provides the user with the versatility to fabricate the IRT specimen with the existing equipment in the laboratory and desirable dimensions.

An experimental plan was designed to develop a procedure for running the IRT fracture test at low temperatures. The goal of this part of the study was to determine the optimal loading rate and testing temperature for the IRT fracture test to capture the linear elastic fracture properties of HMA with high repeatability. This optimization was performed by testing two plant-produced mixtures which were collected for a Kentucky Transportation Cabinet research project. One of the HMA mixtures was produced with a neat PG 64-22 and another was produced with a polymer-modified PG 76-22 binder. All the tests in this research study were conducted at the Asphalt Institute's laboratory using fully calibrated equipment.

To find the optimal loading rate for the IRT fracture test, a set of specimens were tested at three different monotonic loading rates: 12.5, 1.0 and 0.1 mm/min. Then, the plane-strain fracture toughness (K_{IC}) of each specimen was calculated by the newly developed K_I calibration equation. Additionally, the normalized fracture energy of the specimens was determined by calculating the area under the load-displacement curve and normalizing it over the fracture surface area. Based upon the statistical analysis on the data, an optimal loading rate of 1.0 mm/min was recommended for the test. The IRT test exhibited a strong capability in detecting the differences in fracture potential between the field-produced mixes. Both mixtures were made with PG XX-22 binders, which means

based upon binder test data alone their low temperature cracking potential would be expected to be identical. However, the IRT fracture test captured a significant difference between these HMA mixes in terms of their cracking susceptibility at low temperatures.

To determine proper IRT test protocols, and to examine the effect of test temperature on the fracture properties of the mixtures, triplicate samples from both field mixtures were tested at 2°C, -12°C, and -22°C. At -2°C, when the asphalt had not entered the brittle phase yet, the HMA specimens exhibited gradual and ductile crack propagation after the initial crack growth. However, at -12°C and -22°C, when the asphalt was in brittle phase, a sudden and brittle fracture was observed after the initial crack growth. In fact, the test showed a noteworthy capability in capturing the ductile-to-brittle transition of HMA. Further analysis revealed that decreasing the temperature from -12°C to -22°C did not cause a significant change in the K_{IC} value. At these temperatures, the test data passed the requirements of the ASTM E399 test for linear elastic fracture test. However, at -2°C, the specimen experienced a significant amount of permanent deformation and the linear elastic conditions did not exist. Therefore, the plane-strain fracture toughness of these mixtures could not account for all the energy that was consumed in the specimen fracture.

In addition to the fundamental fracture properties, the relaxation properties of HMA have an important impact on its cracking susceptibility. An analysis method was developed to generate a cracking susceptibility indicator for HMA material based on both fracture and relaxation properties. To perform this analysis, a set of creep compliance tests was conducted at various temperatures on five plant-produced mixtures which were collected from highway project in central Kentucky area. The creep compliance master curve data for each mixture were then converted to stress relaxation modulus through numerical methods. A viscoelastic model was developed to calculate the thermally-induced tensile stress in the pavements for a hypothetical cooling scenario.

By employing the linear fracture mechanics theory, IRT fracture test data, and using the thermal stress analysis, the maximum allowable crack sizes (MACS) were calculated for a range of various temperatures. MACS at each temperature represents the smallest crack size in the pavement that would start growing as the pavement temperature drops to the designated temperature according to the hypothetical cooling scenario (the

mixture with a larger MACS is expected to perform better at low temperatures). This analysis showed a highly significant difference between the cracking susceptibility of the HMA mixtures even though they were all produced with PG XX-22 asphalt binders. Moreover, it was concluded that a slight difference between the measured fracture toughness values by IRT fracture test leads to a highly significant difference in the predicted maximum allowable crack size of the pavements.

The MACS analysis can be utilized to evaluate the effect of mixture properties on its thermal cracking potential. One of the most important factors that influence a pavement performance is its in-place density. An experimental study was executed to examine the effect of HMA density (or air voids content) on its thermal cracking potential through IRT fracture testing and MACS analysis. Five plant-produced mixtures from the KYTC density project were used in this experimental study. The mix samples were collected from construction sites whose in-place air voids content were higher than the target value of 8 percent. The IRT specimens were fabricated for each mix at various air void contents ranging from 4 percent to the pavement's average in-place air voids content as measured at several locations in the field.

The results of the experimental study on specimens with various densities revealed a significant correlation between the mixture density and the cracking susceptibility. Three thermal cracking parameters were determined from the analysis for each mix: fracture toughness, maximum allowable crack size, and fracture energy. All three parameters indicated that by increasing the air voids content (or decreasing density), the cracking susceptibility of the mixtures increased significantly. Furthermore, this study concluded that the pavements in the study would exhibit a better low-temperature performance if they had been compacted to 8 percent air voids during the construction.

Another factor that has a high impact on the low-temperature performance of HMA pavements is oxidative aging of asphalt materials. Continuous oxidation of asphalt in the field undermines the relaxation properties and results in more brittle HMA. An experimental study was conducted to evaluate the effect of aging on low-temperature performance of HMA by means of the IRT fracture test. In order to simulate the long-term aging of HMA mixtures, the loose-mix samples, which were collected in the field, were aged in a forced-draft oven at 135°C for 24 hours. Four mixtures were subjected to

long-term laboratory aging and compacted. As the control point, a set of samples were only reheated with no extra aging and compacted to make the IRT specimens.

For this experimental study, the HMA mixtures were tested for IRT fracture toughness and fracture energy at three temperatures (-2, -12, -22°C) and two aging durations (0-hr and 24-hr aging durations). The data analysis concluded that long-term laboratory aging significantly lowered the fracture toughness of all four mixtures at all tested temperatures. Additionally, the overall relationship between the obtained K_{IC} data and the temperature was similar for all mixtures. The normalized fracture energy data showed that the long-term aging had a high impact on the mixtures stiffness and resulted in increased cracking potential for the mixtures. The fracture energy seemed to vary more quickly with respect to temperature at -2°C. By lowering the test temperature, the sensitivity of fracture energy data to test temperature decreased. This could be due to the dependency of normalized fracture energy on the mix stiffness. The statistical analysis showed that the test temperature was slightly more influential on fracture energy than aging duration in the analyzed range.

In summary, the IRT test proved to be a useful tool for evaluating the HMA material performance at low temperatures. The test showed to be capable of discerning the differences between the mixtures and can be utilized to rank HMA mixtures based on their thermal cracking potential. Considering the findings and observations of this research, it is recommended that this test be slated for trial implementation at the state highway agency level.

APPENDIX A
CREEP COMPLIANCE TEST DATA
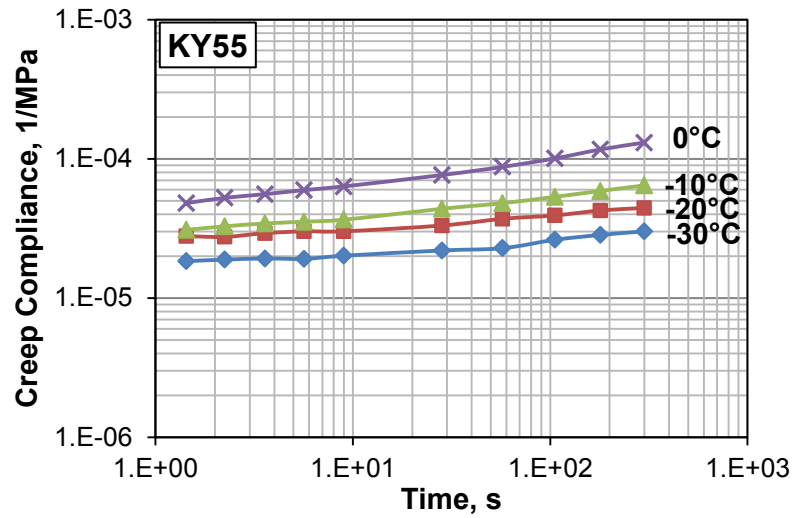
Figure A.1. Isothermal Creep Compliance Test Data for KY55 Mix
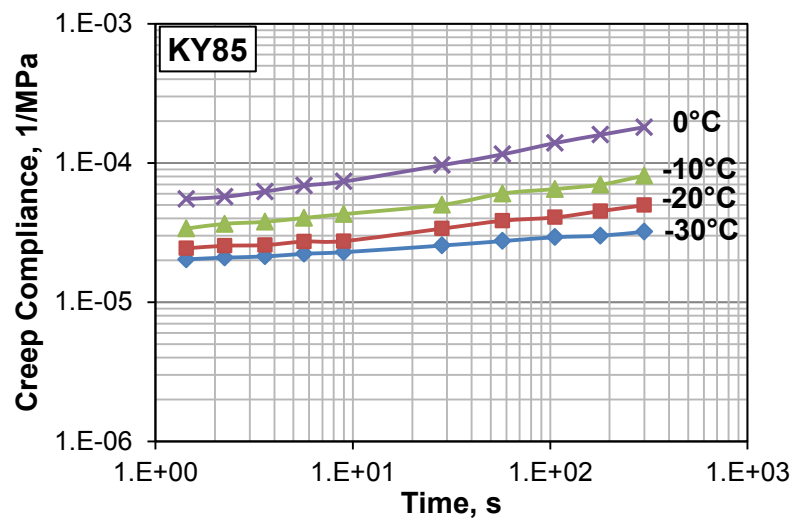
Figure A.2. Isothermal Creep Compliance Test Data for KY85 Mix
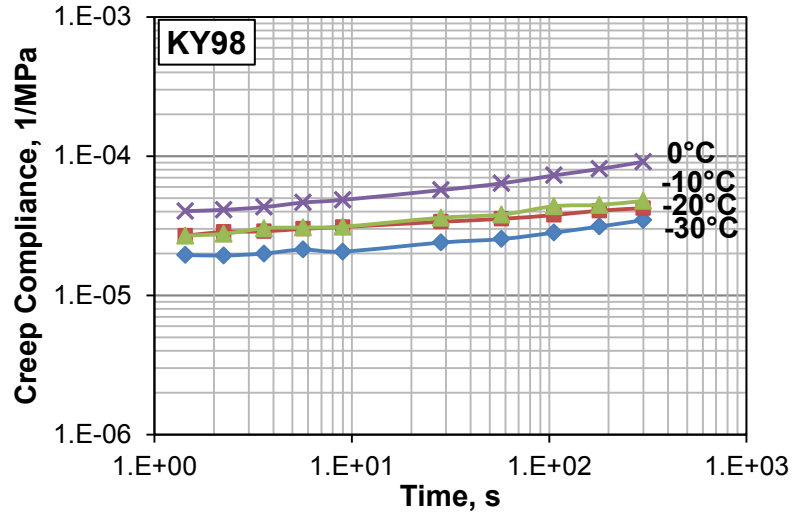
Figure A.3. Isothermal Creep Compliance Test Data for KY98 Mix
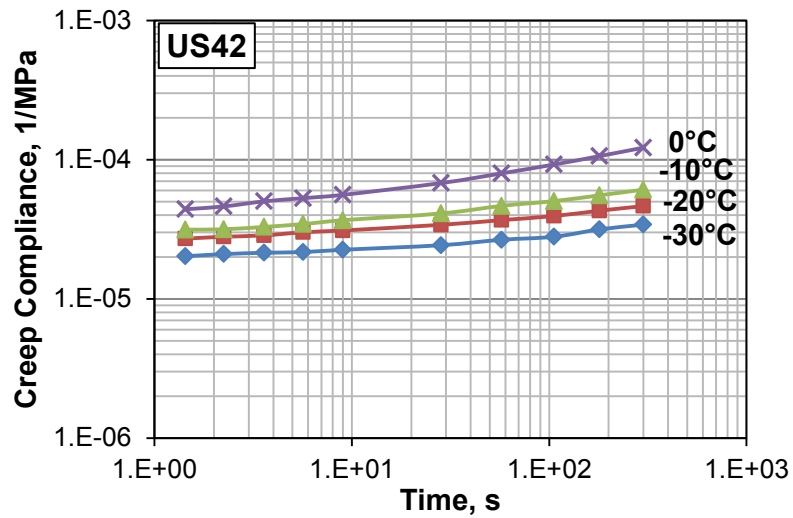
Figure A.4. Isothermal Creep Compliance Test Data for US42 Mix
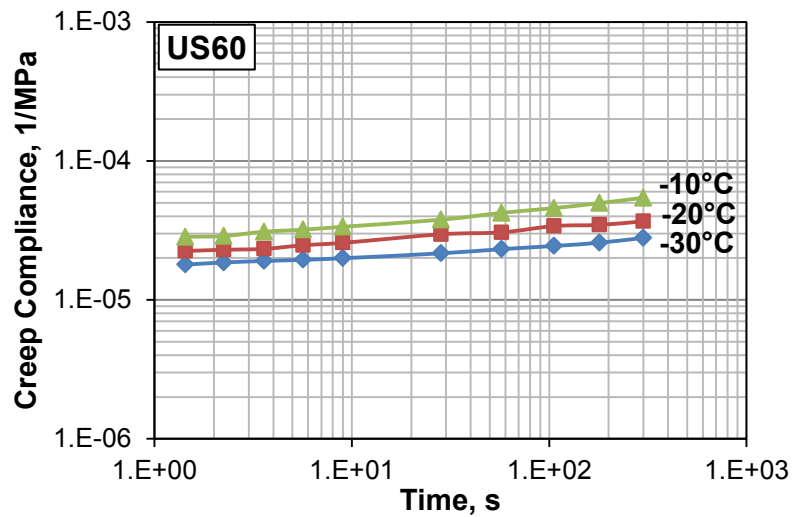
Figure A.5. Isothermal Creep Compliance Test Data for US60 Mix
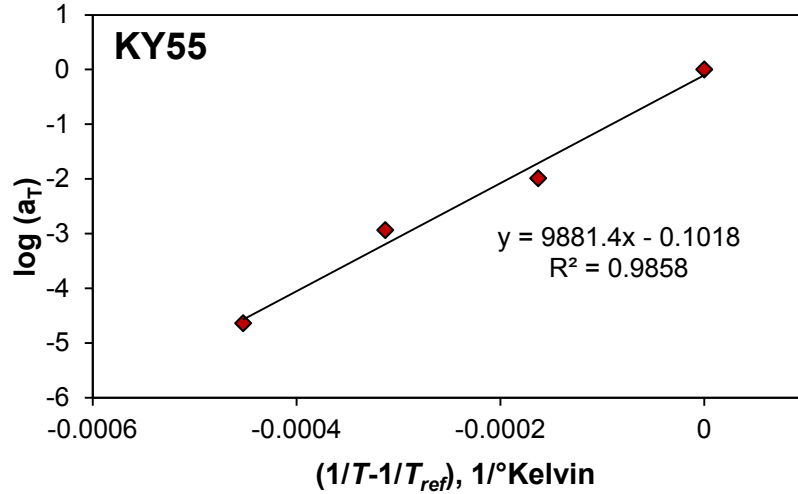
Figure A.6. Shift Factors and Arrhenius Function for KY55 Mix
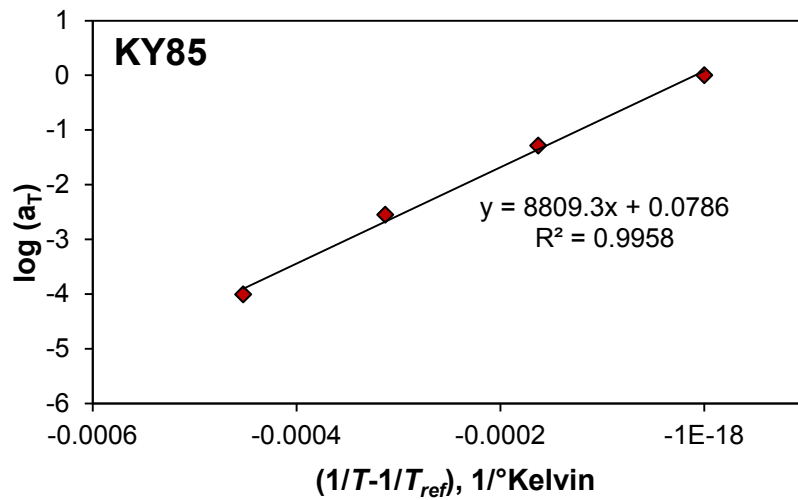
Figure A.7. Shift Factors and Arrhenius Function for KY85 Mix
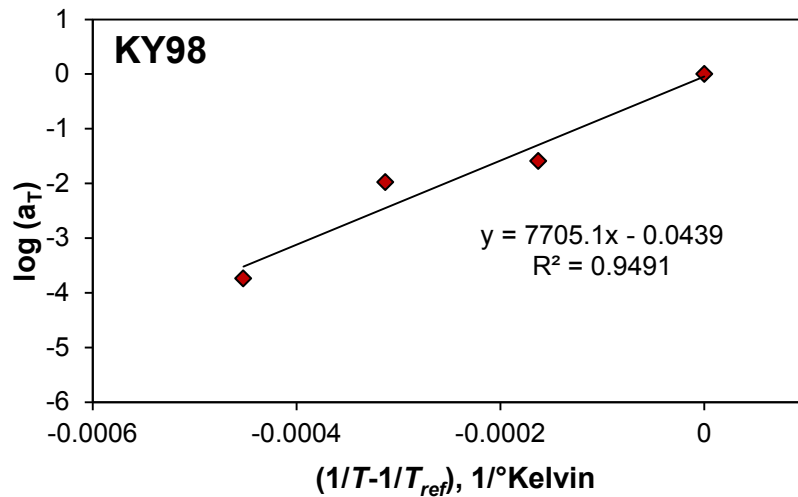
Figure A.8. Shift Factors and Arrhenius Function for KY98 Mix
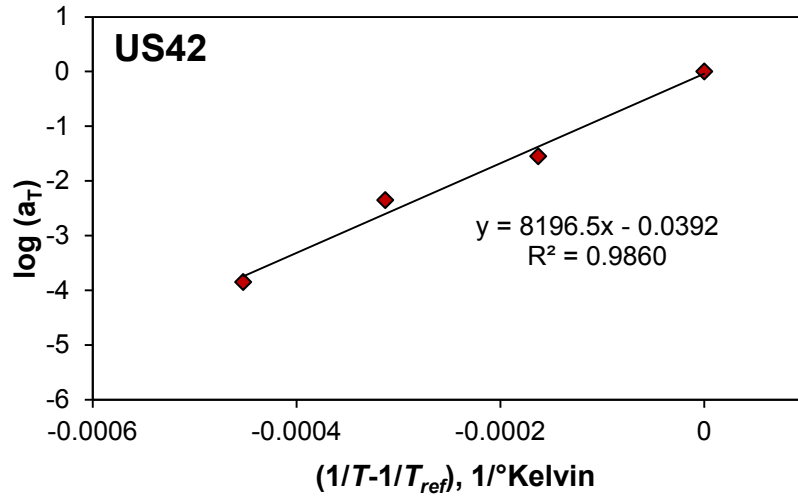
Figure A.9. Shift Factors and Arrhenius Function for US42 Mix
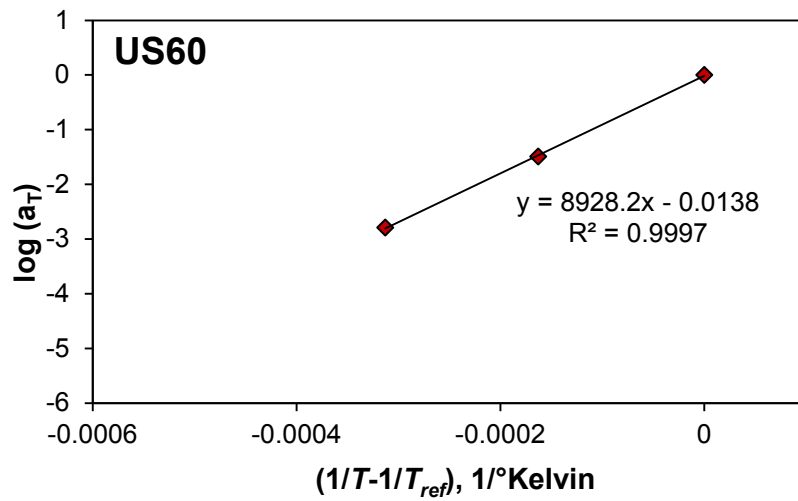
Figure A.10. Shift Factors and Arrhenius Function for US60 Mix

APPENDIX B
IRT FRACTURE TEST DATA FOR DENSITY STUDY
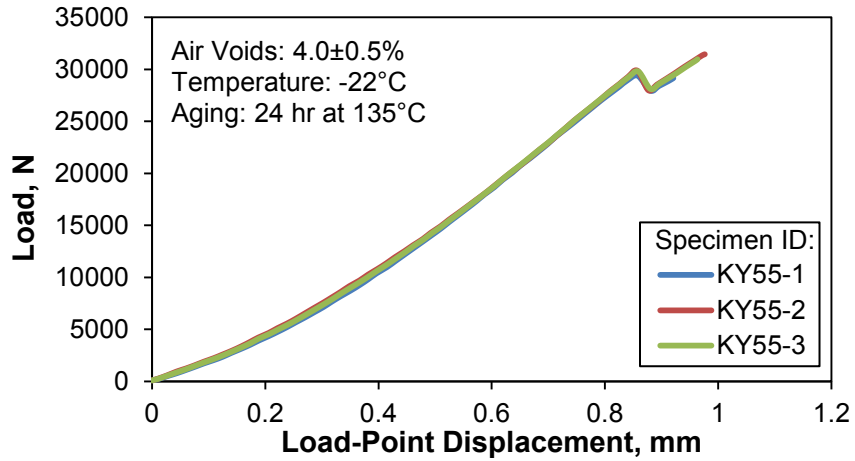
Figure B.1. IRT Fracture Test Data for KY55 Mix with 4.0% Air Voids
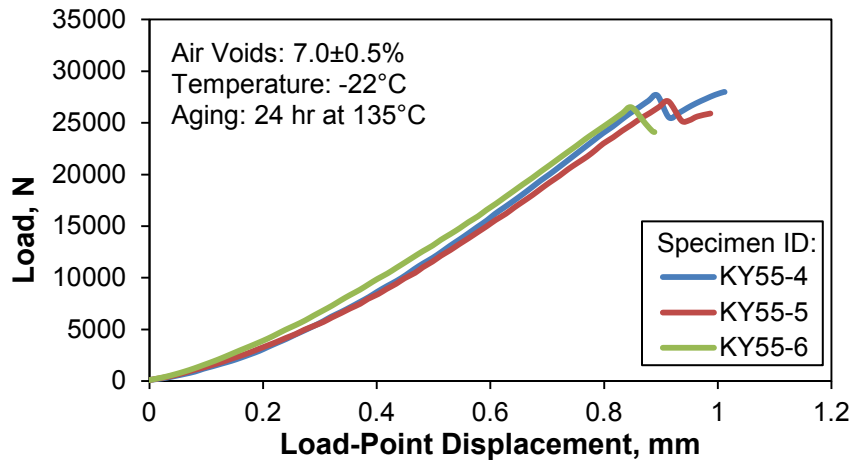
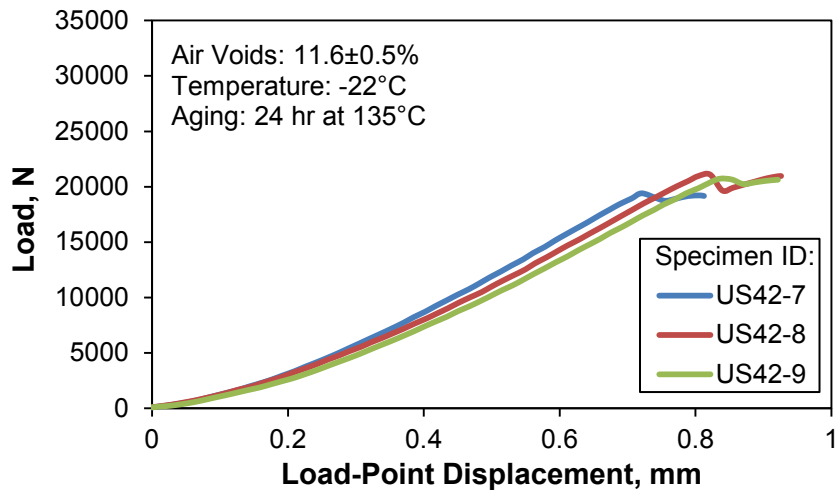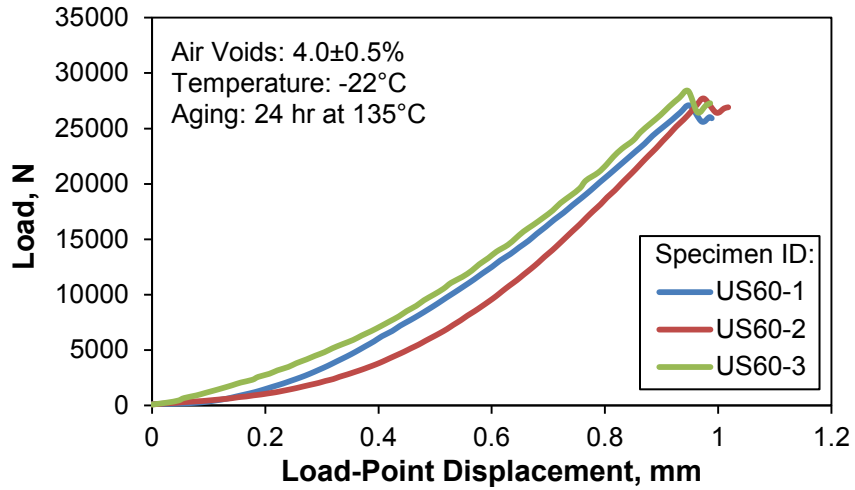**Figure B.2. IRT Fracture Test Data for KY55 Mix with 7.0% Air Voids**
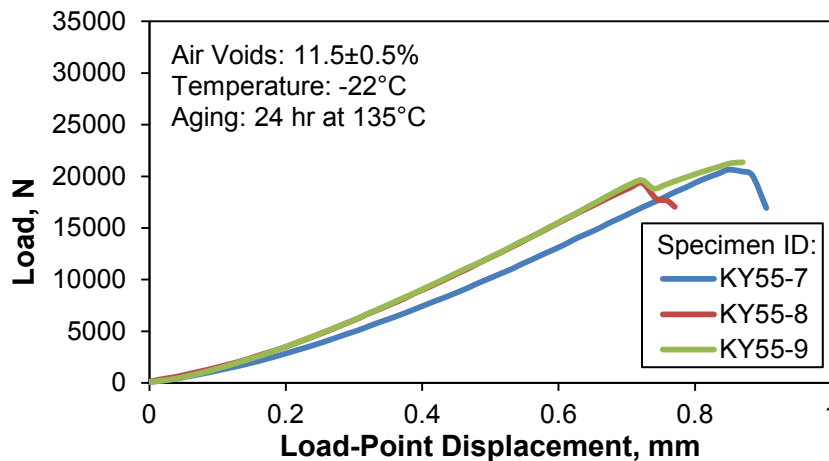
Figure B.3. IRT Fracture Test Data for KY55 Mix with 11.5% Air Voids
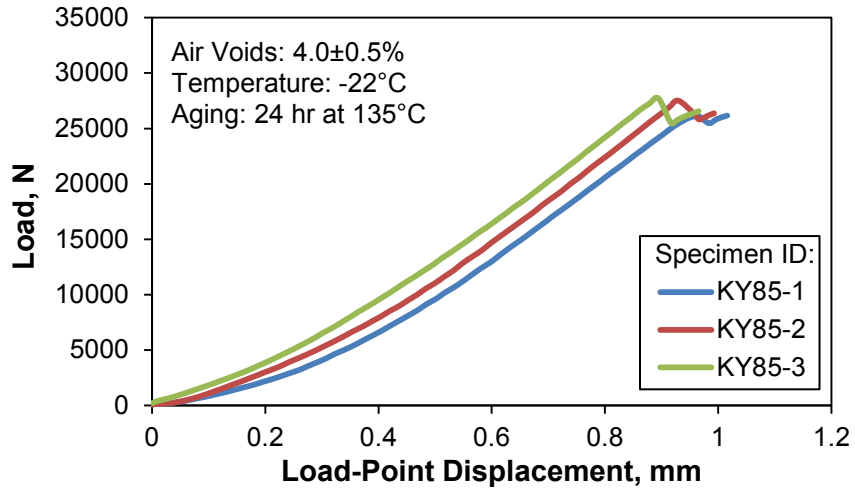
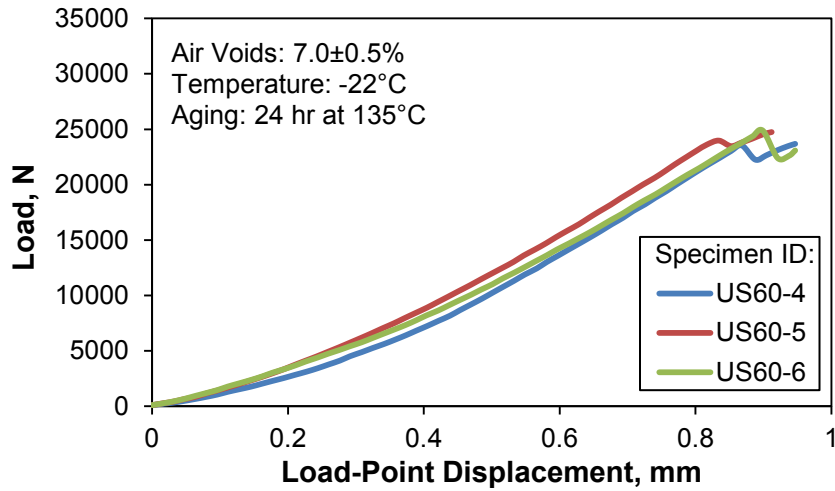**Figure B.4. IRT Fracture Test Data for KY85 Mix with 4.0% Air Voids**
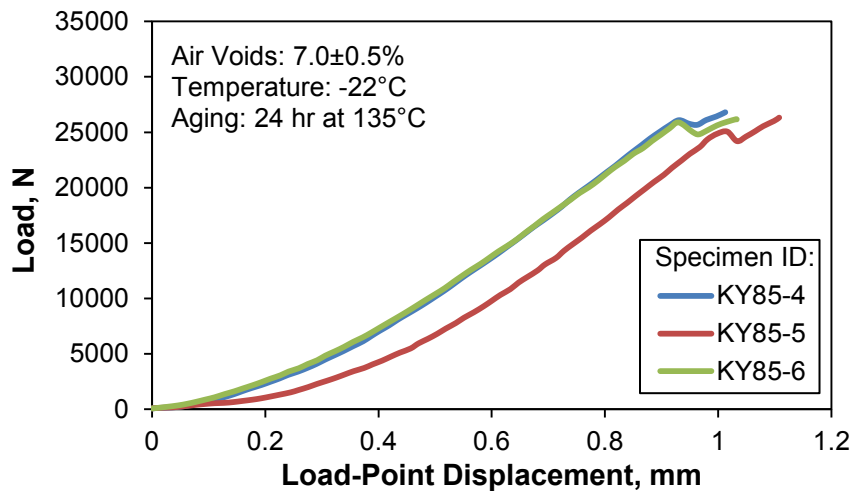
Figure B.5. IRT Fracture Test Data for KY85 Mix with 7.0% Air Voids
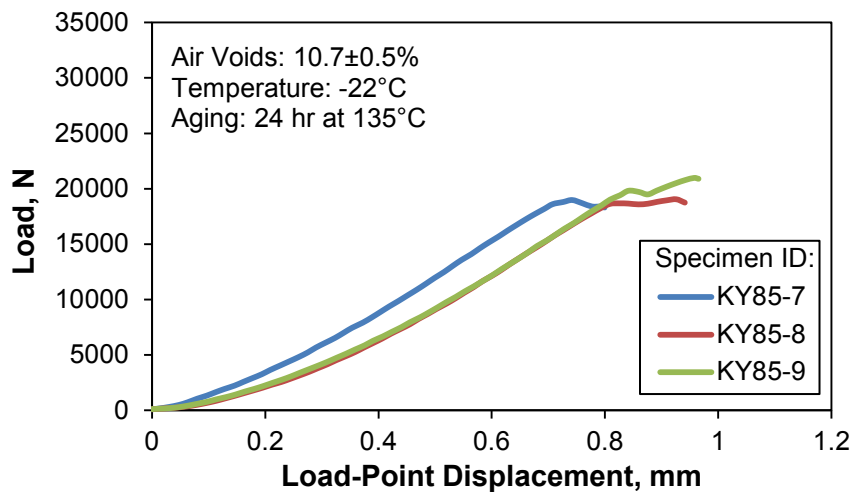
Figure B.6. IRT Fracture Test Data for KY85 Mix with 10.7% Air Voids
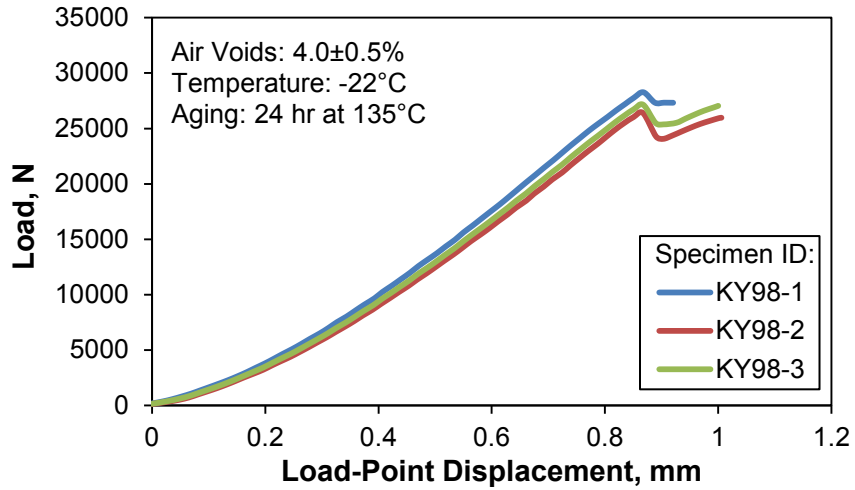
Figure B.7. IRT Fracture Test Data for KY98 Mix with 4.0% Air Voids
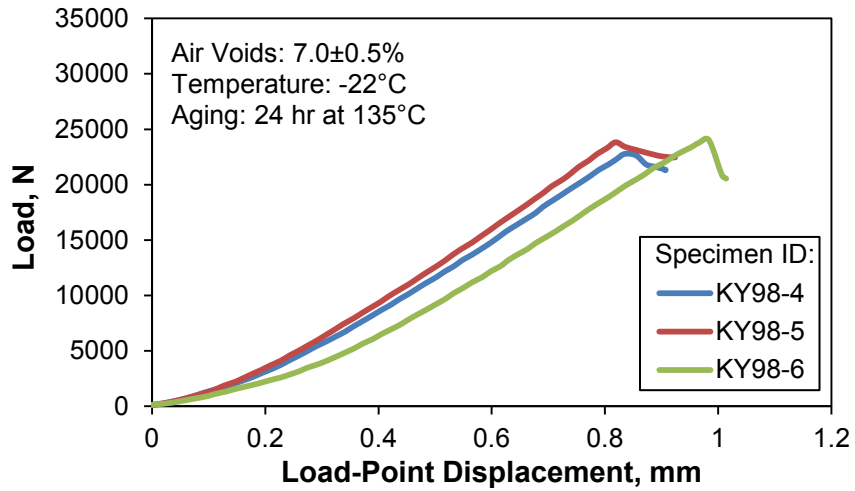
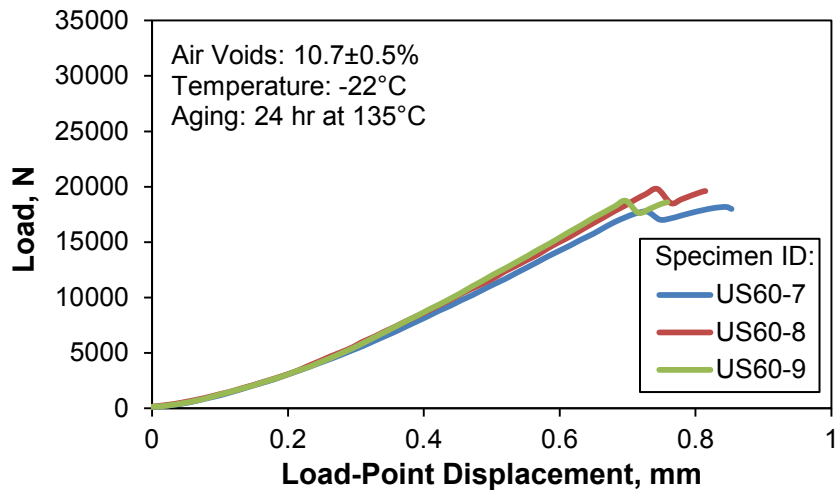**Figure B.8. IRT Fracture Test Data for KY98 Mix with 7.0% Air Voids**
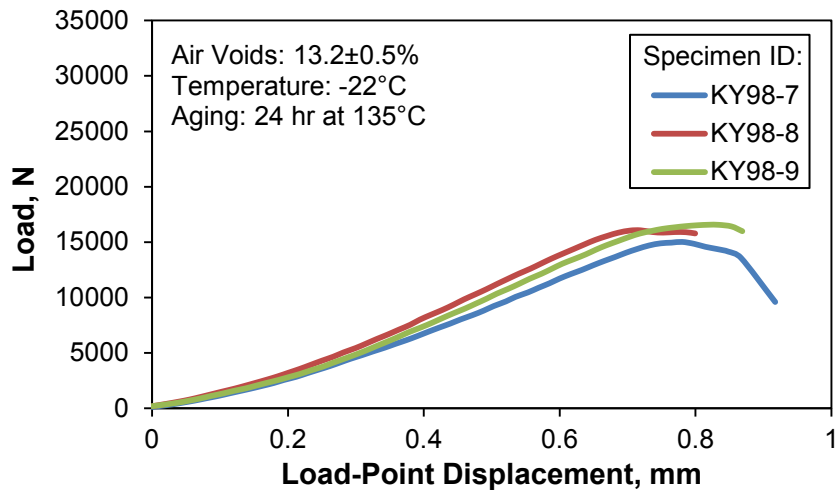
Figure B.9. IRT Fracture Test Data for KY98 Mix with 13.2% Air Voids
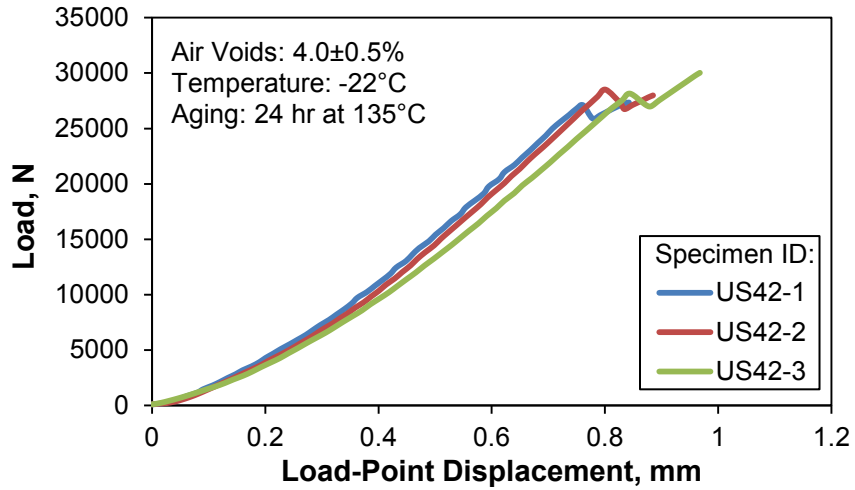
Figure B.10. IRT Fracture Test Data for US42 Mix with 4.0% Air Voids
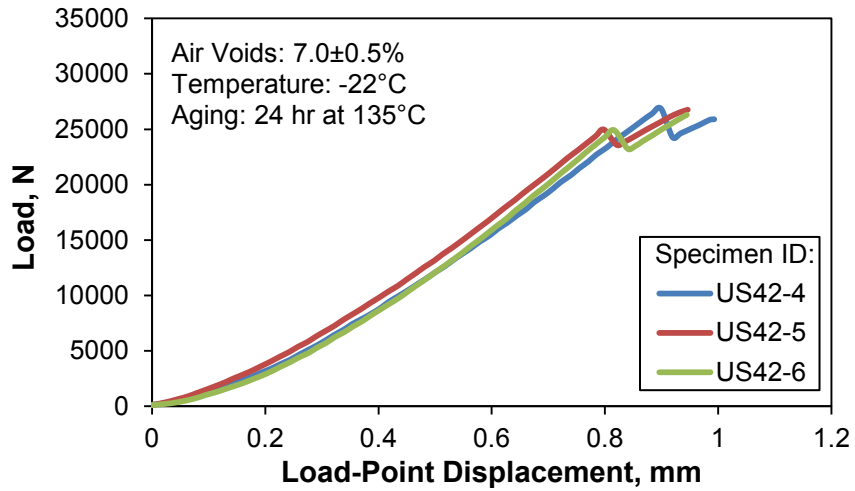
Figure B.11. IRT Fracture Test Data for US42 Mix with 7.0% Air Voids

Figure B.12. IRT Fracture Test Data for US42 Mix with 11.6% Air Voids

Figure B.13. IRT Fracture Test Data for US60 Mix with 4.0% Air Voids

Figure B.14. IRT Fracture Test Data for US60 Mix with 7.0% Air Voids

Figure B.15. IRT Fracture Test Data for US60 Mix with 10.7% Air Voids

APPENDIX C
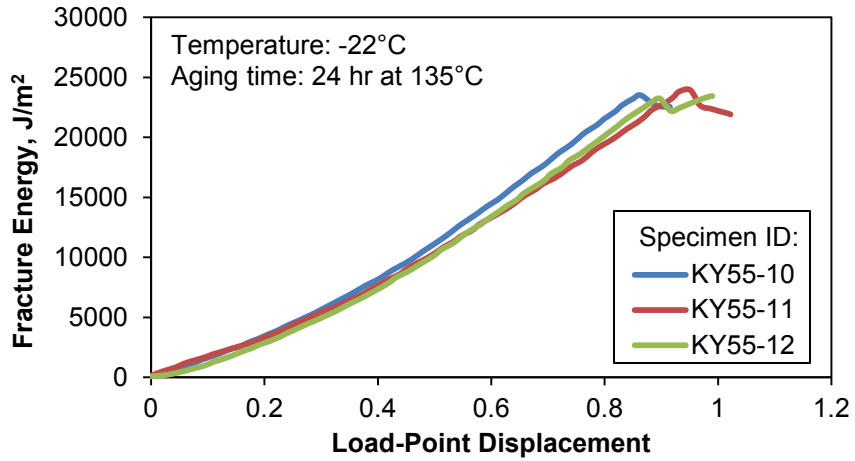# IRT FRACTURE TEST DATA FOR AGING STUDY

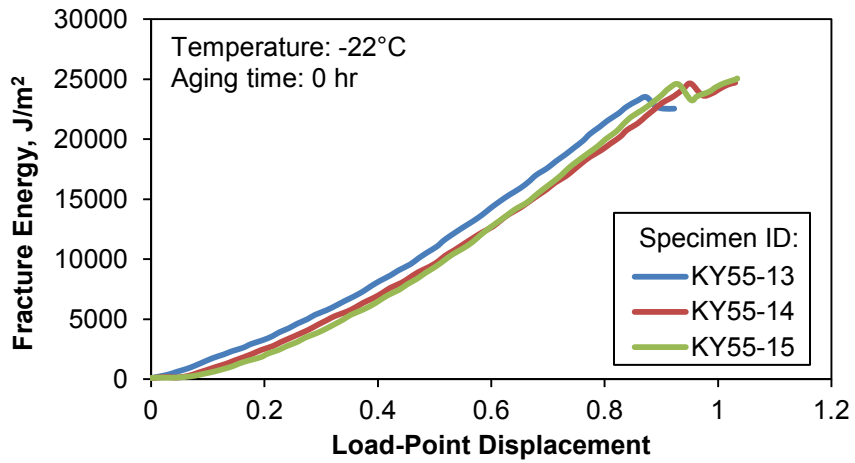**Figure C.1. IRT Fracture Test Data for KY55 at -22°C and after 24-hr Conditioning**

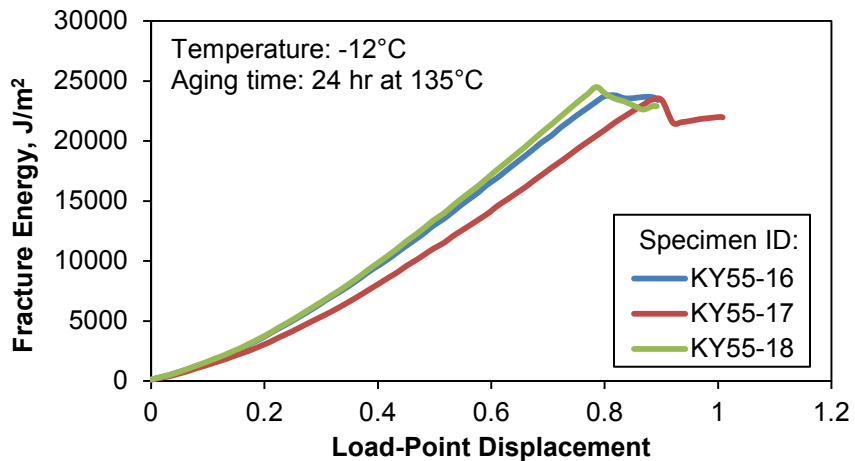**Figure C.2. IRT Fracture Test Data for KY55 at -22°C with No Conditioning**

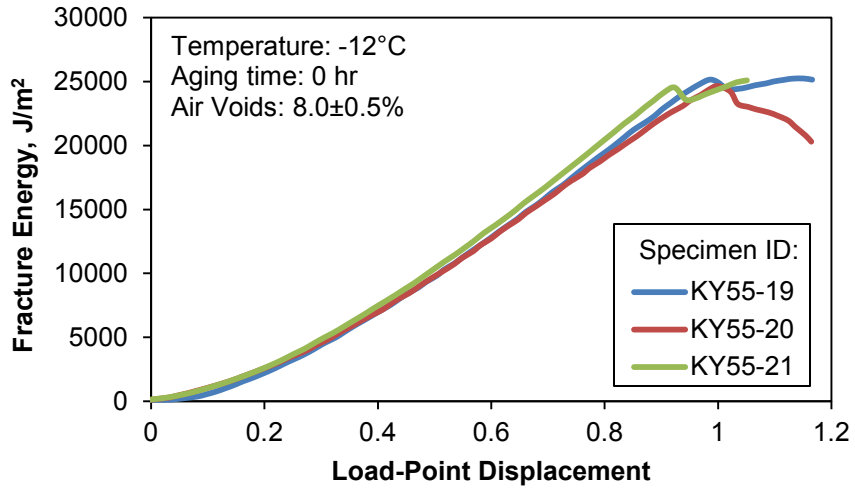**Figure C.3. IRT Fracture Test Data for KY55 at -12°C and after 24-hr Conditioning**

Figure C.4. IRT Fracture Test Data for KY55 at -12°C with No Conditioning

Figure C.5. IRT Fracture Test Data for KY55 at -22°C and after 24-hr Conditioning

Figure C.6. IRT Fracture Test Data for KY55 at -22°C with No Conditioning

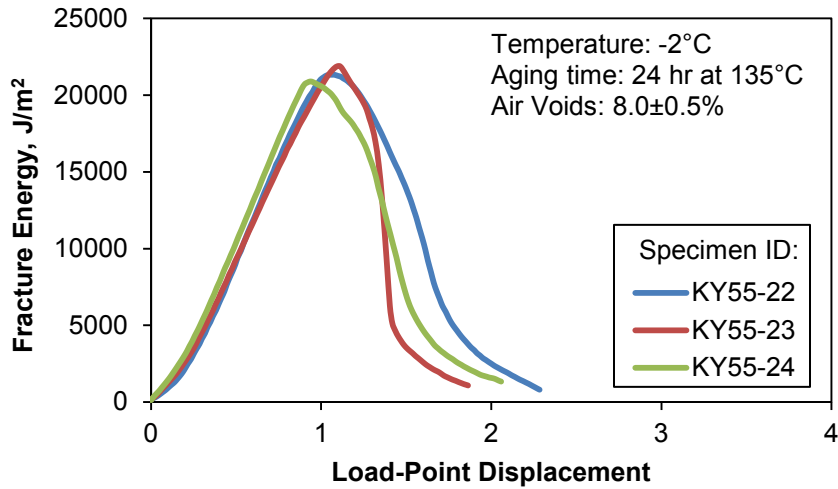**Figure C.7. IRT Fracture Test Data for KY85 at -22°C and after 24-hr Conditioning**

Figure C.8. IRT Fracture Test Data for KY85 at -22°C with No Conditioning

Figure C.9. IRT Fracture Test Data for KY85 at -12°C and after 24-hr Conditioning

Figure C.10. IRT Fracture Test Data for KY85 at -12°C with No Conditioning

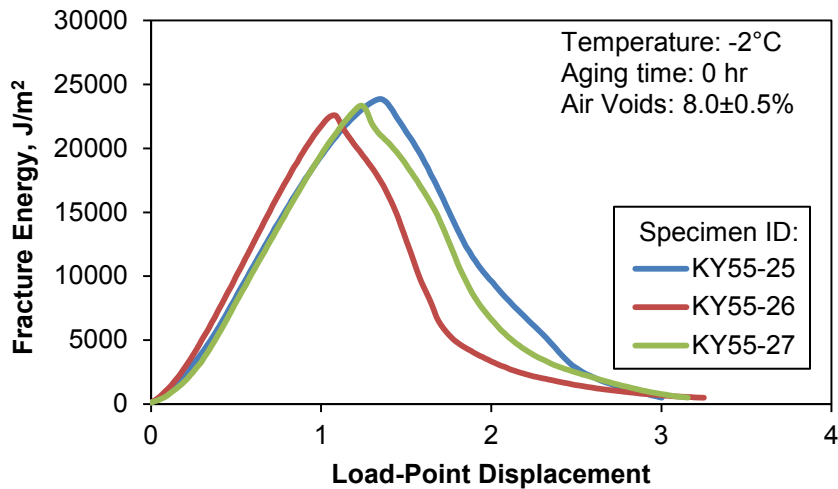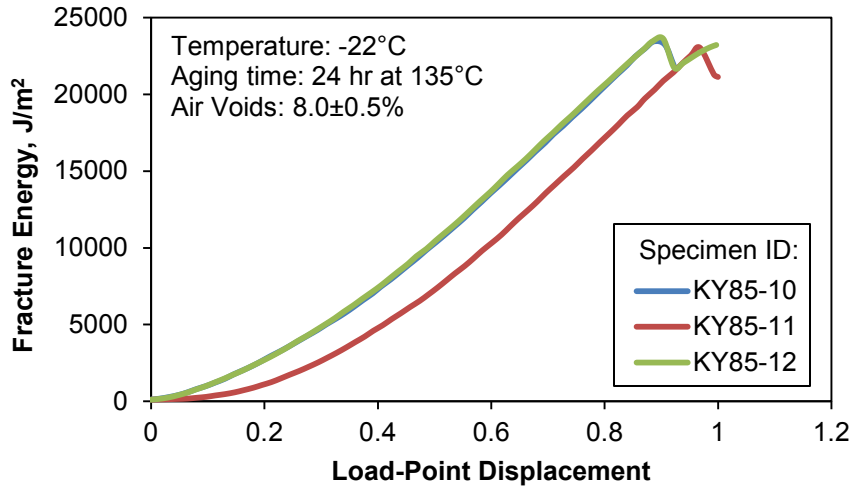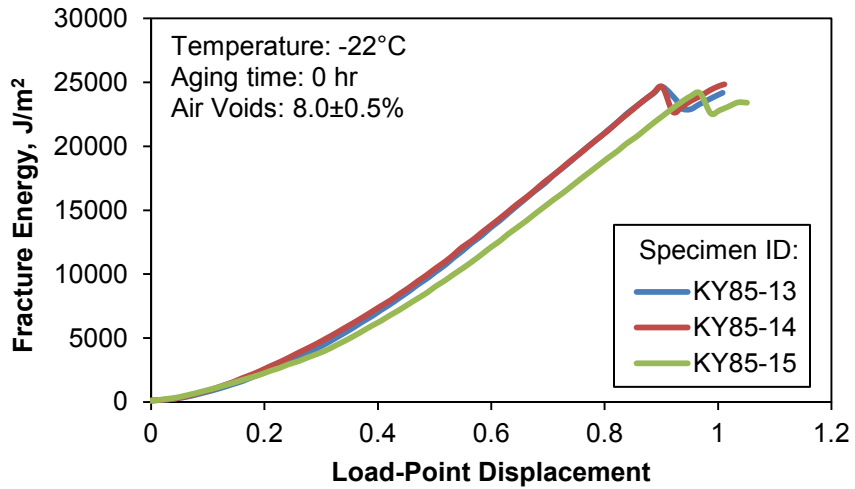**Figure C.11. IRT Fracture Test Data for KY85 at -2°C and after 24-hr Conditioning**

Figure C.12. IRT Fracture Test Data for KY85 at -2°C with No Conditioning

Figure C.13. IRT Fracture Test Data for KY98 at -22°C after 24-hr Conditioning

Figure C.14. IRT Fracture Test Data for KY98 at -22°C with No Conditioning
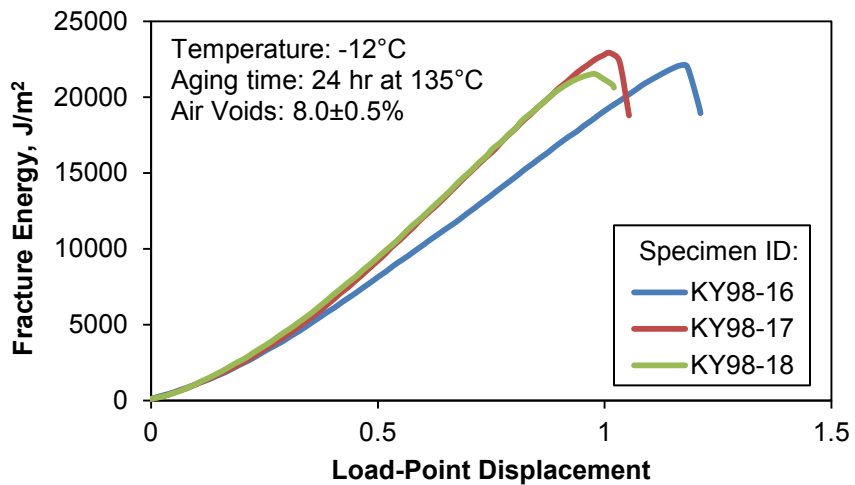
Figure C.15. IRT Fracture Test Data for KY98 at -12°C after 24-hr Conditioning
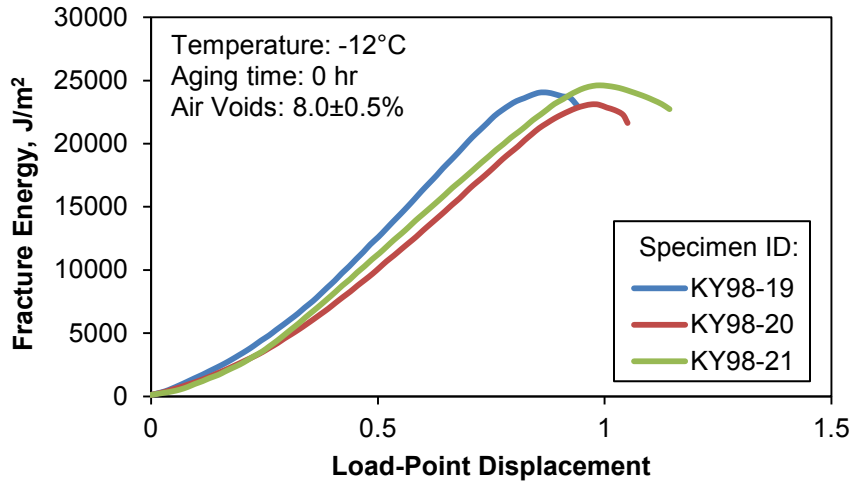
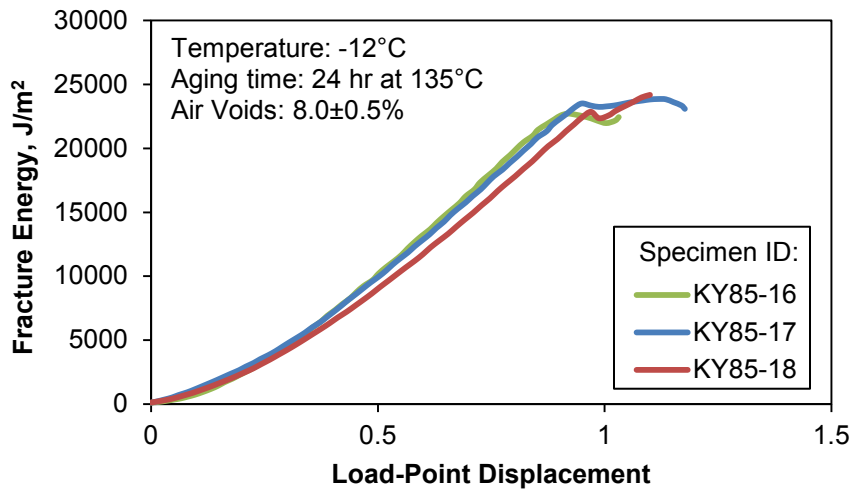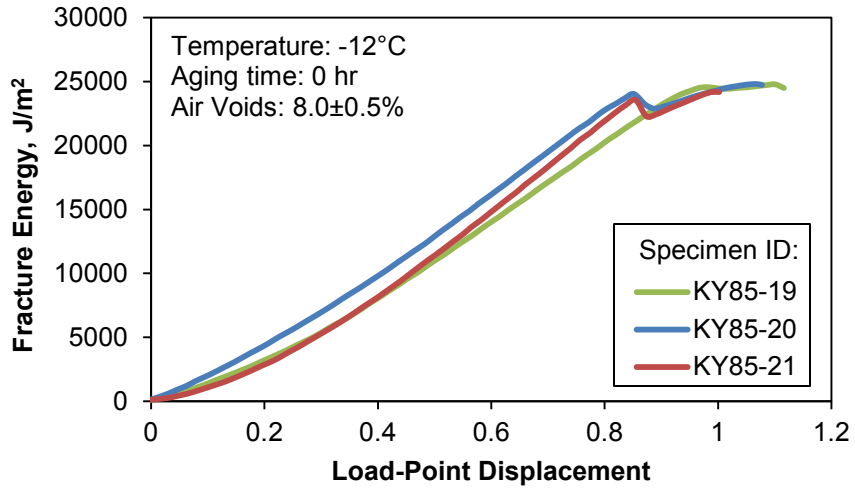**Figure C.16. IRT Fracture Test Data for KY98 at -12°C with No Conditioning**
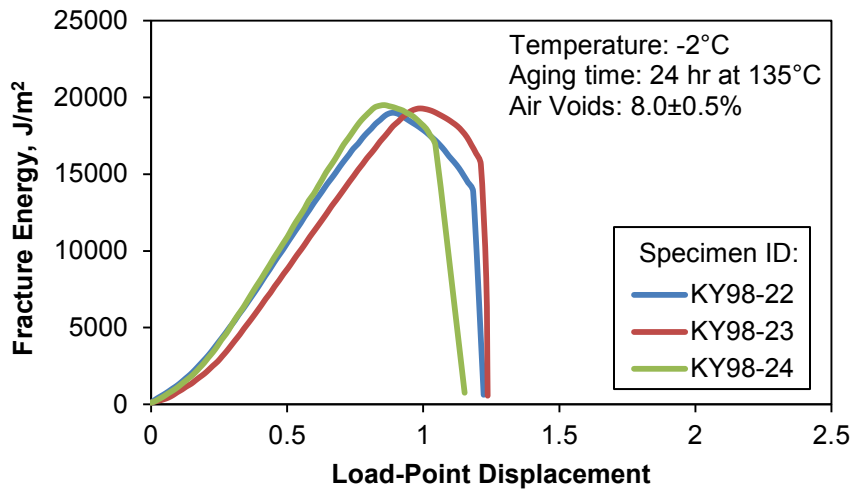
Figure C.17. IRT Fracture Test Data for KY98 at -2°C after 24-hr Conditioning

Figure C.18. IRT Fracture Test Data for KY98 at -2°C with No Conditioning

133

Figure C.19. IRT Fracture Test Data for US42 at -22°C after 24-hr Conditioning

Figure C.20. IRT Fracture Test Data for US42 at -22°C with No Conditioning

Figure C.21. IRT Fracture Test Data for US42 at -12°C after 24-hr Conditioning

Figure C.22. IRT Fracture Test Data for US42 at -12°C with No Conditioning
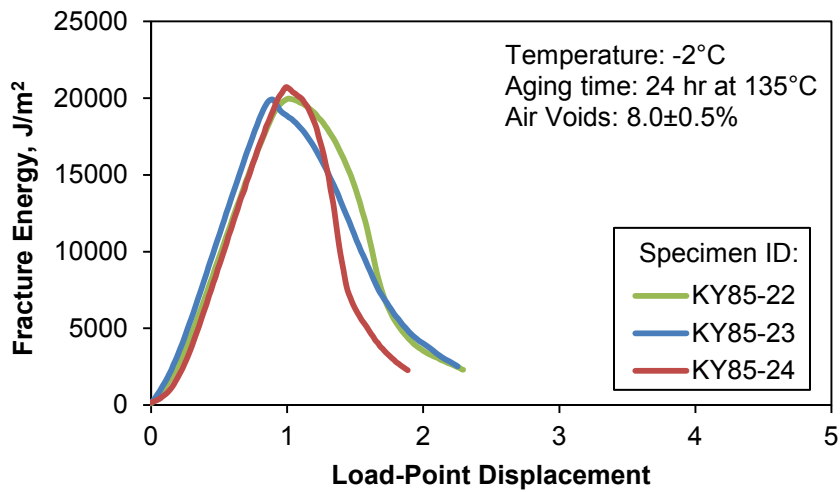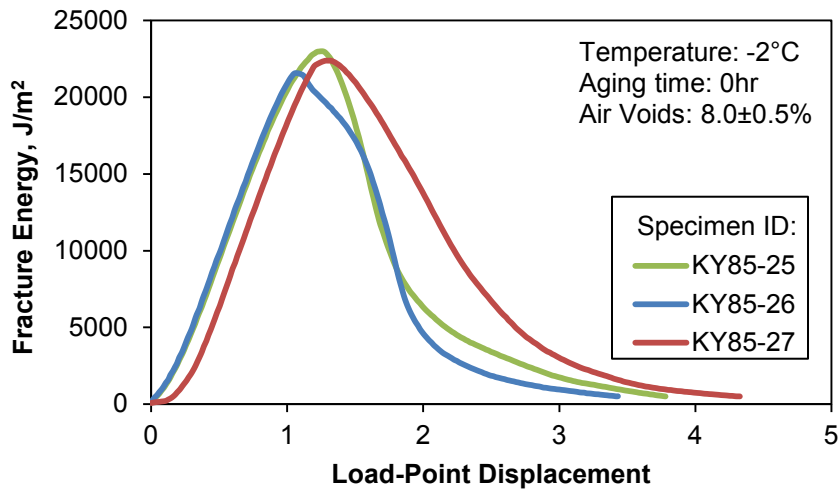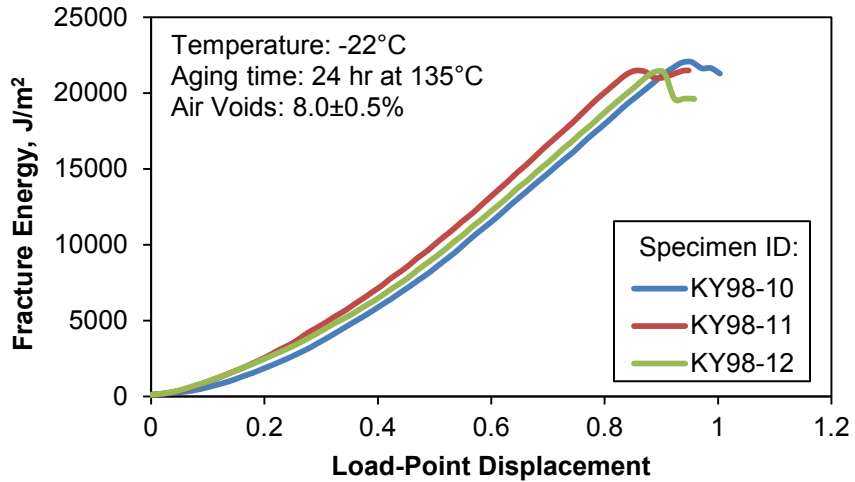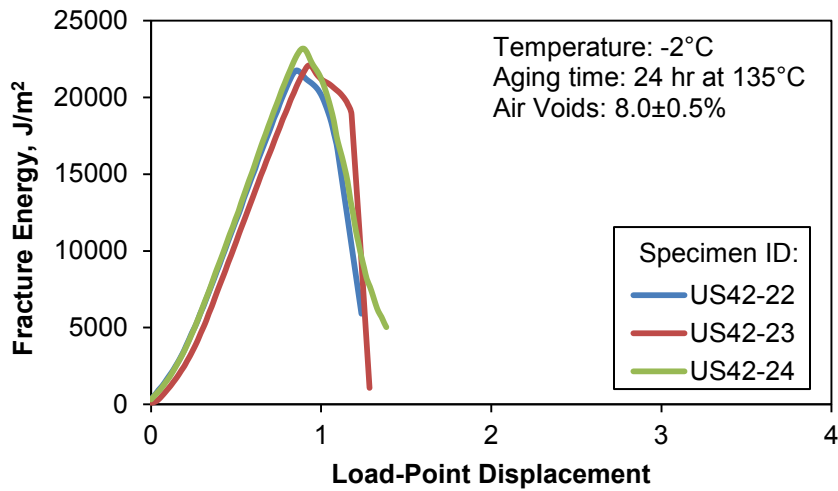

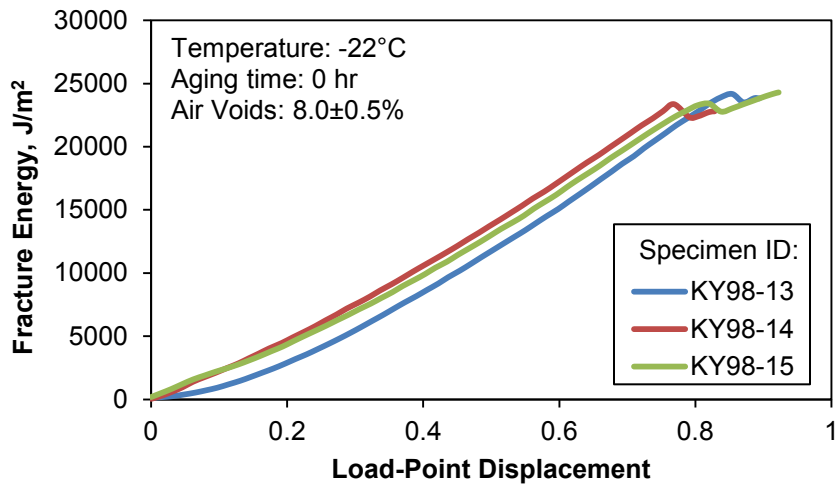**Figure C.23. IRT Fracture Test Data for US42 at -2°C after 24-hr Conditioning**
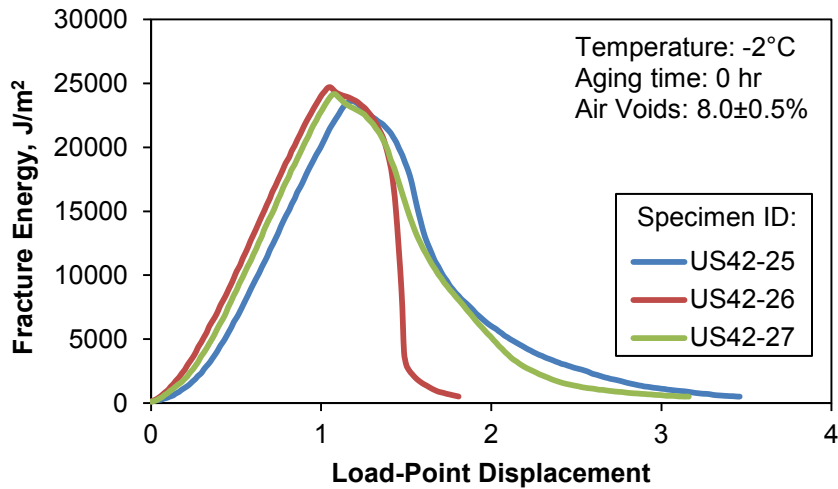
Figure C.24. IRT Fracture Test Data for US42 at -2°C with No Conditioning
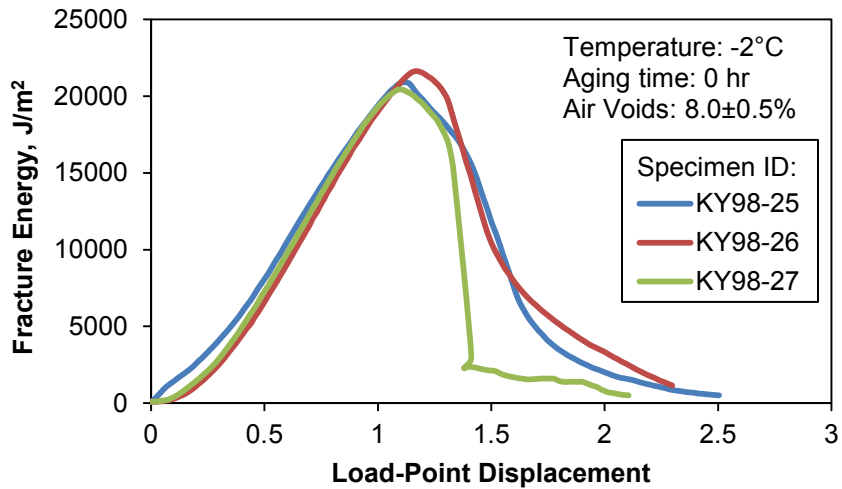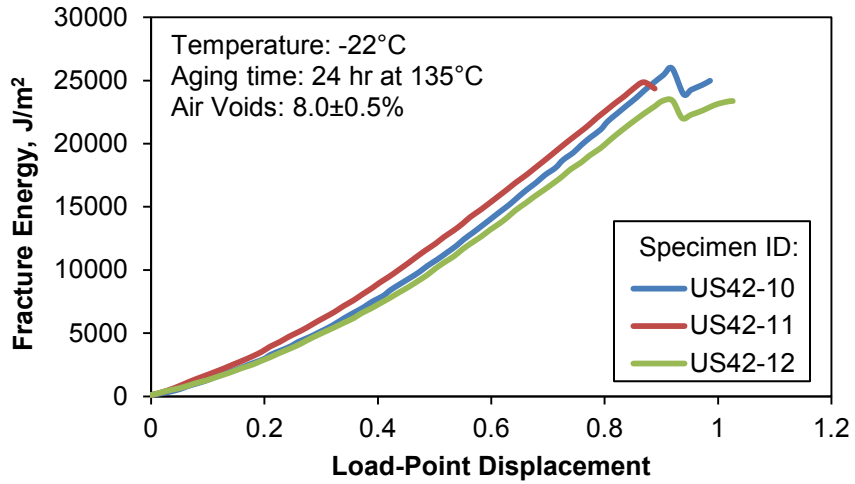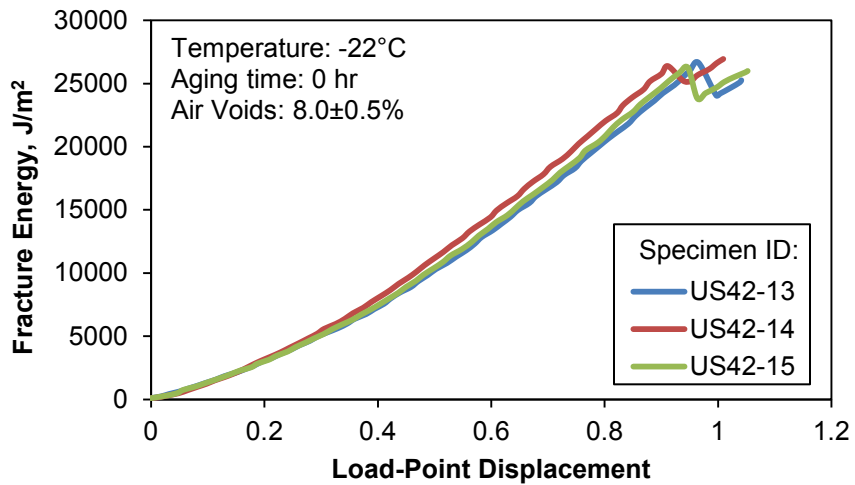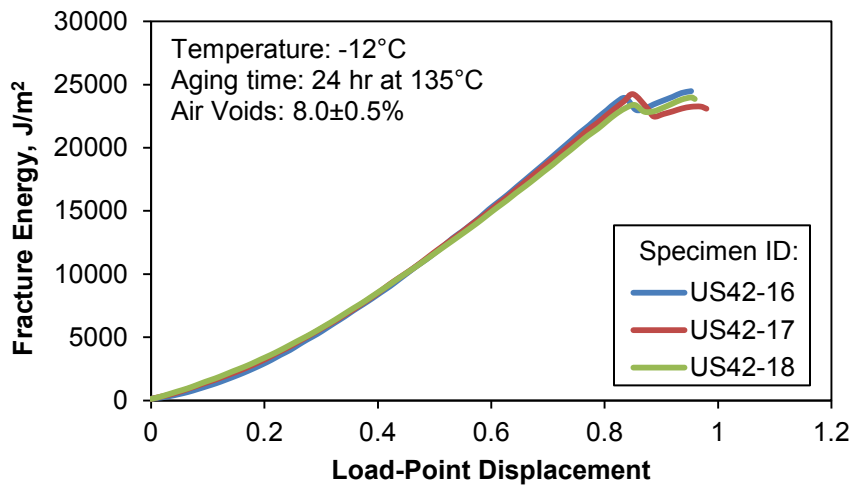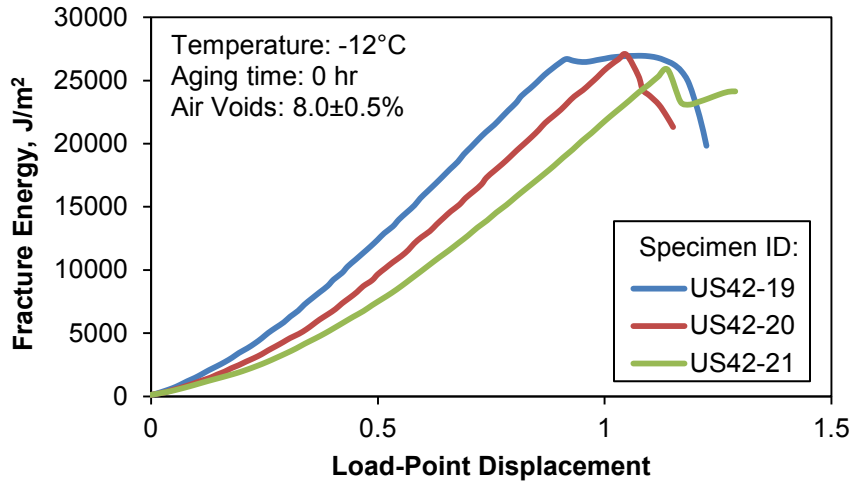
BIBLIOGRAPHY

AASHTO R 30 (2002). "Standard practice for mixture conditioning of hot-mix asphalt (HMA)." American Association of State Highway and Transportation Officials, Washington, DC.

AASHTO T 209 (2011). "Standard method of test for theoretical maximum specific gravity and density of hot-mix asphalt (HMA)." American Association of State Highway and Transportation Officials, Washington, DC.

AASHTO T 322 (2007). "Standard method of test for determining the creep compliance and strength of hot-mix asphalt (HMA) using the indirect tensile test device." American Association of State Highway and Transportation Officials, Washington, DC.

Akhtarhusein, T. T., Deacon, J. A., Coplantz, J. S., Harevy, J. T., Monosmith, C. L., and Finn, F. (1994). *Fatigue Response of Asphalt-Aggregate Mixes*. Publication SHRP-A-404. Strategic Highway Research Program, National Research Council, Washington, D.C.

Anderson, T. L. (1995). *Fracture Mechanics, Fundamentals and Applications,* 2nd Edition. CRC Press, Boca Raton, NY.

ANSYS, Inc. (2009a*), LS-DYNA User's Guide, Release 12.0.* ANSYS, Inc., Canonsburg, PA.

ANSYS, Inc. (2009b), *Element Reference, Release 12.1*. ANSYS, Inc., Canonsburg, PA.

ANSYS, Inc. (2012), *ANSYS Mechanical APDL Contact Technology Guide*. ANSYS, Inc., Canonsburg, PA.

Asphalt Institute (2001). *SuperPave Mix Design, SuperPave Series No.2 (SP-2)*, 3rd Edition, Lexington, KY.

Asphalt Institute (2003). *Performance Graded Asphalt Binder Specification and Testing*, *SuperPave Series No.1 (SP-1)*, 3rd Edition, Lexington, KY.

Asphalt Institute (2007). *The Asphalt Handbook*, 7th Edition, Lexington, KY.

Asphalt Institute (2008). *Asphalt Binder Testing, MS-25*, 2nd Edition, Lexington, KY.

ASTM E399 (2012). "Standard test method for linear-elastic plane-strain fracture toughness K_{IC} of metallic materials." American Society for Testing and Materials, ASTM Book of Standards, Vol. 03.01, Philadelphia, PA.

ASTM D6931 (2012). "Standard test method for indirect tensile (IDT) strength of bituminous mixtures." American Society for Testing and Materials, ASTM Book of Standards, Vol. 04.03, Philadelphia, PA.

ASTM D7313 (2013). "Standard test method for determining fracture energy of asphalt-aggregate mixtures using the disk-shaped compact tension geometry." American Society for Testing and Materials, ASTM Book of Standards, Vol. 04.03, Philadelphia, PA.

Azari, H., and Mohseni, A. (2013). "Effect of short-term conditioning and long-term aging on permanent deformation characteristics of asphalt mixtures." *Journal of the Association of Asphalt Paving Technologists*, 82, 127-149.

Bahgat, A. G., and Herrin, M. (1968). "Brittle fracture of asphalt mixtures." *Journal of the Association of Asphalt Paving Technologists*, 37, 32-50.

Barenblatt G. I. (1962). "The Mathematical theory of equilibrium of cracks in brittle fracture." *Advanced Applied Mechanics*, 7, 55-129.

Barsoum, R. S. (1976). "On the use of isoparametric finite elements in linear fracture mechanics." *International Journal for Numerical Methods in Engineering*, 10(1), 25-37.

Bell, C. A., AbWahab, Y., Cristi, M. E., and Sosnovske, D. (1994). *Selection of Laboratory Aging Procedures for Asphalt-Aggregate Mixtures*. Publication (SHRP-A-383), Strategic Highway Research Program, Washington, D.C.

Bhurke, A. S., Shin, E. E., and Drzal, L. T. (1997). "Fracture morphology and fracture toughness measurement of polymer-modified asphalt concrete", *Transportation Research Record*, 1590, 23-33.

Birgisson, B., Roque, R., Sangpetngam, B., and Zhang, Z. (2002). "Hot mix asphalt fracture mechanics: a fundamental crack growth law for asphalt mixtures." *Journal of the Association of Asphalt Paving Technologists*, 71, 816-827.

Blankenship, P., and Anderson, R. M. (2010). "Laboratory investigation of HMA modulus, flow number and flexural fatigue on samples of varying density." *Journal of the Association of Asphalt Paving Technologists*, 79, 497-515.

Blankenship, P., Anderson, R. M., King, G. N., and Hanson, D. I. (2010). "A laboratory and field investigation to develop test procedures for predicting non-load associated cracking of airfield HMA pavements." *AAPTP Project 06-01 Report*, Airfield Asphalt Pavement Technology Program.

Bonesteel, R. M., Piper, D. E., and Davinroy, A. T. (1978). "Compliance and KI calibration of double cantilever beams (DCB) specimens." *Engineering Fracture Mechanics*, 10(2), 425-428.

Braham, A. F., Buttlar, W. G., Clyne, T. R., Marasteanu, M. O., and Turos, M. I. (2009). "The effect of long-term laboratory aging on asphalt concrete fracture energy." *Journal of the Association of Asphalt Paving Technologists*, 78, 417-454.

Braham, A., Zofka, A., and Li, X. (2012). "Exploring the reduction of laboratory testing for the cohesive zone model for asphalt concrete." *International Journal of Pavement Engineering*, 13(4), 350-359.y

Branthaver, J. F., Peterson, J. C., Robertson, R. E., Duvall, J. J., Kim, S. S., Harnsberger, P. M., Mill, T., Ensley, E. K., Barbour, F. A., and Schabron, J. F. (1993). *Binder Characterization and Evaluation, Volume 2: Chemistry*. SHRP-A-368, Strategic Highway Research Program, Washington, D.C.

Brown, W. F. and Srawly, J. E. (1966). *K Calibration of Specimens*. ASTM STP 410, American Society for Testing and Materials, Philadelphia, PA.

Clements, T. M., Blankenship, P. B., and Mahboub, K. C. (2012). "The effect of loose mix aging on the performance of warm mix asphalt." *Journal of the Association of Asphalt Paving Technologists*, 81, 541-566.

Charpa, S. C., and Canale, R. P. (2009). *Numerical Methods for Engineers, 6th Edition*. McGraw Hill Science, New York, NY.

Chong, K. P., and Kuruppu, M. D. (1984). "New specimen for fracture toughness determination for rock and other materials." *International Journal of Fracture*, 26, 59-62.

Christensen, R. M. (1986). *Theory of Viscoelasticiy: An Introduction*. Academic Press Inc., New York, NY.

Christensen, D. W., and Anderson, D. (1992). "Interpretation of dynamic mechanical test data for paving grade asphalt cements." *Journal of the Association of Asphalt Paving Technologists*, 61, 67-98.

Christensen, D. (1998). "Analysis of creep data from indirect tension test on asphalt concrete." *Journal of the Association of Asphalt Paving Technologists*, 66, 458-489.

Dally, J. W., and Sanford R. J. (1987). "Strain gauge methods for measuring the opening mode stress intensity factor." Experimental Mechanics, 27, 381-388.

Dave, E. V., Paulino, G. H., and Buttlar, W. G. (2010). "Asphalt pavement aging and temperature dependent properties through a functionally graded viscoelastic model, Part-I: Development, implementation and verification." Materials Science Forum, 631, 47-52.

Dong S., Wang Y., and Xia Y. (2004). "Stress intensity factors for central cracked circular disk subjected to compression." *Engineering Fracture Mechanics*, 71, 1135-1148.

Dugdale D.S. (1960) "Yielding of steel sheets containing slits." *Journal of Mechanics and Physics of Solids*, 8, 100-108.

Fett T. (2001). "Stress intensity factors and T-stress for internally cracked circular disks under various boundary conditions." *Engineering Fracture Mechanics*, 68, 1119-1136.

Fischer, M. P., Elsworth, D., Alley, R. B., and Engelder, T. (1996). "Finite element analysis of the modified ring test for determining mode I fracture toughness." *International Journal of Rock Mechanics, Mining Science, and Geomechanics*, 33(1), 1-15.

Frocht, M. M. (1964). *Photoelasticity*. John Wiley & Sons, New York, NY.

Gross, D., and Seelig, T. (2006). Fracture Mechanics with an Introduction to Micromechanics. Springer, New York City, NY.

Gubler, R., Partl, M. N., Canestrari, F., and Grilli, A. (2005). "Influence of water and temperature on mechanical properties of selected asphalt pavements." *Materials and Structures*, 38(279), 523-532.

Harison, J. A., Hardin, B. O., and Mahboub, K. (1994). "Fracture toughness of compacted cohesive soils using the ring test.", *ASCE Journal of Geotechnical Engineering*, 120(5), 872-891.

Harvey, J. T., and Tsai B. W. (1996). "Effect of asphalt content and air void content on mix fatigue and stiffness." *Transportation Research Record*, 1543, 38-45.

Henshell, R. D., and Shaw, K. G. (1975). "Crack tip finite elements are unnecessary." *International Journal for Numerical Methods in Engineering*, 9(3), 495-507.

Hertzberg, R. W. (1996). *Deformation and Fracture Mechanics of Engineering Materials*, 4th Edition. John Wiley and Sons, Inc., New York, NY.

Hillerborg A. (1985). "The theoretical basis of a method to determine the fracture energy GF of concrete", *Material and Structures*, 18(4), 291-296.

Hillerborg, A., Modeer, M., and Peterson, P. E. (1976). "Analysis of crack formation and crack growth in concrete by means of fracture mechanics and finite element." *Cement and Concrete Research*, 6, 773-782.

Hiltunen, D. R., and Roque, R. (1996). "Mechanics-based prediction model for thermal cracking of asphalt concrete pavements." *Journal of the Association of Asphalt Paving Technologists*, 63, 81-106.

Hou, T., Underwood, B. S., and Kim, Y. R. (2010). "Fatigue performance prediction of north Carolina mixtures using the simplified viscoelastic continuum damage model." *Journal of the Association of the Asphalt Paving Technologists*, 79, 35-73.

Huang, Y. H. (2004). *Pavement Analysis and Design*, 2nd Edition, Pearson Prentice Hall, Upper Saddle River, NJ.

Hyde, T. H., and Warrior, N. A. (1990). "Improved method for determination of photoelastic stress intensity factors using the Westergaard stress function." *International Journal of Mechanical Sciences*, 32(3), 265-273.

Hyunwook, K., Wagoner, M. P., and Buttlar, W. G. (2008). "Simulation of fracture behavior in asphalt concrete using a heterogeneous cohesive zone discrete element model." *Journal of Materials in Civil Engineering*, 20(8), 552-563.

Jia, Z., Castro-Montero, A., and Shah, S. P. (1996). "Observation of mixed mode fracture with center notched disk specimen." *Cement and Concrete Research*, 26(1), 125-137.

Kim, M., Mohammad, L., and Elseifi, M. (2012). "Characterization of fracture properties of asphalt mixtures as measured by semicircular bend test and indirect tension test." *Transportation Research Record*, 2296, 115-124.

Kim, Y. R., Lee, S. J., Seo, Y., and El-Haggan, O. (2008). "Determination of price reduction factors for density-deficient asphalt pavements." *Journal of Testing and Evaluation*, 36(4), 335-344.

Larson G., and Dempsey B. J. (1997). *Enhanced Integrated Climatic Model: Version 2.0*, DTFA MN/DOT Report No. 72114, Minnesota Road Research Project and Federal Highway Administration, Minneapolis, MN.

Li, X. and Marasteanu, M. (2004). "Evaluation of the low temperature fracture resistance of asphalt mixtures using the semi-circular bend test." *Journal of the Association of Asphalt Paving Technologists*, 73, 401-426.

Li, X., Marasteanu, M. O., Dai, S., and Lukanen, E. (2005). "Prediction of low temperature crack spacing in asphalt pavements", *Proceedings of the 7th International Conference on the Bearing Capacity of Roads, Railways and Airfields*, Trondheim, Norway.

Lim, I. L., Johnston, I. W., Choi, S. K., and Boland, J. N. (1994). "Fracture testing of a soft rock with semi-circular specimens under three point bending. part1-mode I." *International Journal of Rock Mechanics*, Mining Science 31, 199-212.

Little D. N., and Mahboub K. (1985). "Engineering properties of first generation plasticized sulfur binders and low temperature fracture evaluation of plasticized sulfur paving mixtures." *Transportation Research Record*, 1034, 103-111.

Lytton, R. L., Pufhal, D. E., Michalak, C. H., Liang, H. S., and Dempsey, B. J. (1990). *An Integrated Model of the Climatic Effects on Pavements*. FHWA Report No. RD-90-033, Federal Highway Administration, Washingont, D.C.

Mahboub, K. (1990). "Elasto-plastic fracture characterization of paving materials at low temperatures*." Journal of Testing and Evaluation*, 18(3), 210-218.

Majidzadeh, K., Kauffmann, E. M., and Ramsamooj, D. V. (1971). "Application of fracture mechanics in the analysis of pavement fatigue." *Journal of the Association of Asphalt Paving Technologists*, 40, 227-246.

Marasteanu, M. O., Labuz, J. E., Dai, S., and Li, X. (2002). "Determining the low-temperature fracture toughness of asphalt mixtures", Transportation Research Record, 1789, 191-199.

Mirza, M. W., and Witczak, W. M. (1996). "Development of a global aging system for short term and long term aging of asphalt cements." *Journal of the Association of Asphalt Paving Technologists*, 64, 393-430.

Mobasher, B. M., Mamlouk, M. S., and Lin, H. M. (1997). "Evaluation of crack propagation properties of asphalt mixtures." *Journal of Transportation Engineering*, 123(5), 405-413.

Mogawer, W. S., Austerman, A. J., Kaseem, E., and Masad, E. (2011). "Moisture damage characteristics of warm mix asphalt mixtures." *Journal of the Association of Asphalt Paving Technologists*, 80, 491-524.

Mogawer, W. S., Austerman, A. J., Mohammad, L., and Emin, K. M. (2013). "Evaluation of high RAP-WMA asphalt rubber mixtures." *Journal of the Association of Asphalt Paving Technologists*, 82, 253-287.

Mohammad, L., Elseifi, M., Cooper, S., Challa, H., and Naidoo, P. (2013). "Laboratory evaluation of asphalt mixtures that contain biobinder technologies." *Transportation Research Record*, 2371, 58-65.

Molenaar, J. M. M., and Molenaar, A. A. A. (2000). "Fracture toughness of asphalt in the semi-circular bend test." *Proceedings of 2nd Eurasphalt and Eurobitume Congress, Barcelona*, Spain, 509-517.

Mull, M. A., Stuart, K., and Yehia, A. (2002). "Fracture resistance characterization of chemically modified crumb rubber asphalt pavement." *Journal of Materials Science*, 37, 557-566

Newman Jr., J. C. (1981). "Stress intensity factor and crack opening displacements for round compact specimens." *International Journal of Fracture*, 17(6), 567-578.

Paris P. C., and Sih G. C. (1965). "Stress analysis of cracks." *Fracture Toughness Testing and its Application*, ASTM STP 381, American Society for Testing and Materials, Philadelphia, PA.

Pellinen T. K., Xiao S., Carpenter S., Eyad M., Di Benedetto H., and Roque, R. (2005). "Relationship between triaxial shear strength and indirect tensile strength of hot mix asphalt", *Journal of the Association of the Asphalt Paving Technologists*, 74, 347-379.

Reddy, J.N. (2006). *An Introduction to the Finite Element Method*. McGraw-Hill, New York.

Roque, R., and Buttlar, W. G. (1992). "The development of a measurement and analysis system to accurately determine asphalt concrete properties using the indirect tensile mode." *Journal of the Association of Asphalt Paving Technologists*, 61, 304-328.

Rowe, G. M., Sharrock, M. J., Bouldin, M. G., and Dongre, R. N. (2001). "Advanced techniques to develop asphalt master curves from the bending beam rheometer." *Petroleum and Coal*, 43(1), 54-59.

Rowe, G. M., and Sharrock, M. J. (2011). "Alternate shift factor relationship for describing temperature dependency of viscoelastic behavior of asphalt materials." *Transportation Research Record*, 2207, 125-135.

Sangpetngam, B., Bjorn, B., and Roque, R. (2003). "Development of efficient crack growth simulator based on hot-mix asphalt fracture mechanics." *Transportation Research Record*, 1832, 115-112.

Song, S. H., Paulino, G. H., and Buttlar, W. G. (2006). "A bilinear cohesive zone model tailored for fracture of asphalt concrete considering viscoelastic bulk material." Engineering Fracture Mechanics, 73(18), 2829-2848.

Spiegel, M. R. (1992). Schaum's Outline of Theory and Problems of Laplace Transforms, McGraw Hill, Inc., New York, NY.

Voitovich, L. V., Malezhik, M. P., and Chernyshenko, I. S. (2011). "Stress state around cracks on the boundary of a hole in a photoelastic orthotropic plate under creep." *International Applied Mechanics*, 46(11), 1268-1274.

Wagoner, M. P., Buttlar, W. G., Paulino, G. H. (2005a). "Development of a single-edge notched beam test for asphalt concrete mixtures." *Journal of Testing and Evaluation*, 33(6), 452-460.

Wagoner, M. P., Buttlar, W. G., and Paulino, G. H. (2005b). "Disk-shaped compact tension test for asphalt concrete fracture." *Experimental Mechanics*, 45(3), 270-277.

Wagoner, M. P., Buttlar, W. G., Paulino, G. H., and Blankenship, P. (2005c). "Investigation of the fracture resistance of hot-mix asphalt concrete using a disk-shaped compact tension test." *Transportation Research Record*, 1929, 183-192.

Wagoner, M. P., Buttlar, W. G., Paulino, G. H., Blankenship, P., Roque, R., Rongzong, W., De Bondt, A., Molenaar, A., Scarpas, T., Birgisson, B., Smith, L., and Gibson, N. (2006). "Laboratory testing suite for characterization of asphalt concrete mixtures obtained from field cores." *Journal of the Association of Asphalt Paving Technologists*, 75, 815-852.

Witczak, M. W., Kaloush, K., Pellinen, T., El-Basyouny, M., and Van Quintus, H. (2002). *Simple Performance Test for Superpave Mix Design*, NCHRP Report 465, National Cooperative Highway Research Program, Washington, D.C.

Wu, Z., Mohammad, L. N., Wang, L. B., and Mull, M. A. (2005). "Fracture resistance characterization of Superpave mixtures using the semi-circular bending test." *Journal of ASTM International*, 2(3), 1-15.

Xu, Q., Chen, H., and Prozzi, J. A. (2010). "Performance of fiber reinforced asphalt concrete under environmental temperature and water effects." *Construction and Building Materials*, 24(10), 2003-2010.

Yang, S., Tang, T., Zollinger, D. G., and Gurjar, A., (1997). "Splitting tension tests to determine concrete fracture parameters by peak-load method." *Advanced Cement Based Materials*, 5(1), 18-28.

Zapata, C. E., and Houston, W. N. (2008). *Calibration and Validation of the Enhanced Integrated Climatic Model for Pavement Design*. NCHRP Report 602, Transportation Research Board of the National Academies, Washington, D.C.

Zeinali, A., Blankenship, P. B., and Mahboub, K. C. (2014). "Evaluation of the effect of density on asphalt pavement durability through performance testing." Presented at the 93rd annual meeting of the Transportation Research Board of the National Academies, Washington, DC.

Zhang, Z., Roque, R., Birgisson, B., and Sangpetngam, B. (2001). "Identification and verification of a suitable crack growth law." *Journal of the Association of Asphalt Paving Technologists*, 70, 206–241.

Zienkiewicz, O.C. (1977). *The Finite Element Method*, McGraw-Hill, London.

Zou, J., Roque, R., Chun, S., and Lopp, G. (2013). "Long-term field evaluation and analysis of top-down cracking for Superpave projects." *Road Materials and Pavement Design*, 14(4), 831-846

VITA

Author	Alireza Zeinali		

Education	2008-2011	University of Kentucky	Lexington, KY

Graduate Certificate in Applied Statistics

2012	Asphalt Institute Academy	Lexington, KY

Professional Certificate for Hot Mix Asphalt Mix Design Technology

2002-2005	University of Tehran	Tehran, Iran

M.Sc. Highway and Transportation Engineering

1997-2002	University of Tehran	Tehran, Iran

B.Sc. Civil Engineering

Professional Experience	2014	InstroTek, Inc.	Raleigh, NC

Director of Field Services

2011-2014	Asphalt Institute	Lexington, KY

Graduate Research Engineer

2008- 2014	University of Kentucky	Lexington, KY

Research Associate

2010		Lexington, KY

Engineer in Training Certificate (State of Kentucky)

2009- 2014	University of Kentucky	Lexington, KY

Teaching Assistant

2004-2005	Soil Mechanics Lab	Tehran, Iran

Academic Research Associate

Patent	Southgate H. F., Mahboub K. C., Zeinali A., Load Transfer Assembly (A New Load Transfer System for the Concrete Pavement Joints), U.S. Patent 08206059 Cl. 404-60, Filed September 14, 2011, and issued June 26, 2012.

Honors	▪ David R. Jones, IV, PhD Scholarship Award, Association of Modified Asphalt Producers (AMAP): 2013
	▪ Layman T. Johnson Fellowship Award: 2012
	▪ Ellis G. Williams Award for Asphalt Research: 2012
	▪ Kentucky Opportunity Fellowship: 2010 and 2011
	▪ College of Engineering Scholarship: 2008- 2014
	▪ Chi Epsilon (The Civil Engineering Honor Society)
Society Memberships	▪ Chi Epsilon, University of Kentucky Chapter: Treasurer 2009-2013
	▪ Student Member of the American Society of Civil Engineers (ASCE)
	▪ Transportation Research Board (TRB) Student Affiliate
Peer-Reviewed Journal Publications	▪ Zeinali A., Mahboub K. C., Blankenship P. B., "Development of the Indirect Ring Tension Fracture Test for Hot Mix Asphalt." Accepted for publication in the AAPT Journal, Association of Asphalt Paving Technologists, V. 83, 2014, jointly to be published with the Road Materials and Pavement Deign (RMPD) Journal, 2014.
	▪ Zeinali A., Blankenship P. B., Mahboub K. C., "Effect of Long-Term Ambient Storage of Compacted Asphalt Mixtures on Laboratory-Measured Dynamic Modulus and Flow Number." Accepted for publication in Transportation Research Record: Journal of the Transportation Research Board (TRB), 2014.
	▪ Zeinali A., Blankenship P. B., Mahboub K. C., "Effect of Laboratory Mixing and Compaction Temperatures on Asphalt Mixture Volumetrics and Dynamic Modulus." Accepted for publication in Transportation Research Record: Journal of the Transportation Research Board (TRB), 2014.
	▪ Zeinali A., Blankenship P. B., Anderson R. M., Mahboub K. C., "Laboratory Investigation of Asphalt Pavements with Low Density and Recommendations to Prevent Density Deficiency." Advanced Materials Research, Vol. 723, 2013, pp. 128-135.
	▪ Zeinali A., Mahboub K. C., Southgate H. F., "Effects of Hinged Dowel System on Performance of Concrete Pavement Joints." International Journal of Pavement Research and Technology, Vol. 6, No. 4, 2013, pp. 243-249.
	▪ Zeinali A., M.Sc. Thesis: Measurement of Track Reaction During Train Passage on Railway Curves, University of Tehran, 2005.

Peer-Reviewed Conferences and Invited Presentations

- Zeinali A., Blankenship P. B., Mahboub K. C., "Evaluation of the Effect of Density on Asphalt Pavement Durability through Performance Testing." Presented at the 93rd Annual Meeting of the Transportation Research Board (TRB), Washington, D.C., 2014.

- Zeinali A., Blankenship P. B., Mahboub K. C., "Effect of Long-Term Ambient Storage of Compacted Asphalt Mixtures on Laboratory-Measured Dynamic Modulus and Flow Number." Presented at the 93rd Annual Meeting of the Transportation Research Board (TRB), Washington, D.C., 2014.

- Zeinali A., Blankenship P. B., Mahboub K. C., "Effect of Laboratory Mixing and Compaction Temperatures on Asphalt Mixture Volumetrics and Dynamic Modulus." Presented at the 93rd Annual Meeting of the Transportation Research Board (TRB), Washington, D.C., 2014.

- Zeinali A., Blankenship P. B. (presenter), "Temperature Evaluation of the Forced-Draft Ovens for Conditioning of Loose Asphalt Mix Samples." Committee Presentation at the 93rd Annual Meeting of the Transportation Research Board (TRB), AFK50 Committee, Washington, D.C., 2014.

- Zeinali A., Mahboub K. C., Blankenship P. B., "Development of the Indirect Ring Tension Fracture Test for Hot Mix Asphalt." Presented at the 89th AAPT Annual Meeting, Association of Asphalt Paving Technologists, Atlanta, GA, 2014.

- Zeinali A., Blankenship P. B., Mahboub K. C., "Comparison of Performance Properties of Terminal Blend Tire Rubber and Polymer Modified Asphalt Mixtures." Presented and published in the proceedings of 2nd Transportation and Development Institute (T&DI) Congress, American Society of Civil Engineers, Orlando, Florida, 2014.

- Zeinali A., Mahboub K. C., Blankenship P. B., "Fracture Characterization of Hot-Mix Asphalt by Indirect Ring Tension Test." Presented and published in the proceedings of the 3rd International Conference on Transportation Infrastructure (ICTI), Pisa, Italy, 2014.

- Zeinali A., Blankenship P. B., Mahboub K. C., "Quantifying the Pavement Preservation Value of Chip Seals." Presented and published in the proceedings of the 12th International Society for Asphalt Pavements (ISAP) Conference, Raleigh, North Carolina, 2014.

- Zeinali A., Blankenship P. B., Mahboub K. C., "Laboratory Performance Evaluation of RAP/RAS Mixtures Designed with Virgin and Blended Binders." Presented and published in the proceedings of the 12th International Society for Asphalt Pavements (ISAP) Conference, Raleigh, North Carolina, 2014.

- Zeinali A., Mahboub K. C., Southgate H. F., "Application of the Hinged Dowel System for Increasing the Durability of Concrete Pavement Joints." Presented and published in the proceedings of The Airfield and Highway Pavement Conference, The Transportation and Development Institute (T&DI) of the American Society of Civil Engineers (ASCE), Los Angeles, CA, 2013.

- Zeinali A., Blankenship P. B., Anderson R. M., Mahboub K. C., "Investigating the Current Practice of Employing the Reclaimed Asphalt Pavement and Shingles in New Pavements." Committee Presentation at the 92nd Annual Meeting of the Transportation Research Board (TRB), AFK30 Committee, Washington, D.C., 2013.

- Zeinali A., Mahboub K. C., Southgate H. F., "A New Load Transfer Assembly for the Jointed Concrete Pavements." Presented at the 92nd Annual Meeting of the Transportation Research Board (TRB), Washington, D.C., 2013.

- Zeinali A., Blankenship P. B., Anderson R. M., Mahboub K. C., "Laboratory Investigation of Asphalt Pavements with Low Density and Recommendations to Prevent Density Deficiency." Presented and published in the proceedings of the8th International Conference on Road and Airfield Pavement Technology (8th ICPT), Taipei, Taiwan, 2013.

- Zeinali A., Mahboub K. C., Southgate H. F., "Effects of Hinged Dowel System on Performance of Concrete Pavement Joints." Presented and published in the proceedings of the 8th International Conference on Road and Airfield Pavement Technology (8th ICPT), Taipei, Taiwan, 2013.